Synthesis of transition metal complexes for catalytic application in green energy storage

Inauguraldissertation

der Philosophisch-naturwissenschaftlichen Fakultät

der Universität Bern

vorgelegt von

Pascal Knörr

von Lüterswil-Gächliwil SO, Schweiz

Leiter der Arbeit:

Prof. Dr. Martin Albrecht

Departement für Chemie, Biochemie und Pharmazie

Universität Bern

Synthesis of transition metal complexes for catalytic application in green energy storage

Inauguraldissertation

der Philosophisch-naturwissenschaftlichen Fakultät

der Universität Bern

vorgelegt von

Pascal Knörr

von Lüterswil-Gächliwil SO, Schweiz

Leiter der Arbeit:

Prof. Dr. Martin Albrecht

Departement für Chemie, Biochemie und Pharmazie

Universität Bern

Von der Philosophisch-naturwissenschaftlichen Fakultät angenommen.

Bern, 06.07.2023

Der Dekan:

Prof. Dr. Marco Herwegh

Acknowledgement

During my PhD I have received help, support and guidance from many people and i would like to express my gratitude to all of you.

Fist of all I want to thank my supervisor Martin, for giving me the opportunity to work in his group and for all the support and guidance given over the years. His great knowledge in chemistry and scientific rigour have always been inspirational. Of course, the rest of the group has played just as big a part (if not bigger) in my PhD journey and I would like to thank all of you. Karst, Marta, Philip, Simone, Kevin, Nathalie, Dide, Gearoid, Alex, Essaïe, Giacomo, Luke, Alicia, James and Laura thank you for all the fun times. Special thanks go to Nicolas for good advice and dumb jokes.

Ich möchte mich auch bei meiner Familie bedanken welche mich während meiner ausgiebigen Studienzeit immer unterstützt hat.

Abstract

This thesis describes the preparation of various PYE- and triazolylidene-based ligands, their coordination to transition metals and the application of those systems in challenging catalysis.

The Introduction outlines the general role of transitionmetal-catalysis in relation to sustainable energy storage and fuel production. Tuning of homogeneous catalysts via specific ligand design is discussed. Concepts of cooperative ligands, such as bifunctionality and redox non-innoncence, as well as electronically flexible ligands are introduced.

A new new ruthenium complex containing a pyridylidene amine-based NNN ligand is explored. It was applied as a catalyst precursor for formic acid dehydrogenation where it showed high activity (*TOF ~10,000 h^{-1}*) even in the absence of basic additives. Mechanistic investigations using correlation of UV-vis and NMR spectroscopic changes with gas evolution profiles indicate rapid and reversible protonation of the central nitrogen of the NNN ligand as key step of catalyst activation, followed by an associative step for formic acid dehydrogenation.

Based on a Ruthenium(II)-arene complex, featuring a tridentate PYE-Amide-Quinoline ligand, a series of derivative complexes, which were systematically modified, were explored in formic acid dehydrogenation. The choice of ancillary arene was shown to be vital for catalyst longevity under catalytic conditions. Furthermore, the essential role of the centrally coordinated amide was demonstrated through substantially lower catalytic activity after protonation or methylation of this position. The introduction of an electron withdrawing CF_3 group on the ligand backbone almost tripled the maximum TOF to 27000 h^{-1} making it the most active ruthenium complex to date in the absence of additives.

An iridium triazolylidene complex was heterogenized and applied in water oxidation. Rational ligand design allowed postmodification of the complex and integration into a self-supporting polymer. Preliminary catalytic runs showed equal activity of unsupported and heterogenized complex. Analysis of the aqueous solution showed leaching of iridium into the reaction media, which was attributed to instability of the polymeric backbone.

A phenoxy-substituted PYE ruthenium complex was investigated. In the solid state and in non-coordination solvents (CD_2Cl_2) the complex is present as a phenolate-bridged dimer but suitable ancillary ligands were shown to coordinate to the ruthenium centers and lead to formation of monomeric complexes. The redox behaviour of the complex was investigated by spectroelectrochemical techniques which showed two reversible redox events with distinct color changes. EPR analysis indicates that the first oxidation event is mainly localized on the ligand.

Collaborations

Chapter III

Dr. Nicolas Lentz	Synthesis of **Alkyl-bisPYE, Ph-bisPYE** and complexes **6** and **7**
Michael Aeschlimann	First synthetic screening of **8**

Chapter IV

Dr. Marcel Garbe	First synthesis of **1-3**

General

Single Crystal X-ray diffraction Service	Measurement and refinement of crystal structures

Table of Contents

CHAPTER I

The role of transition metal catalysis and ligand design in moving towards a cyclic green energy economy

This chapter introduces the role of catalysis in moving towards a sustainable cyclic energy economy. General concepts of green energy storage and the usage of renewable fuels are described. Main focus will lay on water oxidation catalysis, a crucial halfreaction for the production of dihydrogen, as well as on formic acid as a promising liquid organic hydrogen carrier molecule. The important role of rational ligand design in homogeneous catalysis will be discussed and the concept of ligand cooperativity introduced. Cooperativity can entail bifunctional ligands that change their atomic composition during catalysis as well as redox non-innocence. Electronically flexible ligands will also be discussed as a related tool for advanced ligand design. Special attention is given to mesoionic carbenes (MICs) and pyridylidene amines (PYEs) and amides (PYAs) which are introduced as attractive ligand classes for redox catalysis with easy synthetic access, modularity and the ability to change donor properties to suit the metal center.

I.1 The cyclic energy economy

The extensive usage of fossil fuel sources comprised of oil, coal and natural gas has led to a net warming of the planetary atmosphere leading to exacerbated weather and climate events. This is driven by the release of several gases in the combustion process (*e.g.* CO_2) that drive the so-called “greenhouse effect” where the amount of trapped heat, generated by sunlight irradiation of the atmosphere, is increased.[1] In order to stave off global crisis it is deemed necessary to cease usage of fossil fuels and invest in the development of renewable energy sources.[2] This process is well underway and methods to harvest sunlight, wind and water energy are beeing steadily improved. However, to be able to actually fully replace fossil fuels it is essential to efficiently store renewable energy, foremost driven by the transient nature of green energy production which peaks at times not necessarily correlated with peaks of energy demand. Thus, large amounts of energy need to be stored in an easy and safe manner. This has led to the concept of a circular energy economy where materials used for energy storage are constantly recycled, lowering the storage cost and generation of waste.

I.1.1 Green energy storage

Most of the renewably produced energy at the moment is generated in the form of electricity. There are various methods available to store it although no singular one is really adequate for all use cases. Short term storage as it is needed to flatten energy spikes/dips experienced in electrical grids is often done directly via charge separation in capacitors or supercapacitors, but low energy density and quick discharge make the technique ill suited in terms of mid to long term energy storage.[3] A more popular method is storage as kinetic energy, e.g. pumping up water into hydroelectric dams. While the technique works great it requires large amounts of space and is stationary by its very nature. This is contrasted by electrochemical storage e.g., batteries and accumulators which can be built in many sizes and made to fit a huge array of potential applications. Main downside of batteries is slow self discharge even in non-use, degradation over time, weight and slow recharging time. Ultimately, energy can also be stored in chemical bonds.[4] This principle is of course the basis of our existence, as in nature plants (and some bacteria) use solar energy to split water and form energy-rich biological reducing agents that allow production of sugars and other necessary cell components.[5,6] Convergently we can artificially store energy by forming various energy-rich organic moleculas that can then be used as renewable fuels.[7]

I.1.2 Hydrogen

While the photosynthetic pathways in plants are well understood, the complexity of the related systems make direct translation into artificial systems difficult.[7–10] To achieve artificial photosynthesis two half reactions have to be performed which are water oxidation[10–13] (providing electrons and protons) and reduction of a feedstock molecule to generate fuels.[14] Dihydrogen has been proposed as one of the most promising alternative fuels. It can be generated from only water as a feedstock and upon usage only benign water waste is again released. The formation of dihydrogen by electrolysis of water has been known for a long time and was already discoverd in the 1800s.[15] However direct formation and usage of dihydrogen has major drawbacks. H_2 is explosive and and has a low volumetric energy density rendering it inferior to traditional fuels in most applications. It has thus been proposed to instead use liquid organic hydrogen carriers (LOHCs) as transient storage vectors. LOHCs constitute small organic molecules than can undergo reversible hydrogenation and dehydrogenation cycles, allowing safe use of thus stored dihydogen. [16] Various systems have been investigated for their suitablility including quinolines[17], boranes[18], formic acid (Fig. 1) and methanol.[19]

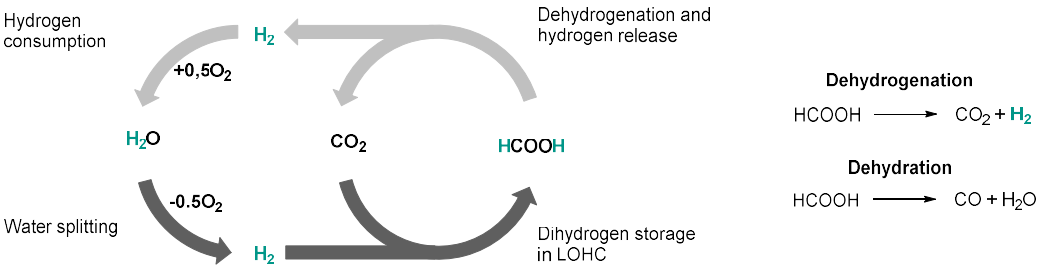

Figure 1. Proposed hydrogen production cycle with intermediate storage as formic acid.

I.1.3 Formic acid

Formic acid (FA; HCOOH) is an outstanding candidate for hydrogen storage (Figure 1) as it can be easily handled and provides sufficiently high energy densities for broadscale application.[20–22] Specifically FA has a volumetric energy density of 1.77 kWh/l, which is significantly higher than what is obtainable from gaseous H_2 even when high pressure (700 bar) gas tanks are used which reach 1.4 kWh/l.[23] FA can be decomposed via two competing pathways which are dehydrogenation (to H_2 and CO_2) and the undesirable dehydration (to H_2O and CO) which necessitates development of suitable selective catalysts. While catalytic formic acid dehydrogenation (FADH) is known since the 1960s the field has only picked up much interest since the seminal work of Beller and Laurency in 2008 (Scheme 1) where they proposed FA as an LOHC.[24–26]

$[Ru(H_2O)_6](tos)_2$ + TPPTS	$[RuCl_2(PPh_3)_3]$
H_2O	DMF
120°C	40°C
HCOOH/HCOONa	HCOOH/NEt_3
TOF: 460h^{-1}	TOF: 2688 h^{-1}
Laurenczy 2008	*Beller 2008*

Scheme 1: Seminal FADH systems of the groups of Laurenczy and Beller

I.2 Ligand design for efficient and selective homogeneous catalysis

Catalysis is a cornerstone of chemistry, allowing the lowering of activation barriers to increase reaction rates. It allows synthesis of desirable components under less harsh conditions, lowering energy consumption and lessens stochiometric production of waste. Thus, catalysts will also play a central role in the production and usage of renewable fuels. For example, while water splitting can be performed very easily by submerging two gold electrodes in water the reaction is not energy efficient enough to allow broadscale production of dihydrogen. Suitable catalysts are thus needed on the electrode surfaces to increase the efficiency of the overall reaction. Furthermore, suitable catalysts need to be developed for the production and subsequent dehydrogenation of LOHCs.

Transition metals play a vital role in many, if not most, catalytic reactions. Their properties and reactivity are dependent both on the metal center as well as on potentially coordinated ligands and must thus suitably be tuned toward the desired reaction outcome. Different metals often have an intrinsic proclivity towards certain reactivities but by developing appropriate ligands this reactivity can be massively enhanced or even subverted. Tuning of catalytic properties through ligands, in well defined molecular complexes, is one of the big benefits homogenous catalysts provide over heterogenous systems, where activity and selectivity are difficult to control. Classical ligands such as phosphines amines and halides feature static donor properties towards the metal, complemented by their individual steric characteristics. In catalysts featuring such ligands reactivity is exclusively metal centered. However, ligands can also play a more prominent role during a catalytic reaction.[27–29] Cooperative ligands for example can actively participate during catalysis by undergoing reversible structural changes where substrate-bonds can be split over a metal-ligand bond. Redox non-innocent ligands can go through electronic changes, thus donating or storing electrons in place of the metal center, allowing reactivity that a classical metal complex could never achieve. Functional ligands can even be the exclusive active site of a complex, turning the metal into a stabilizing spectator.[30] Another way to improve catalytic activity can be the introduction of electronically flexible ligands, that can adapt their donor properties to suit the needs of the metal center through mesomeric charge distribution effects.

I.2.1 Bifunctional substrate activation

In most classical catalytic scenarios bond activations take place exclusively on the metal center while the ligand plays a spectator role. This accounts for reactions such as oxidative additions, reductive eliminations or β-hydride eliminations. However, bonds can also be heterolytically split over a metal–ligand bond which retains the oxidation state of the metal center (Scheme 2). Such reactivity is actually often used in enzymes like hydrogenases. The direct involvement of the ligand skeleton during catalysis can eliminate the need for additives and lower production of waste. Various exemplary systems that operate in such a manner are described in this section with a special focus on hydrogenation[31] and dehydrogenation reactions as it critically relates to the formation and decomposition of LOHCs.

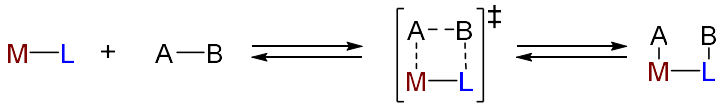

Scheme 2. Metal ligand cooperation assisted bond activation.

An early example of metal ligand cooperativity was discovered and investigated by Shvo in the mid 80s.[32–34] The Shvo pre-catalyst consists of a dinuclar ruthenium complex with a hydroxycyclopentadienyl ligand that has been applied for various hydrogen transfer reactions involving carbonyls, iminies, amines and alcohols as substrates.[35] In solution the dimeric species **1** dissociates into the monomeric catalytically active complexes **2** and and **3** (Scheme 3). Transfer hydrogenation reactions are proposed to take place through an outer sphere mechanism where the hydride from the ruthenium center and the proton from the OH of the hydroxycyclopentadienyl ligand are transferred concertedly onto the substrates.[36–38]

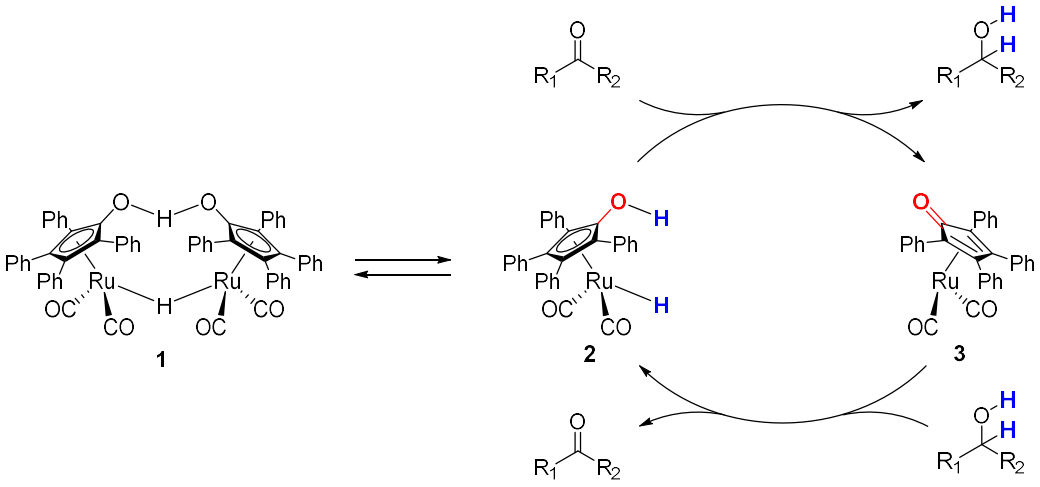

Scheme 3. Shvos dimeric precatalyst **1** can dissociate in solution into catalytically active species **2** and **3**. The proposed reaction mechanism in transfer hydrogenation reactions involves no substrate coordination but takes exclusively place in the outer sphere.

Other early examples of bifunctional metal ligand cooperation[39,40] were discovered by R. Noyori who applied it to hydrogenation reactions.[41] The bifunctionality was initially introduced via simple diamine ligands that could reversibly store a proton on the ligand during hydrogenation catalysis ("NH effect"). In tandem with the ruthenium center formal dihydrogen was transiently stored on the complex, with the hydridic hydrogen coordinated to ruthenium. In an outer sphere mechanism hydride and proton can then be concertedly transferred to a substrate. The general design principle has been greatly expanded over the years with different ancillary ligands and a vast library of possible ligand modifications on the amine.[42–44] For example ruthenium arene complexes were developed with outstanding performance in hydrogenation reactions (Scheme 4).[45–48] In these systems various arenes and bidentate ligands were explored, main important feature was the presence of at least one primary or secondary amine coordination site to enable the transient proton storage on the ligand. The ruthenium chloride catalyst precursor **4** was activated in the presence of base to active complex **5** which then catalyzes transfer hydrogenation of alhohols via intermediate **6**. Hydrogen transfer is supposed to take place in a concerted fashion as shown in **TS1**.

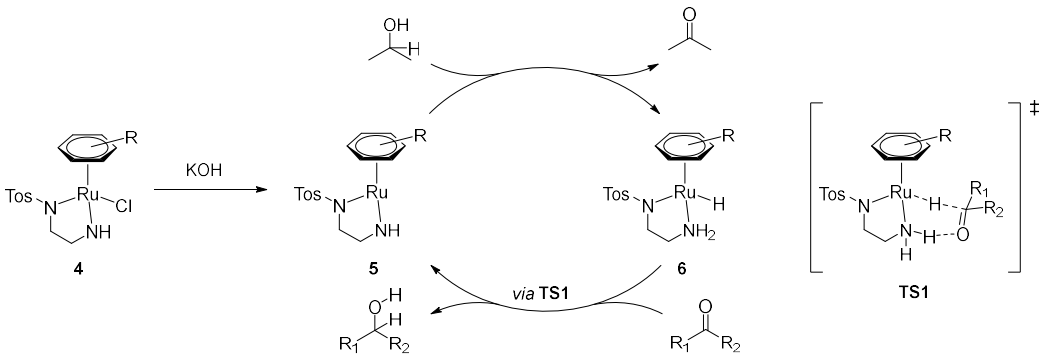

Scheme 4. Noyori type bifunctional ruthenium arene based catalysts and proposed mechanism for the enantioselective transferhydrogenation of ketones.

Another milestone of cooperative catalysis are the pincer-type ligand systems initially developed by Milstein.[49–54] The ligands are based on 2,6-lutidine with a central pyridine mojety and two side arms with chelating groups. Over the years this type of system has been expanded from the initial ruthenium complex and derivates of the ligand have been coordinated to various transition metals (e.g. Ru, Ir, Fe, Mn, Co, Re, Mg).[55] These lutidine-based ligands can act cooperatively by reversible deprotonation of a CH_2 linker *ortho* to the central pyridine ring, which leads to dearomatization of the heterocycle and exocyclic double bond formation (Scheme 5).[56–62] This renders the complex active and H-X bonds (X = H, O, N, B) can be heterolytically split over the metal center and ligand. Notably the coordination mode of the central nitrogen switches from L-type amine to X-type amide during this mechanism and the oxidation state of the metal does not change in the catalytic cycle. Based on the aromatization/dearomatization principle a ruthenium catalyst was developed that was active in the splitting of water via two steps, one thermally driven, the other photocatalytic.[63–65] In a first thermally induced step complex **7** eliminates dihydrogen to give complex **8**. Light irradiation (320 - 420 nm) then promotes O_2 elimination, likely through H_2O_2 as an intermediate, forming unsaturated complex **9**. Through proton migration from a CH_2 linker to the ruthenium center complex **10** is formed, which can react with water to regenerate **7**. Related complexes are also active in various other transformations e.g. alcohl dehydrogenation, ester hydrogenation[66], alcohol and amine couplings as well as the hydrogenation[67] of carbamates carbonates and formates.[57,68] The groups of Nozaki and Pidko showed high activity of iridium[69,70] and ruthenium[71] systems in formic acid dehydrogenation, although in the presence of exogenous base.

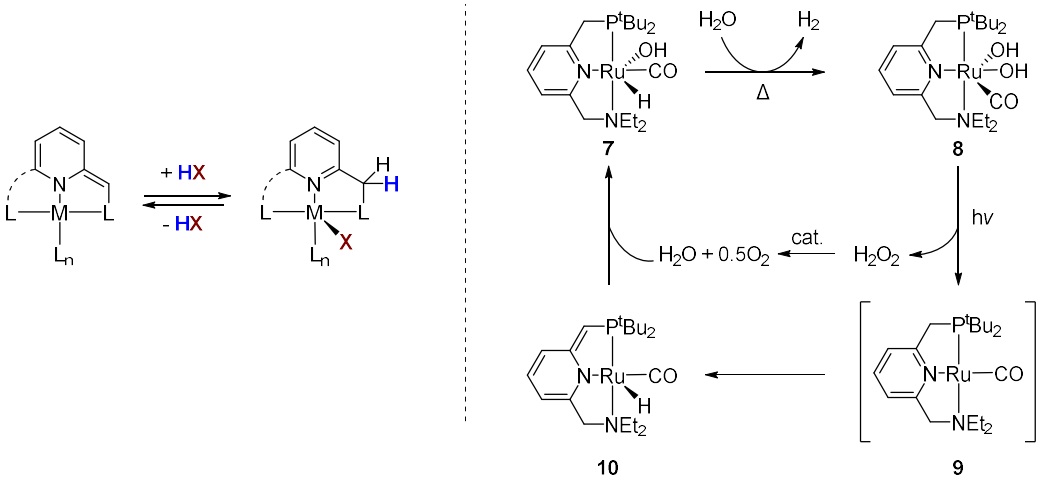

Scheme 5. *Left*: General mechanism of heterolytic bond splitting with lutidine based systems. *Right*: Water oxidation mechanism with the Milstein-type system

Based on the ligand aromatization methodology Milstein et. al. also developed acridine pincer type systems where cooperativity can take place on the remote C9 position of the ligand (Scheme 6.)[72,73] Complex **11** reacts with H_2 in the presence of KOH to form reduced and dearomatized complex **12**. A ruthenium system[74] featuring such a ligand was recently applied in the dehydrogenation of neat formic acid, although preliminary analysis indicates that cooperativity might not be essential for this reaction.[75]

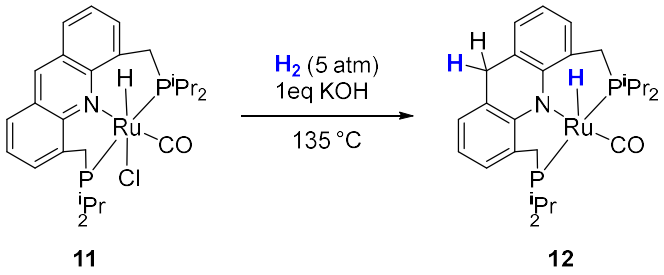

Scheme 6. Acridine-type Milstein system and heterolytic dihydrogen splitting over ruthenium and ligand skeleton.

Following the reactivity demonstrated by Milstein the group of Huang developed ligands based on aminopyridine where the CH_2 linker of the lutidine systems is replaced with an NH motif.[76] The ligand systems have been coordinated to various transition metals[77] (e.g. Ru, Ir, Cr, Fe, Mo, Pd, Ni, Cu) and were applied in base free transfer hydrogenation,[76,78] hydrogenation of

esters[79] and amine coupling reactions,[80] among others[81]. In 2016 they demonstrated the application of a series of ruthenium complexes in formic acid dehydrogenation (Scheme 7).[82] Dearomatized complex **13** can react with FA to form formate complex **14**, which then eliminates CO_2 to the dihydride complex **15**. Dihydrogen liberation finally regenerates complex **13**. During the catalytic cycle the ruthenium center maintains its oxidation state of 2^+. The catalyst was active in the absence of additives with TOFs of 2,380 h^{-1} and TONs of 93,000 but performance was drastically improved in the presence of triethylamine which boosted TONs to 250,000. Best performance was achieved at 90°C with TOFs of 7,000 h^{-1} and a TON of 1,100,000.

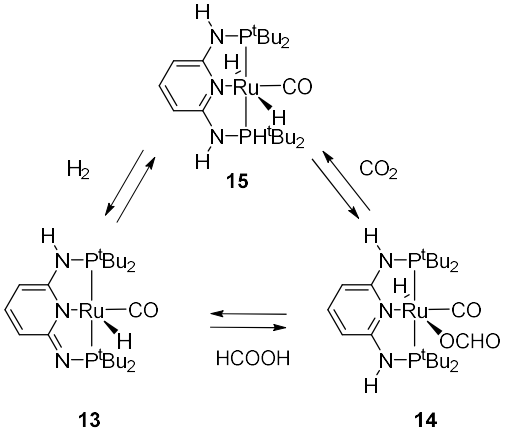

Scheme 7. Proposed reaction mechanism for formic acid dehydrogenation with aminopyridine based systems.

Aliphatic tridentate pincer ligands are another versatile platform extensively studied for metal ligand cooperation. Initially investigated by Fryzuk[83–86] et al. in the 80s a huge library of derivative systems has been developed with different transition metals and various ligand modifications. During catalysis the centrally coordinated amide can reversibly store a proton, thereby allowing heterolytic bond cleavage over the nitrogen metal bond. The Schneider group has also shown that the aliphatic ethyl backbone of this ligand class can potentially be reversibly dehydrogenated as well, leading to two bifunctional MLC modes.[87,88] Hydrogenation of various substrates such as ketones, esters, azides,[89] alcohols[90] and amino borane adducts[91,92] is known. Furthermore, Beller et. al. demonstrated in 2013 the application of these systems in methanol dehydrogenation (Scheme 8).[93,94] The precatalyst **16** is activated by base, forming complex **17** which reacts with alcoholates to complex **18**. Via **19**, hydride complex **20** is generated. This species reacts with methanol either by direct deprotonation of the OH via the ruthenium hydride, forming dihydrogen complex **23,** or by first deprotonating an equivalent of

methanol via the amide ligand (**21**) and then reacting with a second equivalent of methanol to form dihydrogen complex **22**. Dihydrogen release then regenerates the active species **17**.

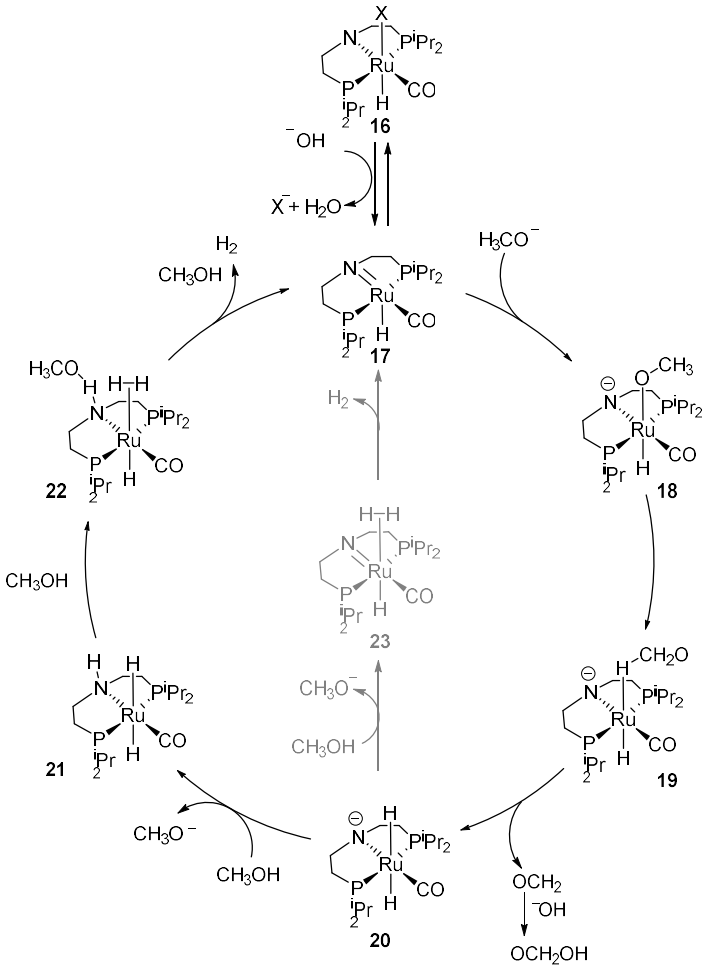

Scheme 8. Proposed catalytic cycle for aquaeous methanol reforming by Beller *et. al.*

The group of Himeda has explored bifunctional ligands bearing 2-hydroxypyridine-based skeletons.[95,96] Corresponding irdium complexes were applied in CO_2 reduction to formic acid where high catalytic activity is proposed to arise from the presence of the ortho pyridone groups that can act as internal bases to promote heterolytic dihydrogen activation (Scheme 9).[97–99] The precatalyst **24** is activated by loss of H_2O, which frees up a coordination site in **25** for dihydrogen coordination to form **26**. Dihydrogen is then heterolytically split over the iridium center and the pyridonate ligand (**27**). The proton on the ligand is highly labile (**28**), thus reaction with CO_2 results in intermediate complex **29**. Conversion to formate complex **30** and subsequent loss of the formate regenerates **25**. Best performance was achieved with a derivative complex

featuring two iridium centers coordinated to a tetrahydroxybispyrimidine ligand and TOFs of 15,000 h^{-1} and TONs of 153,000 were reported. Yamaguchi has used the same ligands for acceptorless alcohol dehydrogenation and proposed that the pyridine moiety again acts as an internal base to promote OH bond activation.[100] However, When applied in formic acid dehydrogenation cooperativity appears to play no significant role compared to electronic ligand influences.[101,102]

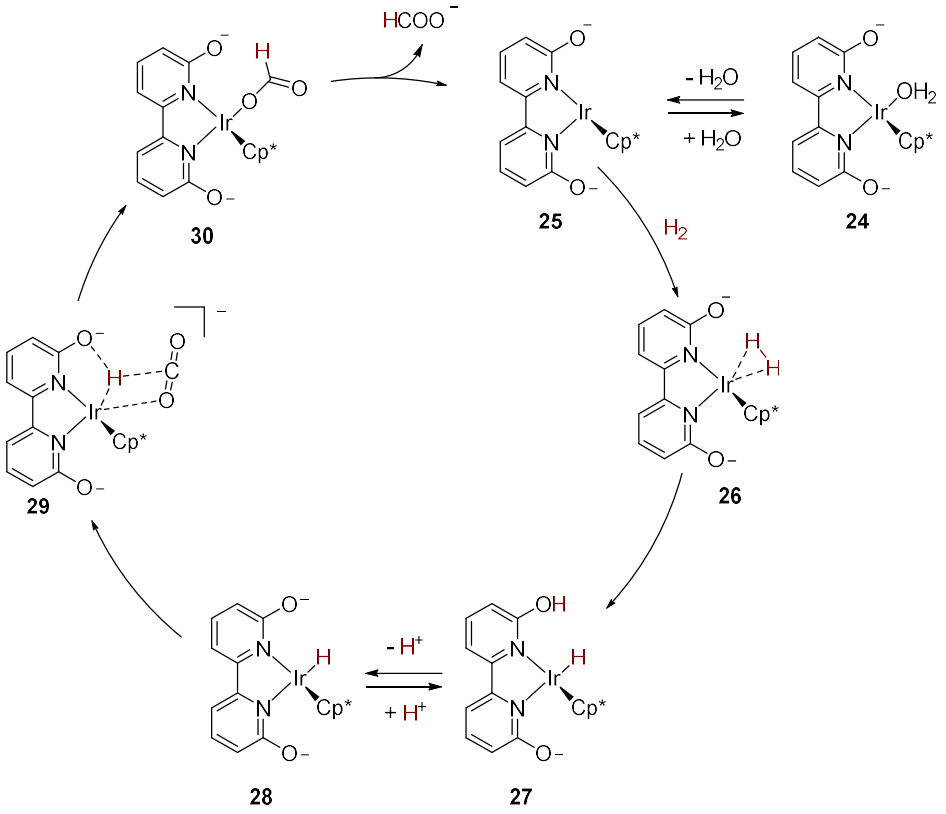

Scheme 9. Proposed CO_2 hydrogenation mechanism with 2-hydroxypyridine based ligands.

I.2.2 Redox active ligands

With classical transition metal complexes redox events take exclusively place at the metal center as ligand-cantered events are energetically disfavoured. In such systems the ligands are deemed to be redox inactive. However, a broad field of redox active ligands has been investigated. These ligands allow ligand-centred redox events to take place.[103,104] Depending on ligand and metal centers these events can be well defined and highly localized or be distributed between ligand an metal, making assignment of traditional oxidation states hazardous. Redox active ligands can benefit catalytic systems in various ways. By acting as

electron reservoirs otherwise inaccessible redox chemistry can occour even with redox inactive metals such as Zn(II) or Zr(IV). They can also impart nobility on early transition metals that would normally favour one-electron processes but in conjunction with a redox active ligand can now catalyze two electron transformations like oxidative additions. Redox-active ligands can further directly transfer single electrons from ligand to a substrate or bifunctionally activate a substrate. A majority of these systems are based on o-phenylene type structrues such as catecholes, *o*-aminophenolates or *o*-diaminophenolates (Scheme 10).[105,106]

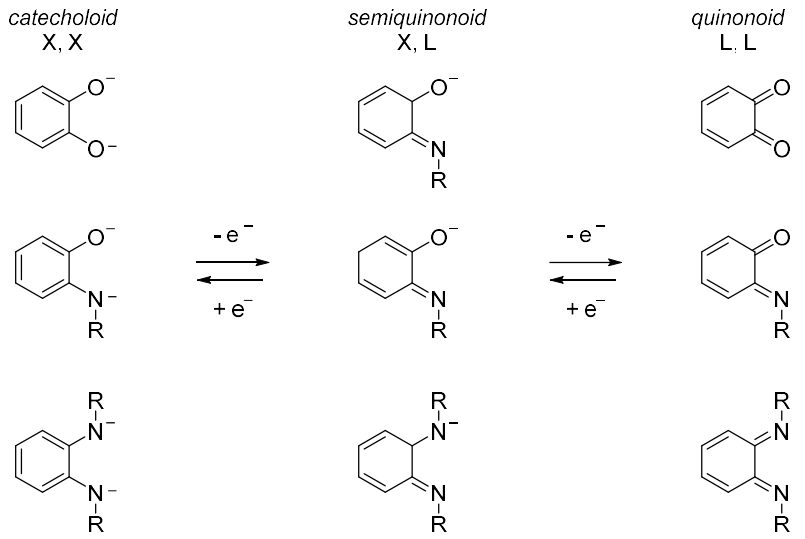

Scheme 10. o-phenylene ligands in different oxidation states (redox- isomers).

Heyduk et. al. have investigated the redox chemistry of aminophenolate type ligands in conjunction with Zr(IV), a d^0 metal center that has no access to oxidative transformations. The two redox active ligands in complex **31** (Scheme 11) can provide two electrons to allow reductive elimination of the two phenyl ligands from **32**. Solvento complex **33** is thus formed which can oxidatively add Cl_2 to the zirconium metal center (**34**).[107] In these processes the metal does not change oxidation state but both ligands undergo $1e^-$ oxidation, allowing oxidative additions and reductive eliminations from an otherwise redox inactive metal.

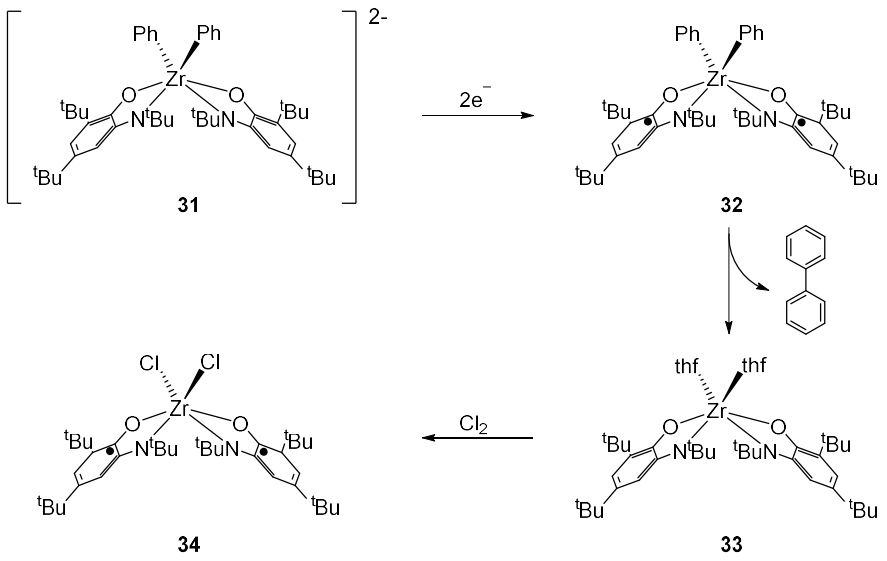

Scheme 11. Reductive elimination and oxidative addition from a Zr(IV) complex facilitated by two aminophenolate Ligands.

Soper *et al*. have applied the homoleptic Co(III) complex **10** with aminophenolate ligands in a Negishi-type cross coupling reaction (Scheme 12).[108,109] The redox active ligands allow oxidative addition of an alkyl fragment onto the metal center, which does not alter its oxidation state. Instead, both ligands undergo one-electron oxidation to form stable iminosemiquinone radicals in complex **36**. The R group can then be transferred to aryl zinc bromides.

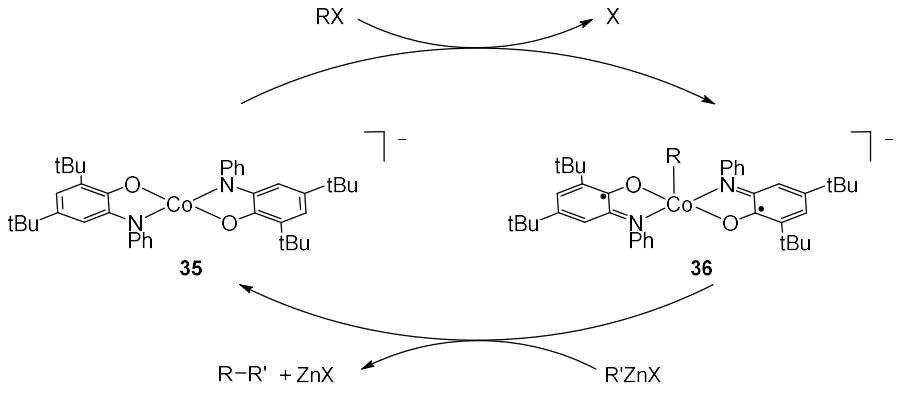

Scheme 12. Reductive elimination and oxidative addition from a Zr(IV) complex facilitated by two aminophenolate Ligands

The group of Tanak has investigated dinuclear ruthenium catalyst **37** for electrocatalytic water oxidation (Scheme 13).[110] The ruthenium centers are connected via an anthracene linker that features two terpyridine moieties that coordinate to the metal. Both metals further complexate redox active quinone ligands. The ground state bis(hydroxy) complex **37** undergoes double deprotonation to form intermediate **38** with peroxobridged ruthenium centers. This reactivity is facilitated by the quinone ligands undergoing one-electron reduction to the respective semiquninones before releasing the stored electrons and returning to the quinone form while the peroxo bridge remains in **39**. O-O bond formation was initially proposed to involve formation of Ru(III) in complex **40**, to allow reaction with H_2O while releasing O_2 and generating aqua complex **41**. However, follow up investigations indicate that this step can well take place without formal oxidation change of ruthenium and instead may be solely dependent on ligand-centered redox events.[111–114] In a final step the aqua ligands loose a proton each to form **37** again.

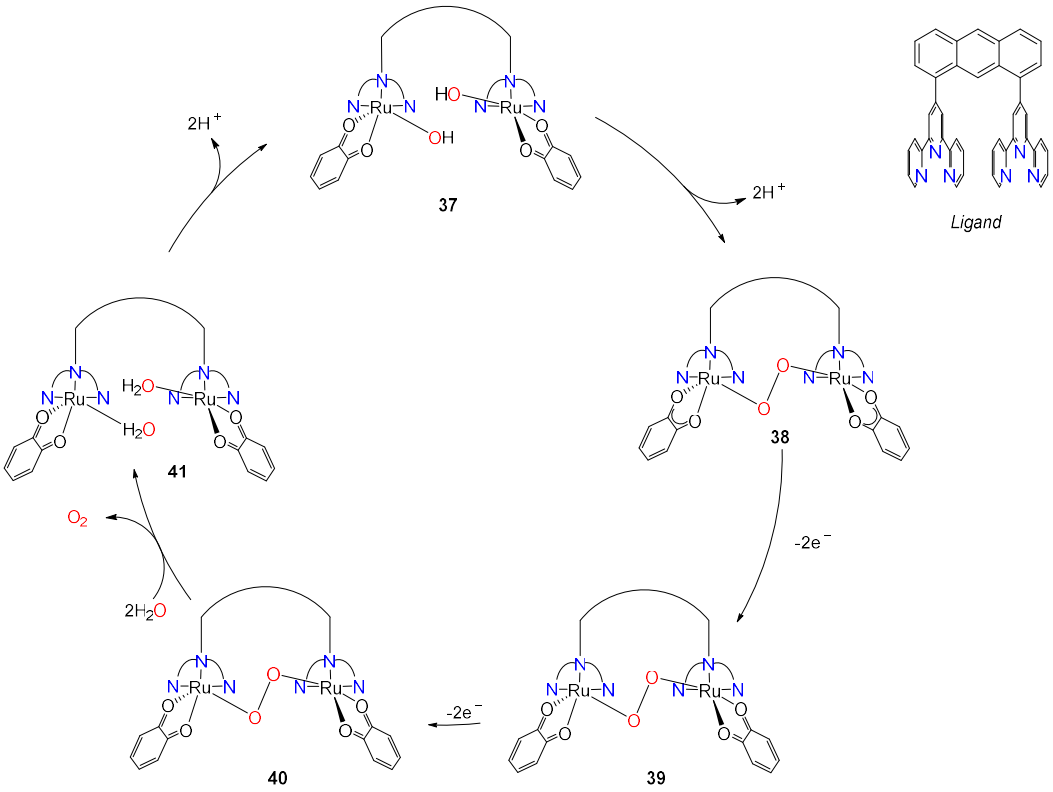

Scheme 13. Proposed mechanism for electrocatalytic water oxidation with dimeric Ru(II) catalyst supported by *o*-quinone ligands. Putative mechanism shown here involves Ru(III), but it is possible that all redox events are ligand centered and the metal oxidation state does not change during the reaction.

I.2.3 Electronically flexible Ligands

In the previous sections, basic principles and mechanisms of cooperative ligand-assisted transition metal catalysis have been discussed. In these systems the ligands reversibly undergo distinct structural or electrochemical transformations to facilitate the catalysis. Electronically flexible ligands follow a different design principle where they can adapt their donor properties and electronic structure without undergoing chemical transformations. This potentially allows such ligands to better suit the needs of a metal center during catalytic transformations where multiple oxidation states must be accessed or transient species with less suitable coordination behaviour need to be activated.

N-heterocyclic carbenes

The most investigated ligand class in this context are N-heterocyclic carbenes (NHCs) with an incredibly diverse spectrum of ligands and corresponding transition metal complexes. The first stable NHC was an imidazolylidene isolated by Arduengo in 1991[115] which led to an explosion of studies aiming to synthesize and analyse related compounds.[116,117] Imidazolylidene ligands can be represented by two different canonical resonance structures[118] *i.e.* a neutral and a zwitterionic one (Scheme 14), which enables the electronic flexibility of these compounds. The ligand class is most prominentely featuered in the 2nd generation Grubbs catalyst that revolutionized the field of olefin methathesis, but there is little indication that electronic flexibility plays a role in the high activity of this complex.[119]

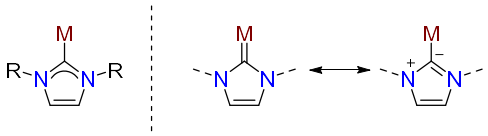

Scheme 14. Limiting resonance structures of classical carbenes (2-imidazolidenes)

Properties of NHC transition metal complexes can be modulated by choosing different N-heterocycles but are also greatly impacted by the position of the carbene site. Aside from the “classic” NHCs such as 2-imidazolylidenes various mesoionic carbenes (MICs) have been explored.[120] In these ligands the carbene is not flanked on both sites by heteroatoms, thereby decreasing their stabilizing effects. However, the decreased proximity of heteroatoms generally increases the σ-donation strength of the carbene ligand which can be highly beneficial, especially for oxidation catalysis where metals must reach high oxidations states during the catalytic cycles. MICs can also not be represented by neutral canonical resonace structures but always feature positive and negative charges.

1,2,3-triazolylidenes (Scheme 15) are an attractive class of MIC ligands that stand out through easy synthetic routes that allow the introduction of a highly diverse range of substituents in 1,3

and 4 positions. The broad functional group tolerance of the copper-catalyzed alkyne azide cycloaddition reaction,[121–125] used to form the heterocycle, allows to easily finetune catalytic systems and grants access to simple methods for anchoring complexes to solid supports, which is important in the context of electrochemically driven water oxidation. Triazolylidene ligands have been extensively exploited in coordination chemistry with 2nd and 3rd row transition metals e.g. Ru, Ir, for which they are very well suited, but also many examples of 1st row complexes are known.[126,127] Triazolylidene Ir[128–133] and Ru[134] complexes have shown high activity in water oxidation either with sacrificial oxidants or electrochemically driven. This is facilitated by the high stability of the carbene metal bond in these complexes and the strong σ-donation which allows accessing of relevant high oxidation states in the catalytic cycles. Furthermore Ir systems have shown high activity in acceptorless dehydrogenation reactions with alcohols and amines as substrates.[17,135,136]

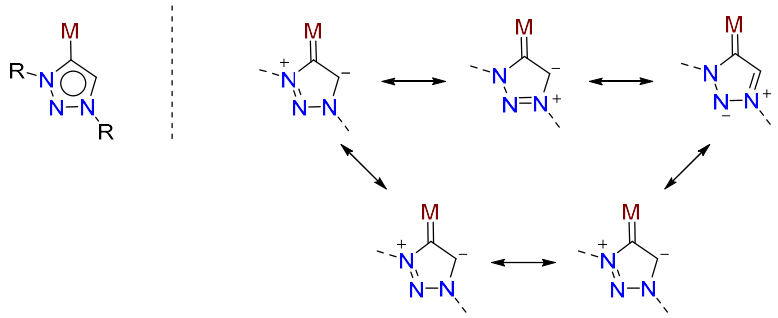

Scheme 15. Donor flexibility of triazolylidene ligands.

Electronically flexible N-donor ligands

The concept of electronic flexible ligands has also been expanded towards nitrogen donor sites.[137] Ligands based on guanidine,[138–140] 2-imidazole-2-imine[141] and bis[(dialkylamino)cyclopropenimine][142] have been investigated by the groups of Alcarazo and others.[143] These types of ligands can be represented by two resonance structures with the coordinating nitrogen adopting a neutral L-type coordination or an zwitterionic configuration where the nitrogen becomes anionic and coordinates in an X-type fashion (Scheme 16). Guanidine-based complexes have been applied in various transformations such as lactide polymerisation, hydrofunctionalisation and oxidation reactions.[144]

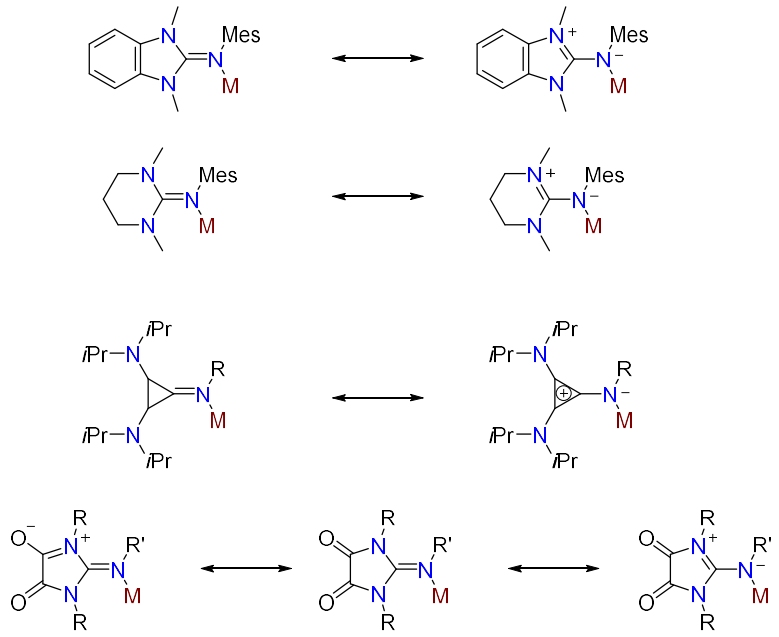

Scheme 16. Resonance forms of various N-donor flexible ligands

In 2009 another family of electronically flexible ligands was investigated in the seminal works of Douthwaite[145] and Johnson.[146] Analogous to the previously discussed systems, these *ortho* and *para* pyridylidene amines (PYEs) feature two limiting resonance structures (Scheme 17). Thus they can be represented as L-type π-acidic weak σ-donors or adopt a π-basic zwitterionic form that coordinates as an X-type ligand with stronger σ-donation based on their mesomeric structures.[147] Synthetic access to PYEs is generally straightforward and inexpensive, making these ligands promising for cost-sensitive applications. A chelating phenoxy-PYE ligand coordinated to iridium which was recently investigated by Lentz *et. al.*, has shown state-of-the-art performance in formic acid dehydrogenation catalysis.[148] The simple cost-efficient synthesis of ligand and complex was shown to significantly reduce the overall cost of dihydrogen production in such systems, even when compared to 1st row transition metal-based systems that use Earth-abundant metals like iron.

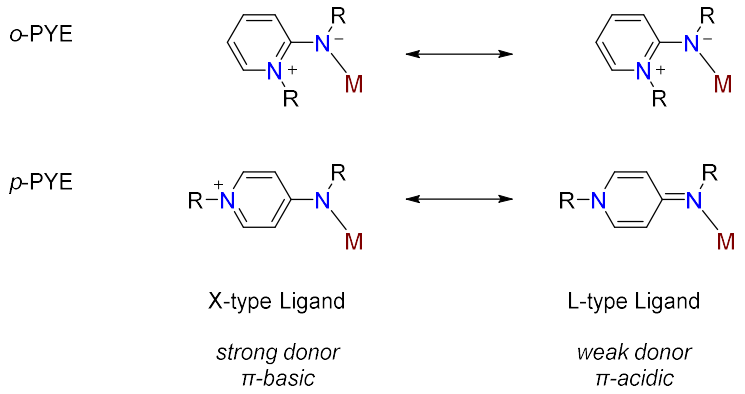

Scheme 17. Limiting resonance structures of *ortho* and *para-PYEs*

Wright et. al. expanded upon the PYE system by replacing the amine group with an amide functionality, thus forming pyridylidene amides (PYAs).[149,150] The amide can adopt an additional mesomeric structure due to the possibility to form an negatively charged enolate (Scheme 18). PYAs have been shown to adapt their donor properties to different solvent polarities with predominatly neutral character in apolar solvents (CD_2Cl_2) and higher contributions of the zwitterionic structure in polar solvents (MeOH, DMSO).[151] Furthermore it was demonstrated that PYAs can significantly adopt their donor properties in response to the coordination of different ancillary ligands.[152] PYAs are thus highly attractive ligands also due to their easy synthesis from diverse, commercially available aminopyridines. Therefore, the library of PYAs has been greatly enlarged, demonstrating easy access to a variety of ortho, para, and also meta PYA complexes.[153–156] Ruthenium complexes with pincer ligands were applied in the transfer hydrogenation of ketones and were shown to be one of the most active systems for this type of transformation.[154] A bidentate bis(PYA) complex was shown to be ultra efficient in olefin oxidation catalysis demonstrating resilience towards oxidative conditions.[157] PYA-iridium complexes have furthermore shown high performance in water oxidation catalysis.[158]

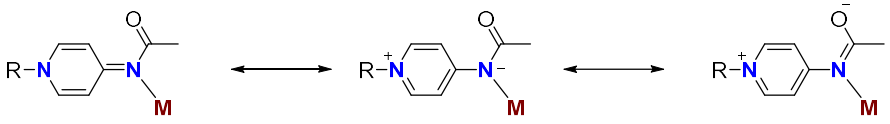

Scheme 18. Limiting resonace structures of *p*-PYA ligands

I.3 Aim and Scope of the Thesis

Rational ligand design of homogenous transition metal complexes plays a crucial part in developing highly active and durable systems. Thus, bifunctional and electronically flexible ligands provide fascinating opportunities to design new catalysts. This thesis aims to investigate new ligand systems in the context of chemical energy storage, with the goal to improve performance of key reactions such as water oxidation or the dehydrogenation of LOHCs, especially formic acid.

Chapter II presents the synthesis of a first generation of pyridylidene amine-based Ru-NNN complexes for additive-free formic acid dehydrogenation catalysis. Conditions to achieve high catalyst turnover frequencies are investigated, as well key steps in the catalytic mechanism.

Chaper III describes a second generation of PYE-based Ru-NNN complexes where modifications on the main ligand and the ancillary arene mojety were introduced and their catalytic impact assessed. With the most performant derivative complex the catalytic activity of the system could be increased threefold.

Chapter IV focuses on the heterogenisation of a triazolylidene Ir complex for water oxidation catalysis. Through distinct ligand design the complex was postmodified to allow its integreation into a self-supported polymer with simple techniques.

Chapter V discloses the synthesis of a phenoxy PYE based ruthenium complex. Coordination chemistry of the complex is discussed, and its redox behaviour was investigated by spectroelectrochemical techniques.

I.4 References

1 S. A. Montzka, E. J. Dlugokencky and J. H. Butler, *Nature*, 2011, **476**, 43–50.

2 N. Armaroli and V. Balzani, *Angew. Chem. Int. Ed.*, 2007, **46**, 52–66.

3 Z. Yang, J. Zhang, M. C. W. Kintner-Meyer, X. Lu, D. Choi, J. P. Lemmon and J. Liu, *Chem. Rev.*, 2011, **111**, 3577–3613.

4 N. S. Lewis and D. G. Nocera, *Proc. Natl. Acad. Sci. U.S.A.*, 2006, **103**, 15729–15735.

5 J. H. Alstrum-Acevedo, M. K. Brennaman and T. J. Meyer, *Inorg. Chem.*, 2005, **44**, 6802–6827.

6 D. Gust, T. A. Moore and A. L. Moore, *Acc. Chem. Res.*, 2001, **34**, 40–48.

7 D. Gust, T. A. Moore and A. L. Moore, *Acc. Chem. Res.*, 2009, **42**, 1890–1898.

8 S. Berardi, S. Drouet, L. Francàs, C. Gimbert-Suriñach, M. Guttentag, C. Richmond, T. Stoll and A. Llobet, *Chem. Soc. Rev.*, 2014, **43**, 7501–7519.

9 J. J. Concepcion, R. L. House, J. M. Papanikolas and T. J. Meyer, *Proc. Natl. Acad. Sci. U.S.A.*, 2012, **109**, 15560–15564.

10 M. D. Kärkäs, E. V. Johnston, O. Verho and B. Åkermark, *Acc. Chem. Res.*, 2014, **47**, 100–111.

11 W. Rüttinger and G. C. Dismukes, *Chem. Rev.*, 1997, **97**, 1–24.

12 J. K. Hurst, *Science*, 2010, **328**, 315–316.

13 K. J. Young, L. A. Martini, R. L. Milot, R. C. Snoeberger, V. S. Batista, C. A. Schmuttenmaer, R. H. Crabtree and G. W. Brudvig, *Coordination Chemistry Reviews*, 2012, **256**, 2503–2520.

14 C. Herrero, A. Quaranta, W. Leibl, A. W. Rutherford and A. Aukauloo, *Energy Environ. Sci.*, 2011, **4**, 2353.

15 R. de Levie, *Journal of Electroanalytical Chemistry*, 1999, **476**, 92–93.

16 N. D. McDaniel and S. Bernhard, *Dalton Trans.*, 2010, **39**, 10021.

17 Á. Vivancos, M. Beller and M. Albrecht, *ACS Catal.*, 2018, **8**, 17–21.

18 N. Blaquiere, S. Diallo-Garcia, S. I. Gorelsky, D. A. Black and K. Fagnou, *J. Am. Chem. Soc.*, 2008, **130**, 14034–14035.

19 K. Sordakis, C. Tang, L. K. Vogt, H. Junge, P. J. Dyson, M. Beller and G. Laurenczy, *Chem. Rev.*, 2018, **118**, 372–433.

20 D. Mellmann, P. Sponholz, H. Junge and M. Beller, *Chem. Soc. Rev.*, 2016, **45**, 3954–3988.

21 N. Onishi, G. Laurenczy, M. Beller and Y. Himeda, *Coord. Chem. Rev.*, 2018, **373**, 317–332.

22 F. Joó, *ChemSusChem*, 2008, **1**, 805–808.

23 J. Eppinger and K.-W. Huang, *ACS Energy Lett.*, 2017, **2**, 188–195.

24 R. S. Coffey, *Chem. Commun. (London)*, 1967, 923b.

25 B. Loges, A. Boddien, H. Junge and M. Beller, *Angew. Chem. Int. Ed.*, 2008, **47**, 3962–3965.

26 C. Fellay, P. Dyson and G. Laurenczy, *Angew. Chem. Int. Ed.*, 2008, **47**, 3966–3968.

27 J. R. Khusnutdinova and D. Milstein, *Angew. Chem. Int. Ed.*, 2015, **54**, 12236–12273.

28 J. I. van der Vlugt, *Eur. J. Inorg. Chem.*, 2012, **2012**, 363–375.

29 H. Grützmacher, *Angew. Chem.*, 2008, **120**, 1838–1842.

30 Q. J. Bruch, A. Tanushi, P. Müller and A. T. Radosevich, *J. Am. Chem. Soc.*, 2022, **144**, 21443–21447.

31 C. Gunanathan and D. Milstein, *Science*, 2013, **341**, 1229712.

32 Youval. Shvo, Dorotha. Czarkie, Yocheved. Rahamim and D. F. Chodosh, *J. Am. Chem. Soc.*, 1986, **108**, 7400–7402.

33 Y. Blum and Y. Shvo, *Isr. J. Chem.*, 1984, **24**, 144–148.

34 Y. Blum, D. Czarkie, Y. Rahamim and Y. Shvo, *Organometallics*, 1985, **4**, 1459–1461.

35 R. Karvembu, R. Prabhakaran and K. Natarajan, *Coordination Chemistry Reviews*, 2005, **249**, 911–918.

36 C. P. Casey and J. B. Johnson, *Can. J. Chem.*, 2005, **83**, 1339–1346.

37 C. P. Casey, S. W. Singer, D. R. Powell, R. K. Hayashi and M. Kavana, *J. Am. Chem. Soc.*, 2001, **123**, 1090–1100.

38 J. B. Johnson and J.-E. Bäckvall, *J. Org. Chem.*, 2003, **68**, 7681–7684.

39 R. Noyori, M. Yamakawa and S. Hashiguchi, *J. Org. Chem.*, 2001, **66**, 7931–7944.

40 R. Noyori, M. Kitamura and T. Ohkuma, *Proc. Natl. Acad. Sci. U.S.A.*, 2004, **101**, 5356–5362.

41 R. Noyori and S. Hashiguchi, *Acc. Chem. Res.*, 1997, **30**, 97–102.

42 J. Canivet and G. Süss-Fink, *Green Chem.*, 2007, **9**, 391–397.

43 T. Ohkuma, H. Ooka, S. Hashiguchi, T. Ikariya and R. Noyori, *J. Am. Chem. Soc.*, 1995, **117**, 2675–2676.

44 J. Takehara, S. Hashiguchi, A. Fujii, S. Inoue, T. Ikariya and R. Noyori, *Chem. Commun.*, 1996, 233.

45 S. Hashiguchi, A. Fujii, J. Takehara, T. Ikariya and R. Noyori, *J. Am. Chem. Soc.*, 1995, **117**, 7562–7563.

46 T. Ikariya and A. J. Blacker, *Acc. Chem. Res.*, 2007, **40**, 1300–1308.

47 T. Ikariya and I. D. Gridnev, *Top Catal*, 2010, **53**, 894–901.

48 A. Fujii, S. Hashiguchi, N. Uematsu, T. Ikariya and R. Noyori, *J. Am. Chem. Soc.*, 1996, **118**, 2521–2522.

49 J. Zhang, G. Leitus, Y. Ben-David and D. Milstein, *J. Am. Chem. Soc.*, 2005, **127**, 10840–10841.

50 C. Gunanathan, Y. Ben-David and D. Milstein, *Science*, 2007, **317**, 790–792.

51 D. Milstein, *Top Catal*, 2010, **53**, 915–923.

52 E. Ben-Ari, G. Leitus, L. J. W. Shimon and D. Milstein, *J. Am. Chem. Soc.*, 2006, **128**, 15390–15391.

53 M. Feller, A. Karton, G. Leitus, J. M. L. Martin and D. Milstein, *J. Am. Chem. Soc.*, 2006, **128**, 12400–12401.

54 J. Zhang, G. Leitus, Y. Ben-David and D. Milstein, *Angew. Chem.*, 2006, **118**, 1131–1133.

55 Y. Liang, U. K. Das, J. Luo, Y. Diskin-Posner, L. Avram and D. Milstein, *J. Am. Chem. Soc.*, 2022, jacs.2c08491.

56 H. Li and M. B. Hall, *ACS Catal.*, 2015, **5**, 1895–1913.

57 C. Gunanathan and D. Milstein, *Acc. Chem. Res.*, 2011, **44**, 588–602.

58 L. Schwartsburd, M. A. Iron, L. Konstantinovski, Y. Diskin-Posner, G. Leitus, L. J. W. Shimon and D. Milstein, *Organometallics*, 2010, **29**, 3817–3827.

59 M. A. Iron, E. Ben-Ari, R. Cohen and D. Milstein, *Dalton Trans.*, 2009, 9433.

60 G. Zeng, Y. Guo and S. Li, *Inorg. Chem.*, 2009, **48**, 10257–10263.

61 C. Gunanathan and D. Milstein, *Chem. Rev.*, 2014, **114**, 12024–12087.

62 T. Zell and D. Milstein, *Acc. Chem. Res.*, 2015, **48**, 1979–1994.

63 X. Yang and M. B. Hall, *J. Am. Chem. Soc.*, 2010, **132**, 120–130.

64 S. W. Kohl, L. Weiner, L. Schwartsburd, L. Konstantinovski, L. J. W. Shimon, Y. Ben-David, M. A. Iron and D. Milstein, *Science*, 2009, **324**, 74–77.

65 J. Li, Y. Shiota and K. Yoshizawa, *J. Am. Chem. Soc.*, 2009, **131**, 13584–13585.

66 Y. Sun, C. Koehler, R. Tan, V. T. Annibale and D. Song, *Chem. Commun.*, 2011, **47**, 8349.

67 E. Balaraman, C. Gunanathan, J. Zhang, L. J. W. Shimon and D. Milstein, *Nature Chem*, 2011, **3**, 609–614.

68 D. Tocqueville, F. Crisanti, J. Guerrero, E. Nubret, M. Robert, D. Milstein and N. von Wolff, *Chem. Sci.*, 2022, **13**, 13220–13224.

69 R. Tanaka, M. Yamashita, L. W. Chung, K. Morokuma and K. Nozaki, *Organometallics*, 2011, **30**, 6742–6750.

70 R. Tanaka, M. Yamashita and K. Nozaki, *J. Am. Chem. Soc.*, 2009, **131**, 14168–14169.

71 G. A. Filonenko, R. van Putten, E. N. Schulpen, E. J. M. Hensen and E. A. Pidko, *ChemCatChem*, 2014, **6**, 1526–1530.

72 C. Gunanathan, B. Gnanaprakasam, M. A. Iron, L. J. W. Shimon and D. Milstein, *J. Am. Chem. Soc.*, 2010, **132**, 14763–14765.

73 C. Gunanathan, L. J. W. Shimon and D. Milstein, *J. Am. Chem. Soc.*, 2009, **131**, 3146–3147.

74 S. Tang, Y. Ben-David and D. Milstein, *J. Am. Chem. Soc.*, 2020, **142**, 5980–5984.

75 S. Kar, M. Rauch, G. Leitus, Y. Ben-David and D. Milstein, *Nat Catal*, 2021, **4**, 193–201.

76 L.-P. He, T. Chen, D.-X. Xue, M. Eddaoudi and K.-W. Huang, *Journal of Organometallic Chemistry*, 2012, **700**, 202–206.

77 H. Li, B. Zheng and K.-W. Huang, *Coordination Chemistry Reviews*, 2015, **293–294**, 116–138.

78 T. Chen, L.-P. He, D. Gong, L. Yang, X. Miao, J. Eppinger and K.-W. Huang, *Tetrahedron Letters*, 2012, **53**, 4409–4412.

79 T. Chen, H. Li, S. Qu, B. Zheng, L. He, Z. Lai, Z.-X. Wang and K.-W. Huang, *Organometallics*, 2014, **33**, 4152–4155.

80 L.-P. He, T. Chen, D. Gong, Z. Lai and K.-W. Huang, *Organometallics*, 2012, **31**, 5208–5211.

81 S. Qu, Y. Dang, C. Song, M. Wen, K.-W. Huang and Z.-X. Wang, *J. Am. Chem. Soc.*, 2014, **136**, 4974–4991.

82 Y. Pan, C. Pan, Y. Zhang, H. Li, S. Min, X. Guo, B. Zheng, H. Chen, A. Anders, Z. Lai, J. Zheng and K. Huang, *Chem. Asian J.*, 2016, **11**, 1357–1360.

83 M. D. Fryzuk and P. A. MacNeil, *Organometallics*, 1983, **2**, 682–684.

84 M. D. Fryzuk, P. A. MacNeil and S. J. Rettig, *Organometallics*, 1985, **4**, 1145–1147.

85 M. D. Fryzuk, P. A. MacNeil and S. J. Rettig, *J. Am. Chem. Soc.*, 1987, **109**, 2803–2812.

86 M. D. Fryzuk, C. D. Montgomery and S. J. Rettig, *Organometallics*, 1991, **10**, 467–473.

87 A. Friedrich, M. Drees, M. Käss, E. Herdtweck and S. Schneider, *Inorg. Chem.*, 2010, **49**, 5482–5494.

88 M. Käß, A. Friedrich, M. Drees and S. Schneider, *Angew. Chem. Int. Ed.*, 2009, **48**, 905–907.

89 B. Askevold, J. T. Nieto, S. Tussupbayev, M. Diefenbach, E. Herdtweck, M. C. Holthausen and S. Schneider, *Nature Chem*, 2011, **3**, 532–537.

90 M. Bertoli, A. Choualeb, A. J. Lough, B. Moore, D. Spasyuk and D. G. Gusev, *Organometallics*, 2011, **30**, 3479–3482.

91 A. Friedrich, M. Drees and S. Schneider, *Chem. Eur. J.*, 2009, **15**, 10339–10342.

92 A. N. Marziale, A. Friedrich, I. Klopsch, M. Drees, V. R. Celinski, J. Schmedt auf der Günne and S. Schneider, *J. Am. Chem. Soc.*, 2013, **135**, 13342–13355.

93 M. Nielsen, E. Alberico, W. Baumann, H.-J. Drexler, H. Junge, S. Gladiali and M. Beller, *Nature*, 2013, **495**, 85–89.

94 E. Alberico, A. J. J. Lennox, L. K. Vogt, H. Jiao, W. Baumann, H.-J. Drexler, M. Nielsen, A. Spannenberg, M. P. Checinski, H. Junge and M. Beller, *J. Am. Chem. Soc.*, 2016, **138**, 14890–14904.

95 Y. Suna, M. Z. Ertem, W.-H. Wang, H. Kambayashi, Y. Manaka, J. T. Muckerman, E. Fujita and Y. Himeda, *Organometallics*, 2014, **33**, 6519–6530.

96 W.-H. Wang, J. T. Muckerman, E. Fujita and Y. Himeda, *New J. Chem.*, 2013, **37**, 1860.

97 J. F. Hull, Y. Himeda, W.-H. Wang, B. Hashiguchi, R. Periana, D. J. Szalda, J. T. Muckerman and E. Fujita, *Nature Chem*, 2012, **4**, 383–388.

98 W.-H. Wang, J. T. Muckerman, E. Fujita and Y. Himeda, *ACS Catal.*, 2013, **3**, 856–860.

99 W.-H. Wang, J. F. Hull, J. T. Muckerman, E. Fujita and Y. Himeda, *Energy Environ. Sci.*, 2012, **5**, 7923.

100 G. Zeng, S. Sakaki, K. Fujita, H. Sano and R. Yamaguchi, *ACS Catal.*, 2014, **4**, 1010–1020.

101 H. Kawanami, M. Iguchi and Y. Himeda, *Inorg. Chem.*, 2020, **59**, 4191–4199.

102 M. Iguchi, H. Zhong, Y. Himeda and H. Kawanami, *Chem. Eur. J.*, 2017, **23**, 17788–17793.

103 N. P. van Leest, F. J. de Zwart, M. Zhou and B. de Bruin, *JACS Au*, 2021, **1**, 1101–1115.

104 O. R. Luca and R. H. Crabtree, *Chem. Soc. Rev.*, 2013, **42**, 1440–1459.

105 G. Skara, M. Gimferrer, F. De Proft, P. Salvador and B. Pinter, *Inorg. Chem.*, 2016, **55**, 2185–2199.

106 H. Masui, A. B. P. Lever and P. R. Auburn, *Inorg. Chem.*, 1991, **30**, 2402–2410.

107 K. J. Blackmore, J. W. Ziller and A. F. Heyduk, *Inorg. Chem.*, 2005, **44**, 5559–5561.

108 A. L. Smith, K. I. Hardcastle and J. D. Soper, *J. Am. Chem. Soc.*, 2010, **132**, 14358–14360.

109 W. I. Dzik, J. I. van der Vlugt, J. N. H. Reek and B. de Bruin, *Angew. Chem. Int. Ed.*, 2011, **50**, 3356–3358.

110 T. Wada, K. Tsuge and K. Tanaka, *Inorg. Chem.*, 2001, **40**, 329–337.

111 J. T. Muckerman, D. E. Polyansky, T. Wada, K. Tanaka and E. Fujita, *Inorg. Chem.*, 2008, **47**, 1787–1802.

112 H. Isobe, K. Tanaka, J.-R. Shen and K. Yamaguchi, *Inorg. Chem.*, 2014, **53**, 3973–3984.

113 M.-K. Tsai, J. Rochford, D. E. Polyansky, T. Wada, K. Tanaka, E. Fujita and J. T. Muckerman, *Inorg. Chem.*, 2009, **48**, 4372–4383.

114 J. L. Boyer, J. Rochford, M.-K. Tsai, J. T. Muckerman and E. Fujita, *Coordination Chemistry Reviews*, 2010, **254**, 309–330.

115 A. J. Arduengo, R. L. Harlow and M. Kline, *J. Am. Chem. Soc.*, 1991, **113**, 361–363.

116 M. N. Hopkinson, C. Richter, M. Schedler and F. Glorius, *Nature*, 2014, **510**, 485–496.

117 D. Bourissou, O. Guerret, F. P. Gabbaï and G. Bertrand, *Chem. Rev.*, 2000, **100**, 39–92.

118 F. E. Hahn and M. C. Jahnke, *Angew. Chem. Int. Ed.*, 2008, **47**, 3122–3172.

119 M. Scholl, T. M. Trnka, J. P. Morgan and R. H. Grubbs, *Tetrahedron Letters*, 1999, **40**, 2247–2250.

120 Á. Vivancos, C. Segarra and M. Albrecht, *Chem. Rev.*, 2018, **118**, 9493–9586.

121 H. C. Kolb, M. G. Finn and K. B. Sharpless, *Angew. Chem. Int. Ed.*, 2001, **40**, 2004–2021.

122 V. V. Rostovtsev, L. G. Green, V. V. Fokin and K. B. Sharpless, *Angew. Chem. Int. Ed.*, 2002, **41**, 2596–2599.

123 C. W. Tornøe, C. Christensen and M. Meldal, *J. Org. Chem.*, 2002, **67**, 3057–3064.

124 J. A. Prescher, D. H. Dube and C. R. Bertozzi, *Nature*, 2004, **430**, 873–877.

125 B. T. Worrell, J. A. Malik and V. V. Fokin, *Science*, 2013, **340**, 457–460.

126 P. V. S. Nylund, N. C. Ségaud and M. Albrecht, *Organometallics*, 2021, **40**, 1538–1550.

127 W. Stroek, M. Keilwerth, D. M. Pividori, K. Meyer and M. Albrecht, *J. Am. Chem. Soc.*, 2021, **143**, 20157–20165.

128 R. Lalrempuia, N. D. McDaniel, H. Müller-Bunz, S. Bernhard and M. Albrecht, *Angew. Chem. Int. Ed.*, 2010, **49**, 9765–9768.

129 M. Olivares, C. J. M. van der Ham, V. Mdluli, M. Schmidtendorf, H. Müller-Bunz, T. W. G. M. Verhoeven, M. Li, J. W. (Hans) Niemantsverdriet, D. G. H. Hetterscheid, S. Bernhard and M. Albrecht, *Eur. J. Inorg. Chem.*, 2020, **2020**, 801–812.

130 J. A. Woods, R. Lalrempuia, A. Petronilho, N. D. McDaniel, H. Müller-Bunz, M. Albrecht and S. Bernhard, *Energy Environ. Sci.*, 2014, **7**, 2316–2328.

131 A. Petronilho, M. Rahman, J. A. Woods, H. Al-Sayyed, H. Müller-Bunz, J. M. Don MacElroy, S. Bernhard and M. Albrecht, *Dalton Trans.*, 2012, **41**, 13074.

132 A. Petronilho, J. A. Woods, H. Mueller-Bunz, S. Bernhard and M. Albrecht, *Chem. Eur. J.*, 2014, **20**, 15775–15784.

133 I. Corbucci, A. Petronilho, H. Müller-Bunz, L. Rocchigiani, M. Albrecht and A. Macchioni, *ACS Catal.*, 2015, **5**, 2714–2718.

134 L. Bernet, R. Lalrempuia, W. Ghattas, H. Mueller-Bunz, L. Vigara, A. Llobet and M. Albrecht, *Chem. Commun.*, 2011, **47**, 8058.

135 M. Valencia, H. Müller-Bunz, R. A. Gossage and M. Albrecht, *Chem. Commun.*, 2016, **52**, 3344–3347.

136 M. Valencia, A. Pereira, H. Müller-Bunz, T. R. Belderraín, P. J. Pérez and M. Albrecht, *Chem. Eur. J.*, 2017, **23**, 8901–8911.

137 H. Bruns, M. Patil, J. Carreras, A. Vázquez, W. Thiel, R. Goddard and M. Alcarazo, *Angewandte Chemie International Edition*, 2010, **49**, 3680–3683.

138 C. Würtele, E. Gaoutchenova, K. Harms, M. C. Holthausen, J. Sundermeyer and S. Schindler, *Angew. Chem. Int. Ed.*, 2006, **45**, 3867–3869.

139 B. S. Khan, V. Flores-Romero, J. LeBlanc and G. G. Lavoie, *Organometallics*, 2022, **41**, 2668–2677.

140 S. Herres-Pawlis, U. Flörke and G. Henkel, *Eur. J. Inorg. Chem.*, 2005, **2005**, 3815–3824.

141 D. Petrovic, C. G. Hrib, S. Randoll, P. G. Jones and M. Tamm, *Organometallics*, 2008, **27**, 778–783.

142 Á. Kozma, J. Rust and M. Alcarazo, *Chem. Eur. J.*, 2015, **21**, 10829–10834.

143 J. Börner, U. Flörke, T. Glöge, T. Bannenberg, M. Tamm, M. D. Jones, A. Döring, D. Kuckling and S. Herres-Pawlis, *Journal of Molecular Catalysis A: Chemical*, 2010, **316**, 139–145.

144 X.-Y. Cui, C.-H. Tan and D. Leow, *Org. Biomol. Chem.*, 2019, **17**, 4689–4699.

145 Q. Shi, R. J. Thatcher, J. Slattery, P. S. Sauari, A. C. Whitwood, P. C. McGowan and R. E. Douthwaite, *Chem. Eur. J.*, 2009, **15**, 11346–11360.

146 M. E. Doster and S. A. Johnson, *Angew. Chem.*, 2009, **121**, 2219–2221.

147 J. Slattery, R. J. Thatcher, Q. Shi and R. E. Douthwaite, *Pure and Applied Chemistry*, 2010, **82**, 1663–1671.

148 N. Lentz and M. Albrecht, *ACS Catal.*, 2022, 12627–12631.

149 P. D. W. Boyd, L. J. Wright and M. N. Zafar, *Inorg. Chem.*, 2011, **50**, 10522–10524.

150 C. M. A. Muller, M. V. Babak, M. Kubanik, M. Hanif, S. M. F. Jamieson, C. G. Hartinger and L. J. Wright, *Inorganica Chimica Acta*, 2016, **450**, 124–130.

151 V. Leigh, D. J. Carleton, J. Olguin, H. Mueller-Bunz, L. J. Wright and M. Albrecht, *Inorg. Chem.*, 2014, **53**, 8054–8060.

152 A. J. Bukvic, V. Kesselring, M. Aeschlimann and M. Albrecht, *Inorg. Chem.*, 2023, **62**, 2905–2912.

153 A. J. Bukvic and M. Albrecht, *Inorg. Chem.*, 2022, **61**, 14038–14045.

154 P. Melle, J. Thiede, D. A. Hey and M. Albrecht, *Chem. Eur. J.*, 2020, **26**, 13226–13234.

155 P. Melle, N. Ségaud and M. Albrecht, *Dalton Trans.*, 2020, **49**, 12662–12673.

156 M. Navarro, C. Segarra, T. Pfister and M. Albrecht, *Organometallics*, 2020, **39**, 2383–2391.

157 K. Salzmann, C. Segarra and M. Albrecht, *Angew. Chem. Int. Ed.*, 2020, **59**, 8932–8936.

158 M. Navarro, M. Li, H. Müller-Bunz, S. Bernhard and M. Albrecht, *Chem. Eur. J.*, 2016, **22**, 6740–6745.

CHAPTER II

Efficient additive-free formic acid dehydrogenation with a NNN-ruthenium complex

A new ruthenium complex containing a pyridylidene amine-based NNN ligand was developed as catalyst precursor for formic acid dehydrogenation, which, as a rare example, does not require basic additives to display high activity (TOF ~10,000 h^{-1}). Conveniently, the complex is air-stable, but sensitive to light. Mechanistic investigations using correlation of UV-vis and NMR spectroscopic modifications with gas evolution profiles indicate rapid and reversible protonation of the central nitrogen of the NNN ligand as key step of catalyst activation, followed by an associative step for formic acid dehydrogenation.

P. Knörr, N. Lentz, M. Albrecht, Manuscript in preparation

II.1 Introduction

Storage of renewable energy is one of the key challenges to move towards a cyclic green energy economy and therefore huge efforts are being devoted towards the development of alternative fuels.[1–3] In particular, dihydrogen has been proposed as an ideal energy carrier, as it is accessible through water splitting and only yields benign products upon oxidation in a fuel cell.[4] To avoid the significant downsides of gaseous dihydrogen such as explosivity and low volumetric energy density, the usage of liquid organic hydrogen carriers (LOHCs) as a transient storage vector is highly promising.[5] Small organic molecules can undergo reversible hydrogenation and dehydrogenation cycles and thus allow hydrogen to be safely stored and used.

Formic acid (HCOOH, FA) is one of the most promising liquid organic hydrogen carriers as it features high volumetric energy density, low toxicity and is liquid at room temperature.[6–8] Hence, the dehydrogenation of FA to selectively release dihydrogen has been intensely investigated since the seminal work of Beller and Laurency in 2008.[9–11] Impressive results have been achieved with homogeneous systems, even though many are compromised by insufficient productivity in the absence of basic additives.[12–25] Notable exceptions include the systems of Li[26] and Milstein[27] which are active in aqueous solution and neat FA, respectively, and reach turnover frequencies (TOFs) of 487,500 and 3000 h^{-1} with turnover numbers (TONs) around 2,000,000.

The introduction of cooperative basic functionalities on the ligands has been proposed as an approach to avoid basic additives and to increase catalytic efficiency.[12,28–31] We hypothesized that the presence of a basic amide site on a ligand system, in combination with an electronically flexible pyridylidene (PYE) mojety, which has been shown to positively impact catalytic activity, could access a complex active in additive free FADH. [13,32,33]

Herein, we report a tridentate Ruthenium NNN complex featuring amide and PYE coordination sites. The central amide moiety of the NNN ligand is demonstrated to act as an internal base to ensue high catalytic activity.

II.2 Results and discussion

Reaction of the known,[34] potentially N,N,N-tridentate ligand precursor **1** with $[Ru(cym)Cl_2]_2$ in the presence of Na_2CO_3 afforded complex **2a** (Scheme 1) as a red solid that was purified by filtration over a short pad of basic Al_2O_3. Complex **2b** with a PF_6^- rather than an OTf^- anion was prepared by first generating the neutral ligand from **1** in aqueous KOH solution and extraction into CH_2Cl_2, followed by metalation with $[Ru(cym)Cl_2]_2$ in the presence of $NaPF_6$ and Na_2CO_3. Both complexes **2a** and **2b** are air- and moisture-stable, however they are sensitive to light. Therefore, synthesis and purification were carried out under exclusion of light, and the complexes were stored in the dark.

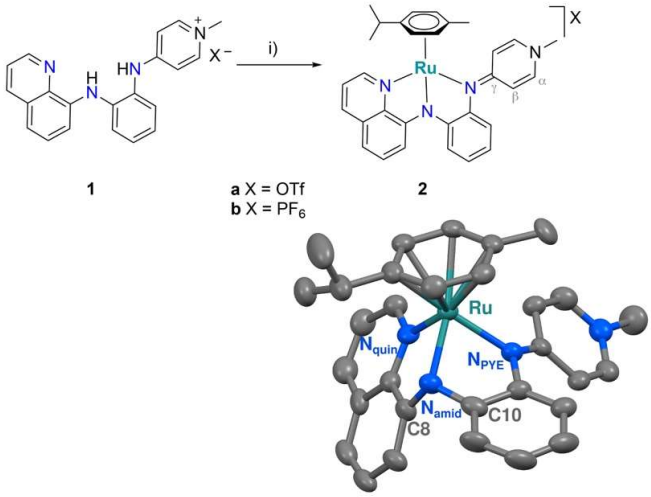

Scheme 1. Synthesis of the NNN Ru complexes **2a** and **2b**. i) $[Ru(cym)Cl_2]_2$, Na_2CO_3, CH_3CN, r.t.; crystal structure of complex **2a** (ellipsoids at 50% probability level. hydrogen atoms and OTf^- anion omitted for clarity). Selected bond lengths (Å) and angles (deg): Ru–N_{quin} 2.089(6), Ru-N_{amid} 2.068(5), Ru–N_{PYE} 2.123(6), C8–N_{amid}–C10 115.7(6), Ru1–N_{amid}–C10 108.3(5), Ru–N_{amid}–C8 114.4(5), N_{quin}–Ru–N_{amid} 78.6(2), N_{amid}–Ru–N_{PYE} 75.7(2), N_{quin}–Ru–N_{PYE} 93.3(2).

Complex formation was indicated in HR-MS analysis by the diagnostic *m/z* signals at 561.1575 (561.1587 calculated for $[\mathbf{2a}-OTf]^+$). In ^1H NMR spectroscopy, complexation led to the disappearance of the two NH resonances of the ligand precursor **1** at δ_H = 10.12 and 8.63, and to desymmetrization of the *i*Pr group of the cymene ligand into two doublets at δ_H = 0.89 and 0.86 for the CH_3 protons. Moreover, the quinoline CH resonances underwent significant downfield shifts (*e.g.* $C_{quin}H$ from δ_H = 9.03 in **1** to δ_H = 9.43 in **2a**), in agreement with ruthenium coordination of the quinoline nitrogen. Likewise, coordination of the PYE site was inferred from the characteristic upfield shift of the N_{pyr}–CH_3 resonance from δ_H = 3.86 to 3.48 upon

ruthenation. Collectively, these data strongly support a tridentate coordination of the ligand to ruthenium with all nitrogens deprotonated. The ^{1}H NMR spectrum of complex **2b** is identical to that of **2a**, yet ^{19}F NMR spectroscopy shows the diagnostic doublet at δ_F = –72.94 for the PF_6^- anion, while **2a** features a singlet at δ_F = –79.31 due to the OTf^- anion. The indistinguishable ^{1}H NMR spectra of **2a** and **2b** indicate that the counterions are not strongly interacting with the complex cation in CD_3CN solution.

X-ray diffraction analysis of single crystals of **2a**, grown by Et_2O/CH_2Cl_2 vapor diffusion, unambiguously confirmed the proposed *N,N,N*-tridentate coordination mode of the substituted PYE ligand to the Ru(cym) fragment in a facial mode (Scheme 1.). The PYE heterocycle is slightly twisted out of the plane of the central phenylene ring by 36.22°. The C–C and C–N bond distances in the PYE heterocycle are consistent with considerable double bond localization in the C_α–C_β bond (average 1.36(1) Å), while the C_β–C_γ bonds are significantly longer (average 1.42(1) Å, indicative of a predominantly quinoidal configuration of the PYE unit in the solid state with a neutral N_{PYE} coordinated to ruthenium. The 360° sum of the bond angles around N_{PYE} also suggest sp^2 hybridization, identical to N_{quin}. In contrast, the central amide shows considerable sp^3 character with bond angles adding up to just 338°, pointing to a lone pair at N_{amid}. Notably, the NNN-tridentate coordination imparts a three-legged piano-stool geometry around Ru that is markedly distorted towards a four-legged geometry with a vacant site opposite to N_{amid} (Fig. 9).

When exposed to light, solutions of complex **2** gradually darkened, irrespective of the counterion (PF_6^- or OTf^-) or the solvent (DMSO, acetone, CH_2Cl_2, MeCN). When kept under otherwise inert conditions, light-induced decomposition was indicated in ^{1}H NMR spectroscopy by the appearance of resonances characteristic for free cymene, *e.g.*, a doublet at δ_H = 1.17 in DMSO-d_6 (*cf* two doublets at δ_H = 0.82 and 0.76 for **2a**; Fig. 1). Simultaneously a new set of signals emerged in the aromatic region for the *N,N,N*-tridentate ligand that are distinct from the ligand precursor. We therefore tentatively attribute these signals to the formation of a solvento complex $[Ru(NNN)(DMSO)_3]^+$. When complex **2** was exposed to light in the presence of oxygen, again decoordination of cymene was inferred. In addition, a new species emerged with broad and poorly resolved signals, suggesting metal oxidation and the formation of a paramagnetic Ru(III) species. The same behavior was observed when air was introduced into a solution of the putative solvent complex $[Ru(NNN)(DMSO)_3]^+$. ESI mass spectroscopy of solutions of complex **2a** after exposure to light and air revealed an *m/z* signal at 459.0376 (459.0395 calculated for $[\mathbf{2a}+O_2-cym-OTf]^+$) consistent with a higher-valent ruthenium dioxo or oxyl species that preserves the NNN ligand. These data and the absence of any detectable ligand precursor suggest that the NNN-ligand remains coordinated to the ruthenium during the various ligand exchange and metal oxidation processes. In contrast, when complex **2** was protected from light, no loss of cymene ligand was observed for weeks, even when the solutions were aerated, indicating that cymene dissociation is key for metal oxidation processes. For

application, any oxidized species is conveniently removed by filtration of the complex over a short pad of basic Al_2O_3 (acetone/CH_2Cl_2 1:2).

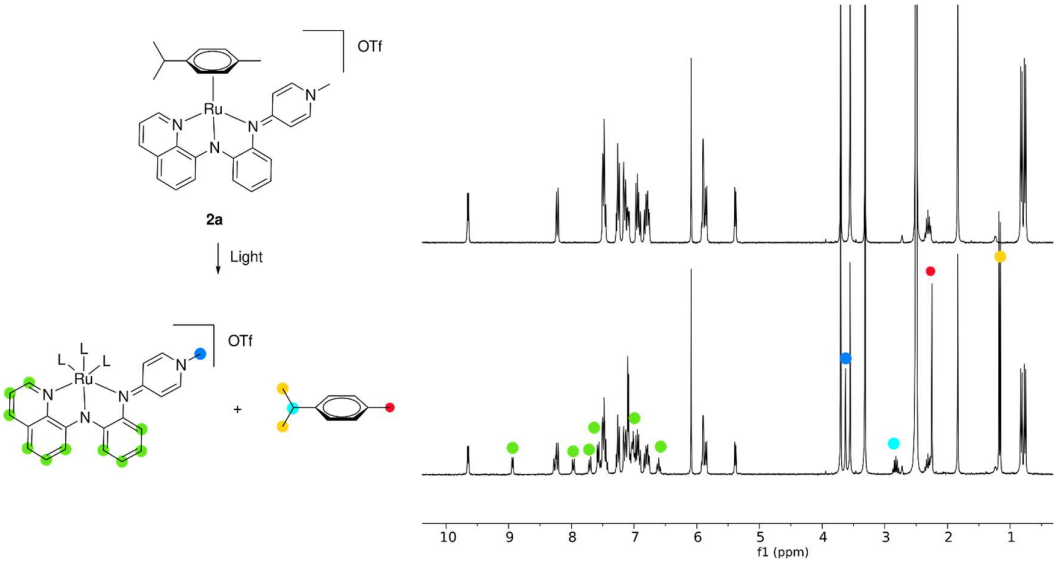

Figure 1: ^{1}H NMR spectra of **2a** in DMSO-d_6 under N_2 and exclusion of light (top), and after exposure to sunlight for 1 h (bottom).

Complexes **2a** and **2b** are catalytically active in the dehydrogenation of FA. Initial reactions were performed by adding FA to a solution of **2a** at 80 °C and subsequent monitoring of the amounts of evolved gas (Fig. 2). Several solvents were tested that were previously used in FA dehydrogenation catalysis, including dioxane, DMSO, water, propylene carbonate, and a mixture of *t*BuOH and toluene (1:1 v/v; Table 1).[12,26,31,35,36] In water the complex was completely inactive (entry 1). Highest catalytic activities were observed in DMSO and in dioxane, with initial turnover frequencies (TOFs) around 2,000 h^{-1} (entries 2,3). A mixture of toluene and *t*BuOH suppressed activity considerably (TOF = 710 h^{-1}; entry 4). Interestingly, using propylene carbonate as solvent completely changed the reaction profile (Fig. 2). While the initial activity was low (TOF = 200 h^{-1}), it gradually increased over the course of about one hour to reach an appreciable TOF_{max} = 1300 h^{-1} (entry 5). A similar unusual gas evolution profile has been reported previously with carbonate solvents.[36] It may be rationalized by either a slow catalyst activation in propylene carbonate, by initial hydrogenation of the solvent and formation of *n*PrOH as a co-solvent, or by a gradual pH increase upon formic acid consumption to an optimal range with highest catalyst performance. To probe these scenarios, another batch of FA was added after completion of the initial run. These experiments resulted in a similar gas evolution profile with gradually increasing catalytic activity, albeit at lower overall rate. This behavior is consistent with a pH-dependent catalyst performance rather than solvent hydrogenation or a long induction due to catalyst activation. Irrespective of its exact role, propylenecarbonate lowers the activity of **2a** considerably when compared to dioxane or DMSO. The latter solvent

is preferable over dioxane as it is non-toxic, more sustainable,[37] features a low vapor pressure, and a high boiling point.

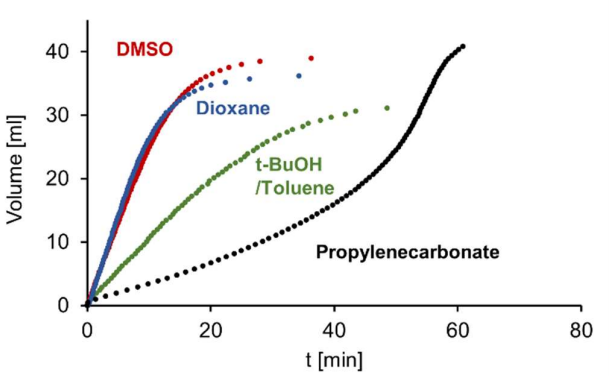

Figure 2: Time-dependent gas evolution profiles for FA dehydrogenation with **2a** in different solvents. Reaction conditions: FA (40µl), [Ru] (0.2 mol%), solvent (1.2 ml), 80°C under N_2. Representative single runs are shown but catalytic runs were performed at least twice to ensure reproducibility. H_2O profile is excluded as no activity was observed.

Table 1: FA dehydrogenation catalysis with **2a** in different solvents [a)]

Entry	Solvent	mol% **2a**	TOF_{max} [b)]	TON [b)]
1	H_2O	0.2	---	0
2	Dioxane	0.2	2,000	380
3	DMSO	0.2	2,000	420
4	t-BuOH/Toluene	0.2	710	310
5	Propylene carbonate	0.2	1,300	440
6	DMSO	0.02	9,200	1400
7	DMSO	0.002	1,300	2200

a) Reaction conditions: FA (40 µl), complex **2a**, solvent (1.2 mL), 80 °C under N_2; b) TON and TOF determined based on evolved gas volume, see ESI for details

Complexes **2a** and **2b** show identical conversion profiles and catalytic performance in DMSO, indicating no significant influence of the counterion on the catalytic cycle. Performing FA dehydrogenation at higher temperatures notably increases TOFs from 2,000 h^{-1} at 80 °C to 3,200 h^{-1} at 90 °C and 7,000 h^{-1} at 100 °C (Fig. 3). Tenfold decrease in pre-catalyst loading to 0.02 mol% increased the TOF to 9,200 h^{-1} (Table 1, entry 6), though a further lowering to 0.002 mol% significantly impeded catalyst turnover (TOF = 1,300 h^{-1}; entry 7). Based on these turnover frequencies, complex **2a** is showing outstanding activity and outperforms other ruthenium-based catalysts, *e.g.* Milstein's system features a TOF around 3,000 h^{-1}.[27] While

iridium catalysts show generally an even higher activity with TOFs that are up to 2 orders of magnitude larger,[26] ruthenium is about 100 timess less scarce and about 10 times cheaper. Notably, under dilute catalyst conditions, the maximum turnover number (TON) of **2a** was just 2200, which is a significant limitation in comparison to the Milstein catalyst with 1,7 M TON.

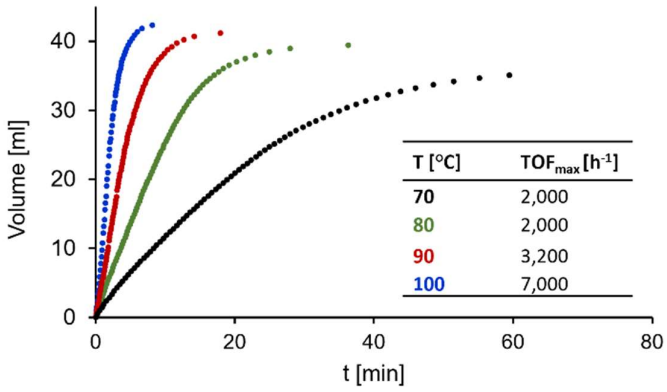

Figure 3: Time-gas evolution profiles for FA dehydrogenation with **2a** at different temperatures. Reaction conditions: FA (40µl,), [Ru] (0.2 mol%), Solvent (1.2 ml), N_2 atm.

Arrhenius and Eyring analyses of the initial rates of these temperature-dependent catalytic runs revealed an activation energy E_a = 68 ±1 kJ mol^{-1}, an enthalpy of activation $\Delta H^{\ddagger}$ = 65 ±1 kJ mol^{-1} and an entropy of activation $\Delta S^{\ddagger}$ = –177 ±3 J (K mol)$^{-1}$ (Fig. 4, 5). The highly negative $\Delta S^{\ddagger}$ suggests an associative process in the turnover limiting step, which might entail, for example, the interaction between a putative ruthenium hydride and FA, or adduct formation of the ruthenium complex and *in situ* formed formate

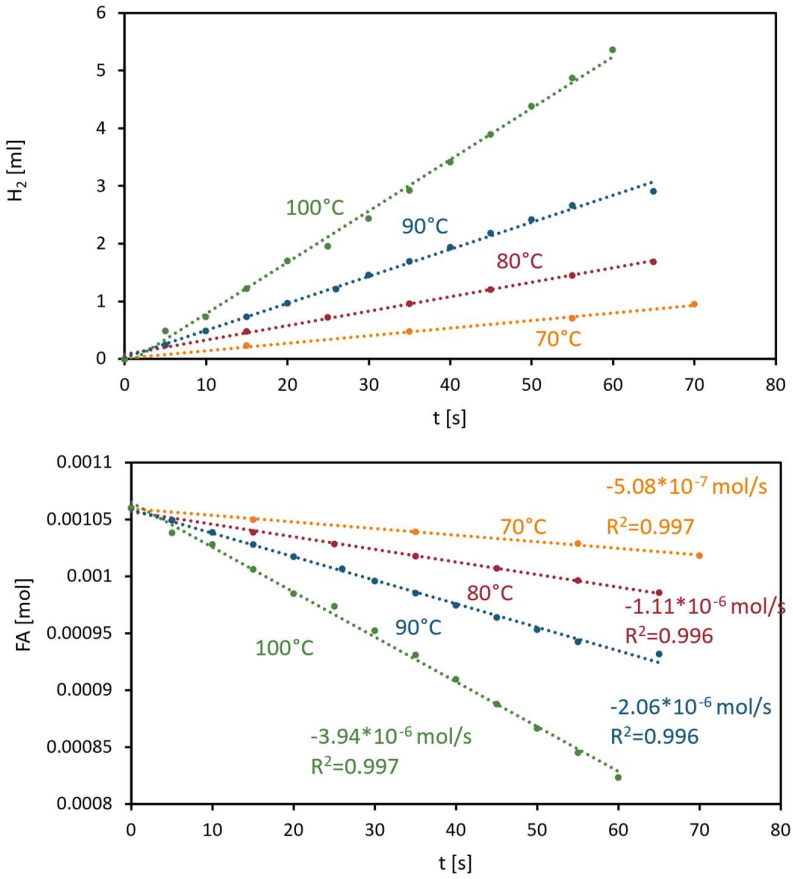

Figure 4: *Top*: Initial production of H_2 at different temperatures. H_2 production was measured with the BlueV count volumetric gas counter. The volume was halved as the evolved gas consists of 1:1 CO_2/H_2 mixture; *bottom*: FA consumption at different temperatures. The FA concentrations were calculated based on initially injected amount minus consumed amount based on evolved gas volume. Reaction condition: **2a** (0.01 mol%), FA (1.06 mmol) and DMSO (1.2 mL) at indicated temperature.

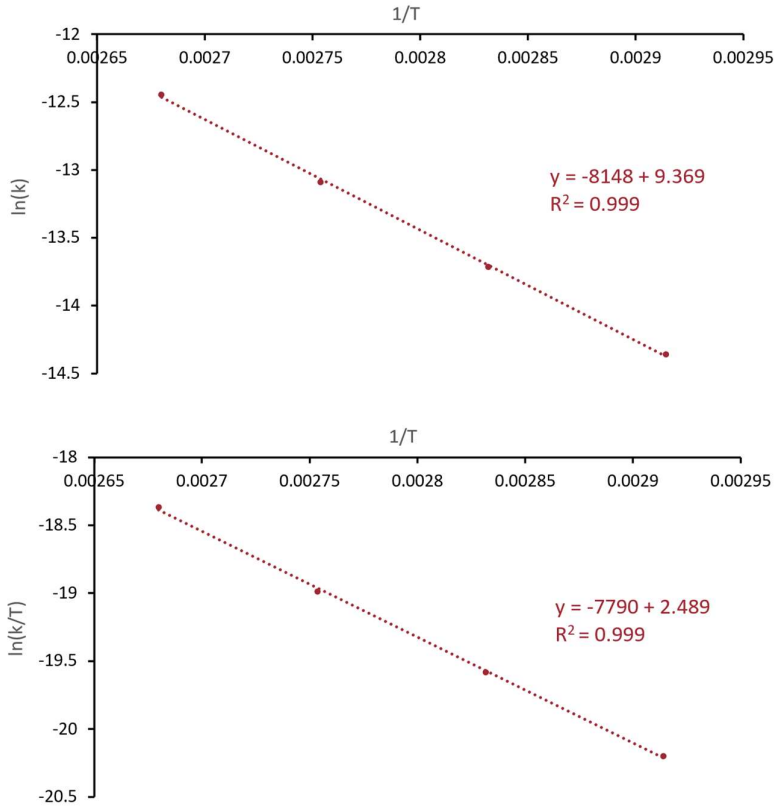

Figure 5. Arrhenius plot (top) and Eyring plot (bottom), form rates deduced from temperature dependent catalysis (see slopes in Fig. 4)

Catalytic dehydrogenation with complex **2a** is accompanied by distinct color changes of the reaction solution. The initially red complex solution turns immediately purple upon addition of FA at elevated temperatures and then gradually changes to orange. Monitoring the catalytic reaction by *in-situ* UV-vis spectroscopy indicates that the color change from the red complex solution (λ_{max} = 500 nm) to the purple solution (λ_{max} = 550 nm) is essentially instantaneous (<1 s) and coincides with the start of gas evolution, *i.e.* catalytic activity (Fig. 6, 7). After about 8 min, a new band starts to emerge (λ_{max} = 445 nm). The gas evolution rate decreases as this band is growing, and the corresponding species is persistent at the end of the reaction when gas evolution ceased, indicating that the orange Ru species is catalytically inactive.

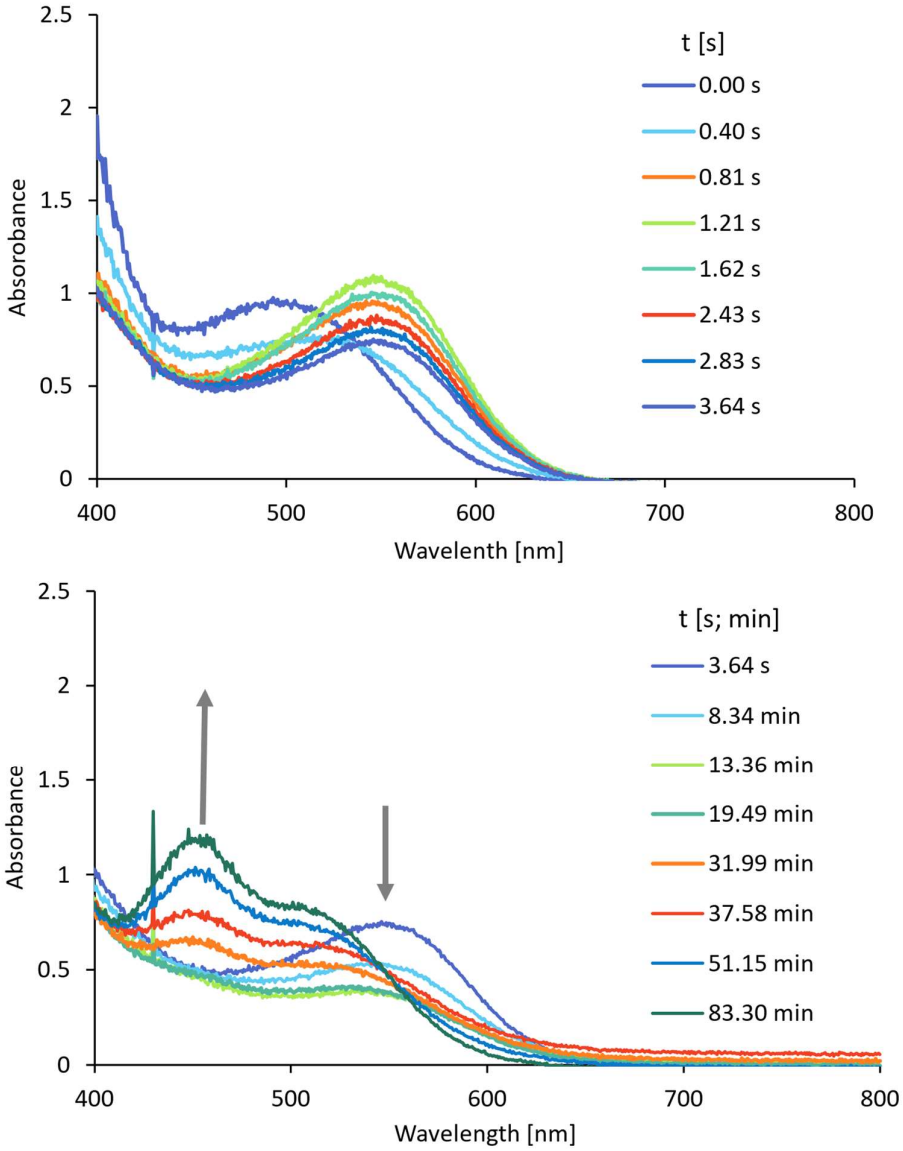

Figure 6. Catalytic reaction at 80 °C followed by in situ UV-vis spectroscopy. Inital reaction (*top panel*), later stages (*bottom panel*). Catalysis was carried out according to general procedure but upscaled to accommodate the UV-probe. Reaction conditions: **2a** (0.1 mol%, 7.53 mg, 10.6 µmol), FA (0.4 mL, 10.6 mmol) and DMSO (10 mL) at 80°C. Gas evolution was measured concomitantly and is shown in Fig. 7**.**

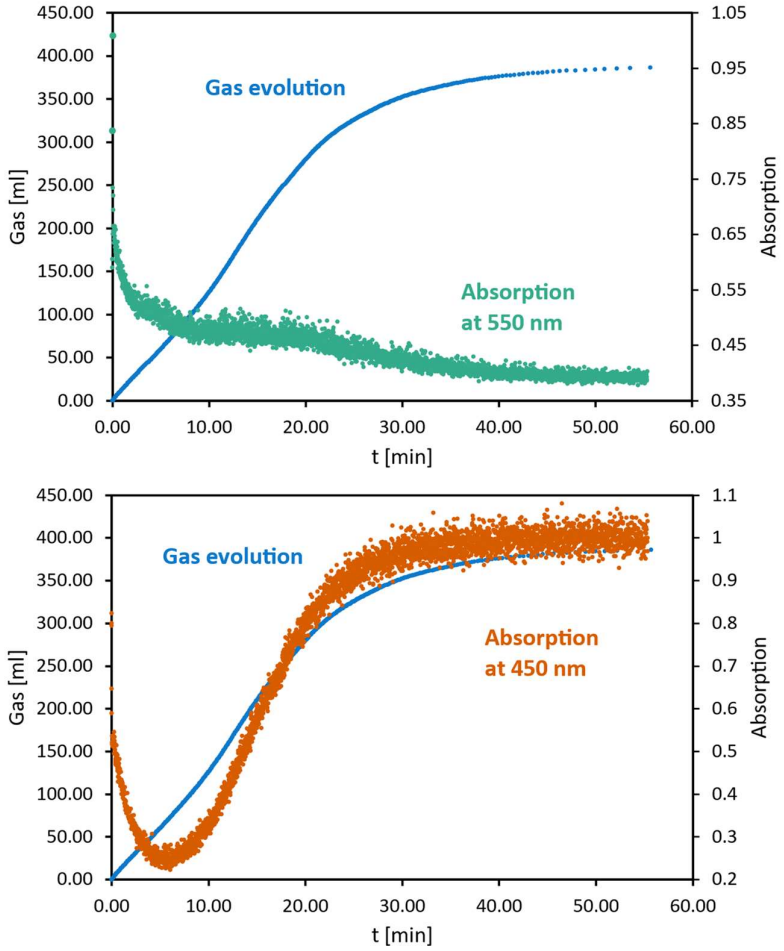

Figure 7. Gas evolution *vs* absorption (absorption data measured in situ, see also Fig. 6).

Further details unveiled upon lowering the temperature of the catalytic reaction to 30 °C. At this temperature, formation of the active purple species is not instantaneous anymore, and instead, an immediate color change from red to yellow was noted upon formic acid addition, followed by a gradual color change to purple. The yellow species is characterized by the disappearance of the absorbance at 500 nm from complex **2a**, with only intra-ligand charge transfer bands present in the UV region (Fig. 8). No gas evolution was recorded at this stage. The evolution of the yellow species, has been attributed to protonation of the N,N,N-ligand at its central nitrogen, which is supported by reactions performed with catalytically innocent acids such as TFA or HOTf (TFA = CF_3COOH, HOTf = CF_3SO_3H). Thus, when treating a DMSO solution of the ruthenium complex **2a** with TFA (1 eq) instead of formic acid induced the same instantaneous color change from red to yellow and yielded **[2a–H]$^+$** (Scheme 2). The ^{1}H NMR spectrum of **[2a–H]$^+$** revealed a new resonance at δ_H = 11.8, consistent with an acidic NH functionality. Protonation of the central Ar–N–Ar nitrogen is deduced based on only relatively small chemical

shifts of the heterocyclic protons. It agrees with the considerable pyramidalization and sp^3 hybridization of the N_{amid} as evidenced by the molecular structure of **2a**, and was ultimately confirmed by a single-crystal X-ray diffraction of the PF_6^- salt of **[2a–H]$^+$** (Scheme 2, Fig. 9). While the global structure of **[2a–H]$^+$** is almost identical to that of **2a**, all bonds to N_{amid} are significantly elongated (*e.g.* Ru– N_{amid} is 2.068(5) Å in **2a** *vs.* 2.132(3) Å in **[2a–H]$^+$**) and thus corroborate protonation of this nitrogen. The marked deshielding of the NH resonance (*cf.* δ_H = 8.4 in **1**) suggests that also in solution, the nitrogen remains coordinated to ruthenium upon protonation. The moderate downfield shift of the aromatic signals, *e.g.* the *ortho* CH_{quin} from δ_H = 9.64 to 9.96, is in agreement with increased N_{quin}-to-Ru charge transfer and points to some compensation of the reduced amine basicity upon protonation. The same spectroscopic changes were noted when treating **2a** with 10 eq HOTf, indicating selective protonation of only one nitrogen (Fig. 10). Addition of Na_2CO_3 fully reverses the color change back to red and restores the ^{1}H NMR spectrum of **2a**, identifying protonation as a completely reversible process.

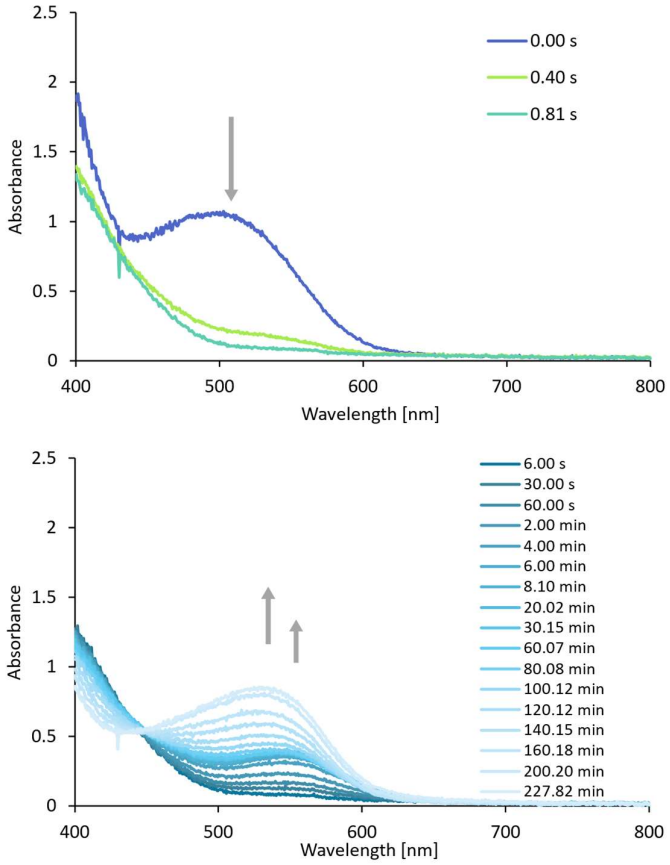

Figure 8. Catalytic reaction at 30 °C monitored by *in situ* UV-vis spectroscopy. Reaction condition: **2a** (0.1 mol%, 7.53 mg, 10.6 µmol), FA (40 µl, 10.6 mmol) and DMSO (10 mL) at 30 °C. Gas evolution was measured concomitantly and is shown in Fig 11

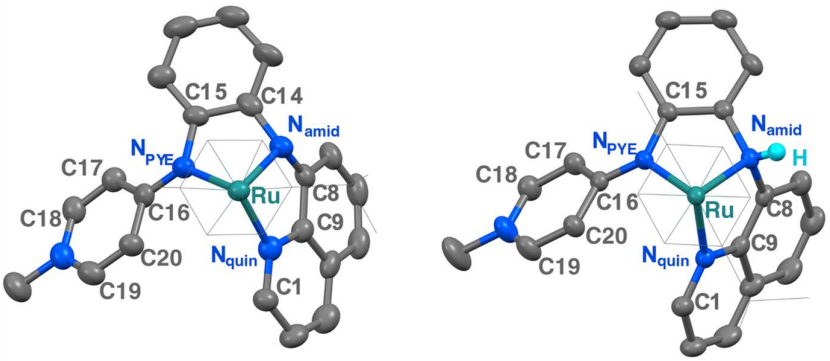

Figure 9. Crystal structure representations of **2a** and **[2a-H]⁺**, perspective down the cymene centroid–Ru axis. All ellipsoids at 50% probability level, PF_6^- counteranions and most hydrogen atoms omitted for clarity, p-cym depicted as wireframe for clarity.

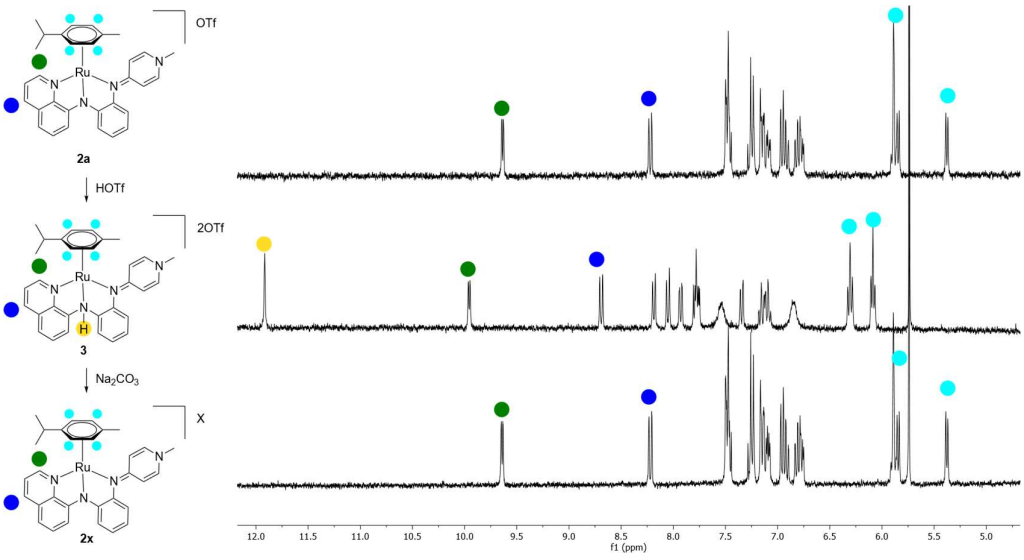

Figure 10. ^{1}H NMR spectra of **2a** (top), of **2a** after addition of HOTf to form complex **[2a–H]⁺** (middle), and restoring complex **2a** upon adding Na_2CO_3 (bottom).

The subsequent appearance of the purple color features an isosbestic point at 440 nm and is again accompanied by gas evolution, indicating a direct conversion of **[2a–H]⁺** into the catalytically competent species. Within the inital 7 min λ_{max} is located at 550 nm as observed at 80 °C, and gas evolution is linear. The absorption then slowly decreases and the maximum shifts to 530 nm during the subsequent 60 min, and gas evolution gradually ceases (Fig. 11). Hence the absorption shift relates to the formation of a catalytically inactive species. In agreement, NMR signals due to free p-cymene became visible at this stage of gas evolution, thus indicating a pathway for catalyst deactivation.

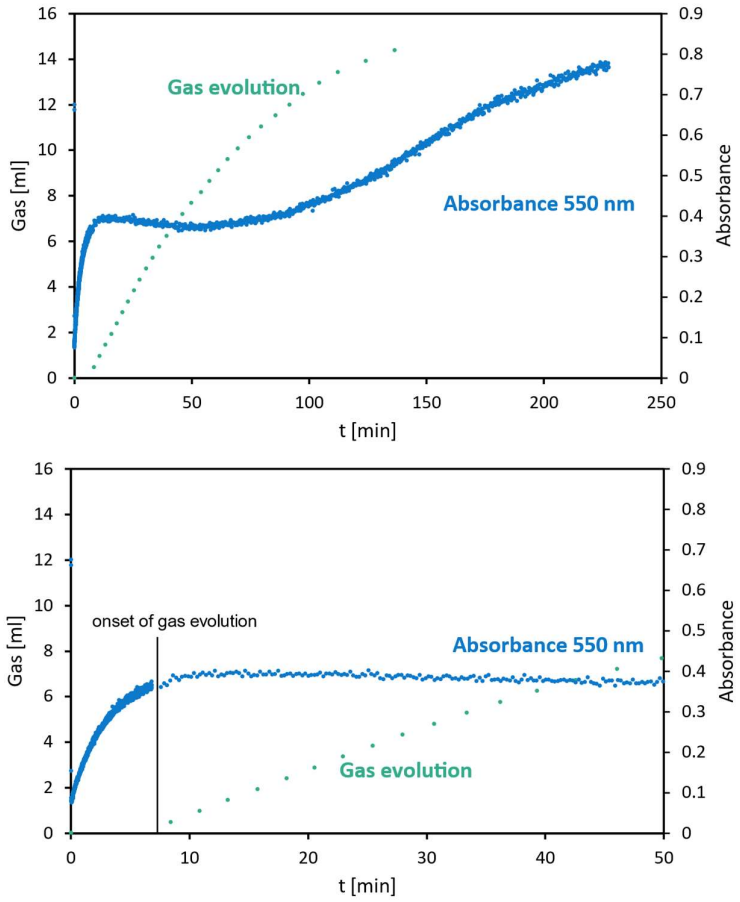

Figure 11: Gas evolution profile *vs* changes in absorption. Full profile (top), expansion of the profile during the inital 50 min (bottom; absorptions at 550 nm extracted from spectra, see Fig. 8).

Structural information about the purple catalytically active species has been gathered from the reaction of complex **2a** with 180 eq FA in DMSO–d_6 to mimic catalytic conditions (Fig. 12). Addition of FA induces again an instantaneous color change to yellow and NMR spectroscopy shows the formation of **[2a-H]$^+$**. In addition, a new species starts to emerge which features signals for the N,N,N-ligand and the cymene that are only slightly shifted with respect to **[2a–H]$^+$**, suggesting robust coordination of both ligands. The evolution of this component, tentatively attributed to the formic acid complex **3** (Scheme 2), increases gradually and is persistent for over 2 h, during which gas evolution is essentially linear under these conditions (Fig. 12, 13). Of note, the NNN-ligand is likely protonated as indicated by a strongly deshielded singlet at δ_H = 10.28 ppm, which is absent when the reaction is performed with DCOOD instead of HCOOH. Therefore, N_{amid} is coordinating only weakly, if at all, to the ruthenium center in complex **3**. While the tridentate chelation of the NNN-ligand principally might provide space for a small ligand to

bind to the ruthenium center in a distorted square-pyramidal geometry (Fig. 9), hemilability of the central nitrogen is more likely to accommodate the formate and is not unprecedented.[34]

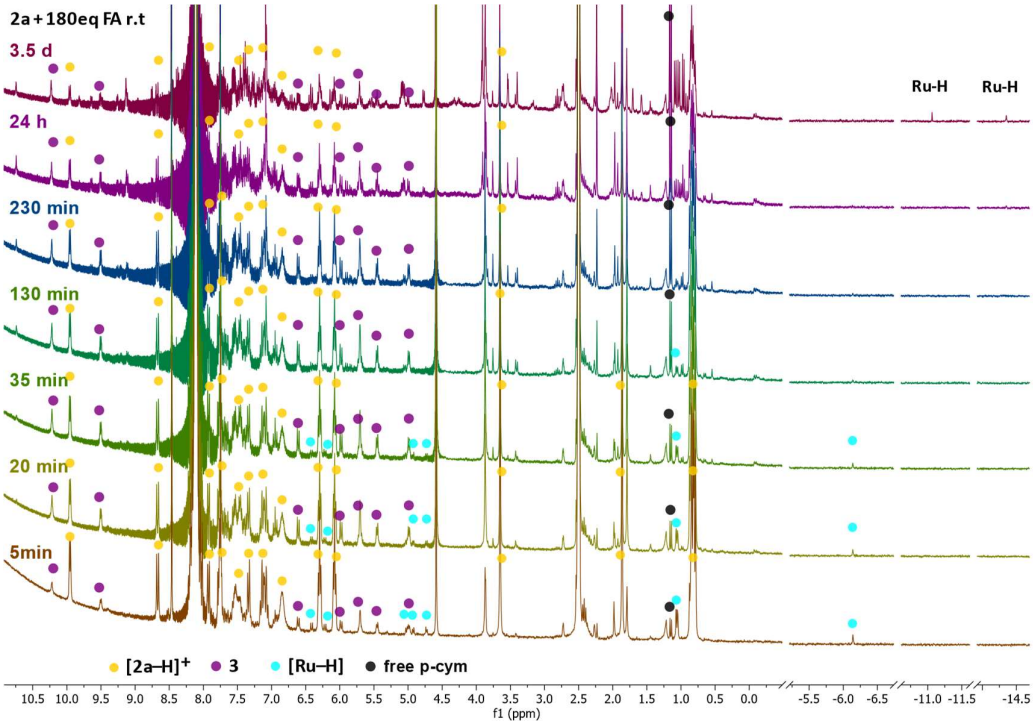

Figure 12. Stacked ^{1}H NMR spectra after addition of 180 eq FA to **2a**. Conditions: DMSO-d_6 (0.6 mL), **2a** (4 mg, 5.64 µmol), FA (40 µl, 1.06 mmol). Signals assigned to **3** (•), **[2a-H]$^+$** (•) and the **[Ru-H]** (•) are marked.

In the high-concentration regime of the NMR experiment, additionally, trace amounts of a hydride species are present at the initial stages of the reaction, with a diagnostic signal at δ_H = –6.14 and corresponding resonances in the cymene and NNN ligand regions (Fig. 12). After about 20 min, this hydride species is fully consumed, though gas evolution continues for another two hours in an almost linear regime, suggesting that this hydride complex is not related to the catalytically active species. This hydride side product is also visible in mixtures resulting from stoichiometric reactions of **2a** with 1 eq formic acid, or when treating **[2a–H]$^+$** with stoichiometric quantities of lithium formate .

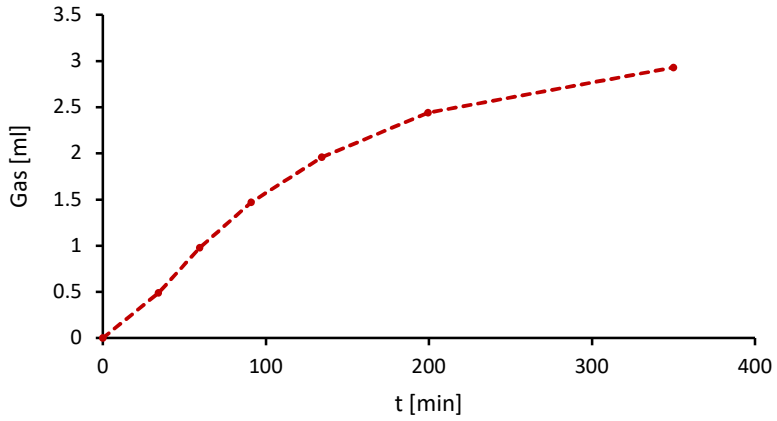

Figure 13. Gas evolution from NMR tube with deuterated FA. Usual preparation of NMR sample but the tube was connected to a blueVcount volumetric gas measurement device. Conditions: DMSO-d_6 (0.6 mL), **2a** (4 mg, 5.64 µmol), DCOOD (40 µL, 1.06 mmol), r.t.

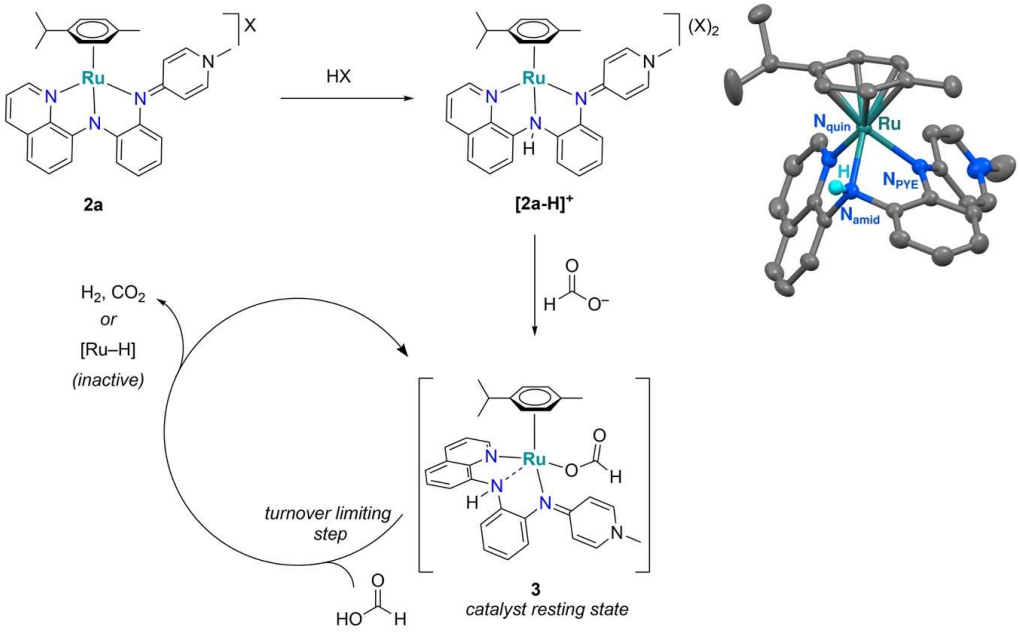

Scheme 2: Suggested pathway for the activation of complex **2** for catalytic FA dehydrogenation and thermal ellipsoid plot of **[2a-H]⁺** (50% ellipsoids, the two PF_6^- counteranions, all carbon-bound hydrogen atoms, and co-crystallized CH_2Cl_2 molecule omitted for clarity).

The relevance of these room temperature studies was validated by performing a formic acid dehydrogenation experiment at 80 °C for just 1 min followed by immediate cooling. The corresponding ^{1}H NMR spectrum is essentially identical to that from room temperature reactions after 35 min, supports the variable temperature UV-vis data (vide supra). When FA is almost fully consumed additional hydridic resonances at δ_H = –11.06 and –14.3 are observed, indicating that upon consumption of all formic acid, either cymene is lost or the tridentate coordination mode of the NNN ligand is altered.

Overall, these spectroscopic data suggest fast N-protonation as the initial catalyst activation step. Proton transfer to the ruthenium-bound amide nitrogen is pH controlled and fast in the presence of excess FA or a strong acid. This protonation is assumed to weaken the Ru–N_{amid} bond, and thus allow for formate coordination. This purple species **3** is considered the catalyst resting state. While it is tempting to propose a β-hydrogen elimination from this resting state to form a hydride species, such a turnover-limiting step would imply a highly positive entropy of activation because of the concomitant release of CO_2, which is incompatible with the large negative value of $\Delta S^{\ddagger}$ (*vide supra*). We therefore propose the formation of a highly ordered adduct with a second equivalent of formic acid to facilitate the hydride formation (Scheme 2). Note that due to the distal location of the acidic proton at N_{amid}, from the putative ruthenium-bound hydride, intramolecular elimination of H_2 seems much less likely compared to protonation of the hydride by extraneous formic acid. In this latter scenario, N_{amid} protonation is essential for opening up a coordination site at the ruthenium center during catalyst activation, but not for cooperative formic acid activation or H_2 release.

II.3 Conclusion

We disclose here a ruthenium complex containing an easily accessible NNN ligand system for efficient formic acid dehydrogenation. The catalytic system shows very high catalytic activity with turnover frequencies that surpass other additive-free ruthenium catalyst for formic acid dehydrogenation. Mechanistic investigations indicate a purple phase as catalytically active species, which is defined by a ruthenium system that still comprises the cymene and the NNN ligand, though the latter presumably only in bidentate coordination mode. While the system is highly active, its longevity is mediocre. This limitation may be addressed by ligand modifications, which are straightforward because of the convenient and modular ligand synthesis.

II.4 Experimental

General

Ruthenium complexes were synthesized under exclusion of light. Ligand precursor **1a** was synthesized according to a published procedure.[34] All other reagents were commercially available and used as received unless specified. NMR spectra were recorded at 25 °C on Bruker spectrometers operating at 300 or 400 MHz (^{1}H NMR), 282 or 376MHz (^{19}F NMR), and 75 or 100 MHz (^{13}C{^{1}H} NMR), respectively. Chemical shifts (δ in ppm, coupling constants *J* in Hz) were referenced to residual solvent signals (^{1}H,^{13}C). Assignments are based on homo- and hetero nuclear shift correlation spectroscopy. High resolution mass spectrometry was carried out by the DCBP mass spectrometry group at the University of Bern with with a Thermo Scientific LTQ Orbitrap XL (ESI-TOF). Elemental analyses were performed on a Thermo Scientific Flash 2000 CHNS-O elemental analyzer by the DCBP Microanalytic Laboratory.

Complex 2a

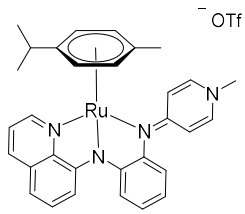

Under nitrogen atmosphere and under exclusion of light, [Ru(*p*-cymene)Cl_2]$_2$ (128.5 mg, 0.21 mmol), ligand precursor **1a** (200 mg, 0.42 mmol) and Na_2CO_3 (444 mg, 4.2 mmol) were stirred in degassed CH_3CN (11 mL) for 16 h. The crude mixture was filtered, and all volatiles were removed under reduced pressure. The residue was dissolved in CH_2Cl_2 and filtered over a short pad of basic Al_2O_3. The complex was eluted with a mixture of CH_2Cl_2 and acetone (2:1; 60 mL) as a red solution. All volatiles were evaporated under reduced pressure and the solid redissolved in a minimal amount of CH_2Cl_2. Et_2O was then added until a red solid precipitated. The supernatant was removed and the solid washed with Et_2O (2 × 10 mL) and pentane (2 × 10 mL) to yield complex **2a** as a red solid (190 mg, 64%). Slow diffusion of Et_2O into a solution of complex **2a** in CH_2Cl_2 gave crystals suitable for X-ray diffraction analysis. ^{1}H NMR (300 MHz, CD_3CN) δ 9.44 (dd, $^{3}J_{HH}$ = 5.1, $^{4}J_{HH}$ = 1.3 Hz, 1H, H_{Quin}), 8.14 (dd, $^{3}J_{HH}$ = 8.4, $^{4}J_{HH}$ = 1.3 Hz, 1H, H_{Quin}), 7.48 (dd, $^{3}J_{HH}$ = 7.6, $^{4}J_{HH}$ = 1.4 Hz, 1H, H_{Ar}), 7.38 (dd, $^{3}J_{HH}$ = 8.4, 5.1 Hz, 1H, H_{Quin}), 7.32–7.23 (m, 2H, $H_{PYE\ \alpha}$, H_{Quin}), 7.18 (dd, J_{HH} = 3.5, 1.3 Hz, 1H, H_{Ar}), 7.16 (dd, J_{HH} = 3.3, 1.3 Hz, 1H, H_{Ar}), 7.02 (dd, J_{HH} = 7.6, 3.1 Hz, 1H, H_{Ar}), 7.00–6.92 (m, 3H, $H_{PYE\ \alpha}$, 2 H_{Ar}), 6.83 (td, J_{HH} = 7.6, 1.4 Hz, 1H, H_{Ar}), 6.78 (dd, J_{HH} = 7.7, 3.1 Hz, 1H, H_{Ar}), 5.78–5.71 (m, 2H, H_{cym}), 5.69–5.62, 5.18–5.12 (2 × m, 1H, H_{cym}), 3.48 (s, 3H, N–CH_3), 2.37 (septet, $^{3}J_{HH}$ = 6.9 Hz, 1H, $CHMe_2$), 1.91 (s, 3H, cym–CH_3), 0.87, 0.83 (2 × d, $^{3}J_{HH}$ = 6.9 Hz, 3H, (CH_3)$_2$CH). ^{13}C NMR (101 MHz, CD_3CN) δ 160.92, 160.25, 159.64 (3 × C_{Ar}), 154.68, 154.62(1 ×CH_{Quin}, 1 × C_{Ar}), 148.23, 141.47, 140.86 (3 × C_{Ar}), 138.24(CH_{Quin}), 131.01, 129.98, 125.52, 124.50 (4 × C_{Ar}), 123.20 (CH_{Quin}), 122.78, 120.15, 119.17, 116.57, 114.62, 109.51 (6 × C_{Ar}), 103.18, 102.58 ((C_{cym}–*i*Pr, C_{cym}–Me), 88.16, 87.93, 86.54, 84.72 (4 × C_{cym}–H), 43.84 (N–CH_3), 31.31 ($CHMe_2$)), 22.77, 21.73(2 × CH(CH_3)$_2$), 18.54 (cym–CH_3). ^{19}F NMR (376 MHz, CD_3CN) δ -79.31 (OTf). HR-MS (m/z): Calculated for

[M–OTf] = 561.1587 found 561.1575. Anal. Calc. (%) for $C_{32}H_{31}F_3N_4O_3RuS$: C 54.15, H 4.40, N 7.89; found C 53.73, H 4.35, N 7.63.

Complex 2b

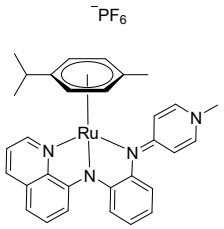

Ligand precursor **1a** (400 mg, 0.84 mmol), was stirred in a biphasic mixture of aqueous KOH (1 M, 10 mL) and CH_2Cl_2 (20 mL) for 15 min. The CH_2Cl_2 phase was separated and washed with 0.1 M KOH solution (20 mL) followed by water (20 mL). The organic phase was dried over Mg_2SO_4, filtered, and all volatiles were removed under reduced pressure. The resulting oil was layered with pentane for 1 h to afford a solid, which was washed with pentane (2 × 20 mL) and dried in vacuo to yield a yellow waxy solid (272 mg, 99%). This solid was directly used for further synthesis without full characterisation. ^{1}H NMR (300 MHz, CD3CN) δ 8.81 – 8.71 (m, 2H), 8.20 (dd, $^3J_{HH}$ = 8.3, $^4J_{HH}$ = 1.7 Hz, 1H), 7.67 (dt, $^3J_{HH}$ = 7.7, $^4J_{HH}$ = 1.0 Hz, 1H), 7.60 (dd, $^3J_{HH}$ = 7.8, $^4J_{HH}$ = 1.2 Hz, 1H), 7.54 – 7.40 (m, 2H), 7.25 (dd, $^3J_{HH}$ = 8.2, $^4J_{HH}$ = 1.2 Hz, 1H), 7.10 – 6.88 (m, 4H), 6.45 – 6.00 (m, 2H), 3.40 (s, 3H).

Under nitrogen atmosphere and exclusion of light, the waxy solid (80 mg, 0.25 mmol), [Ru(*p*-cymene)Cl_2]$_2$ (75 mg, 0.13 mmol), $NaPF_6$ (41 mg, 0.25 mmol) and Na_2CO_3 (130 mg, 1.2 mmol) were stirred in degassed CH_3CN (5 mL) for 40 h. The crude mixture was filtered, and all volatiles were removed under reduced pressure. The residue was dissolved in CH_2Cl_2 and filtered over a short pad of basic Al_2O_3. The complex was eluted with a mixture of CH_2Cl_2 and acetone (2:1; 60 mL) as a red solution. All volatiles were evaporated under reduced pressure and the solid redissolved in a minimal amount of CH_3CN. Et_2O was then added until a red solid precipitated. The supernatant was removed and the solid washed with Et_2O (2 × 10 mL) and pentane (2 × 10 mL) to yield complex **2b** as a red solid (135 mg, 78%). ^{1}H NMR and ^{13}C NMR spectra are identical to those of **2a.** ^{19}F NMR (376 MHz, CD_3CN) δ -72.94 (d, *J* = 706.5 Hz, PF_6). HR-MS (m/z): Calculated for $[M–PF_6]^+$ = 561.1581 found 561.1579.Anal. Calc. (%) for $C_{31}H_{31}F_6N_4PRu$: C 52,77, H 4.43, N 7.94 found C 52.72, H 4.41, N 7.79.

Synthesis of complex [2a–H]$^+$

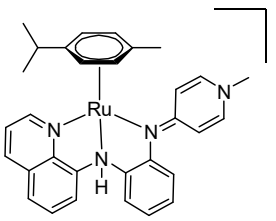

2a (297.9 mg, 0.42 µmol) was dissolved in CH_3CN (10 mL). HOTf (0.12 mL, 1.26 mmol) was added until colour changed from inital red to yellow. Aqueous saturated NH_4PF_6 solution (3 mL) and water (40 mL) were added, leading to precipitation of a yellow solid. The solid was filtered of, washed with water (40 mL) and dried under reduced pressure. The solid was dissolved in CH_2CH_2 (10 mL) and stirred for 10 min over an excess of $NaPF_6$ (400 mg). The solution was filtered and concentrated under reduced pressure. Et_2O was added (50 mL), leading to a yellow precipitate which was washed with Et_2O (2 × 20 mL). All volatiles were removed under reduced

pressure to afford **[2a-H][2PF$_6$]** as a yellow solid (215 mg, 60%). ^{1}H NMR (400 MHz, CD_3CN) δ 10.44 (s, 1H), 9.65 (dd, $^3J_{HH}$ = 5.2, $^4J_{HH}$ = 1.4 Hz, 1H, NH), 8.53 (dd, $^3J_{HH}$ = 8.5, $^4J_{HH}$ = 1.3 Hz, 1H, H_{Quin}), 8.02 (dt, $^3J_{HH}$ = 7.6, $^4J_{HH}$ = 1.0 Hz, 1H, H_{Quin}), 7.96 (dd, $^3J_{HH}$ = 8.3, $^3J_{HH}$ = 1.1 Hz, 1H, H_{Quin}), 7.88 (dd, $^3J_{HH}$ = 7.8, $^4J_{HH}$ = 1.5 Hz, 1H, H_{Ph}), 7.73 (t, $^3J_{HH}$ = 7.9 Hz, 1H, H_{Quin}), 7.66 (dd, $^3J_{HH}$ = 8.4, $^3J_{HH}$ = 5.2 Hz, 1H, H_{Quin}), 7.35 (dd, $^3J_{HH}$ = 7.9, $^4J_{HH}$ = 1.4 Hz, 3H, H_{Ph}), 7.45 – 7.22 (broad m, 2H, H_{PYE}), 7.16 (td, $^3J_{HH}$ = 7.7, $^4J_{HH}$ = 1.5 Hz, 1H, H_{Ph}), 7.09 (td, $^3J_{HH}$ = 7.6, $^3J_{HH}$ = 1.4 Hz, 1H, H_{Ph}), 6.79 (s, 2H, H_{PYE}), 6.24 (dd, $^3J_{HH}$ = 6.1, $^4J_{HH}$ = 1.3 Hz, 1H, H_{cym}), 6.10 (dd, $^3J_{HH}$ = 6.1, $^4J_{HH}$ = 1.3 Hz, 1H, H_{cym}), 6.01 (dd, $^3J_{HH}$ = 6.6, $^3J_{HH}$ = 1.0 Hz, 1H, H_{cym}), 5.86 (dd, $^3J_{HH}$ = 6.1, $^3J_{HH}$ = 1.3 Hz, 1H, H_{cym}), 3.60 (s, 3H), 2.48 (sept, $^3J_{HH}$ = 6.9 Hz, 1H, $CHMe_2$), 1.91 (s, 3H, cym–CH_3), 0.90 (d, $^3J_{HH}$ = 6.9 Hz, 3H, $(CH_3)_2CH$), 0.86 (d, $^3J_{HH}$ = 6.9 Hz, 3H, $(CH_3)_2CH$). ^{13}C NMR (101 MHz, CD_3CN) δ 162.14 (C_{Ar}), 158.84 (CH_{Quin}), 149.54, 147.51, 145.61, 142.93, 142.47 (5 × C_{Ar}), 140.89 (CH_{Quin}), 130.32, 130.13, 129.84, 129.82, 129.01, 125.02, 123.45, 122.69 , 106.96, 103.32 (10 × C_{Ar}), 86.62, 85.65, 85.17, 84.73 (4 × C_{cym}–H), 44.60 (N–CH_3), 31.37 ($CHMe_2$)), 22.20, 21.86 (2 × $CH(CH_3)_2$), 18.14. Anal. Calc. (%) for $C_{31}H_{32}F_{12}N_4P_2Ru$: C 43.72, H 3.79, N 6.58; found C 43.69, H 3.93, N 6.32.

In situ protonation with excess OTf

Complex **2a** (4 mg, 5.64 µmol) was dissolved in DMSO-d_6 and HOTf (ca. 5 µL, 56 µmol) was added. Upon addition the red solution immediately turned yellow.

^{1}H NMR (300 MHz, DMSO-d_6) δ 12.04 (s, 1H), 9.98 (d, $^3J_{HH}$ = 5.1 Hz, 1H), 8.70 (d, $^3J_{HH}$ = 8.3 Hz, 1H), 8.20 (d, $^3J_{HH}$ = 7.6 Hz, 1H), 8.06 (d, $^3J_{HH}$ = 8.1 Hz, 1H), 7.96 (dd, $^3J_{HH}$ = 7.6, $^4J_{HH}$ = 1.6 Hz, 1H), 7.84 – 7.73 (m, 2H), 7.55 (s, 2H), 7.35 (dd, $^3J_{HH}$ = 7.9, $^4J_{HH}$ = 1.6 Hz, 1H), 7.21 – 7.04 (m, 2H), 6.86 (s, 2H), 6.33 (t, $^3J_{HH}$ = 6.5 Hz, 2H), 6.15 – 6.07 (m, 2H), 3.67 (s, 3H), 2.48 – 2.38 (m, 1H), 1.88 (s, 3H), 0.85 (d, $^3J_{HH}$ = 6.9 Hz, 3H), 0.81 (d, $^3J_{HH}$ = 6.8 Hz, 3H).

Reversible deprotonation

Na_2CO_3 (ca. 8 mg, 75 µmol) was added and the suspension mixed. The color of the solution changed back from yellow to red. The ^{1}H NMR spectrum reverted to that of **2a**.

Light sensitivity of complexes 2a and 2b

In an NMR tube DMSO-d_6 solutions of **2a/2b** (4 mg in 0.6 mL) were kept in the dark and respective ^{1}H NMR spectras were recorded. The tubes were then taped to a sunfacing window and after regular time intervals ^{1}H NMR spectras were recorded to monitor the decomposition. The experiments were performed both under inert atmosphere and in air.

Crystal structure determination

Crystals of **2a** and **[2a-H]⁺** were immersed in parabar oil, mounted at ambient conditions and transferred into the stream of nitrogen (173 K). A crystal of **2a** was measured on a *RIGAKU Synergy S* area-detector diffractometer[38] using mirror optics monochromated Cu *K*α radiation (λ = 1.54184 Å), while **[2a-H]⁺** was measured on an *Oxford Diffraction SuperNova* area-detector diffractometer[38] using mirror optics monochromated Mo *K*α radiation (λ = 0.71073 Å) and Al filtered.[39] The unit cell constants and an orientation matrix for data collection were obtained from a least-squares refinement of the setting angles of reflections in the range 2.382° < θ < 77.289° for **2a** and 2.023° < θ < 27.844° for **[2a-H]⁺**. For **2a** a total of 4112 frames were collected using ω scans, with 3.2 second exposure time (10 s for high-angle reflections), a rotation angle of 0.5° per frame, a crystal-detector distance of 40.0 mm, at T = 173(2) K. For **[2a-H]⁺** a total of 834 frames were collected using ω scans, with 2.5+25 seconds exposure time, a rotation angle of 1.0° per frame, a crystal-detector distance of 65.0 mm, at T = 173(2) K.

Data reduction was performed using the *CrysAlisPro*[38] program. The intensities were corrected for Lorentz and polarization effects, and an absorption correction based on the multi-scan method using SCALE3 ABSPACK in *CrysAlisPro*[38] was applied. Data collection and refinement parameters are given in Table S2. The structures were solved by intrinsic phasing using *SHELXT*[40], which revealed the positions of all non-hydrogen atoms. All non-hydrogen atoms were refined anisotropically. H-atoms were assigned in geometrically calculated positions and refined using a riding model where each H-atom was assigned a fixed isotropic displacement parameter with a value equal to 1.2Ueq of its parent atom (1.5Ueq for methyl groups). Refinement of the structures was carried out on F^2 using full-matrix least-squares procedures, which minimized the function $\Sigma w(F_o^2 - F_c^2)^2$. The weighting schemes were based on counting statistics and included a factor to downweight the intense reflections. All calculations were performed using the *SHELXL-2014/7*[41] program in OLEX2[42]. The structure of **2a** was refined as a two-component twin, where the twin law corresponds to a rotation of -180 degrees around [-0.23 -0.00 0.97] (reciprocal) or [0.00 0.00 1.00] (direct). A disorder model was included for triflate, where the occupancy of the disorder components is refined using a free variable. The occupancies of both components together are restrained to 100%.

For **[2a-H]⁺**, a disorder model was used for one of the PF_6 units and for the CH_2Cl_2. There is another disordered CH_2Cl_2 molecule, which could not be modeled and therefore a mask was used to include the contribution of the electron density located in the void area into the calculated structure factors.

Further crystallographic details are compiled in Table S2. Crystallographic data for both structures reported in this paper have been deposited with the Cambridge Crystallographic Data Centre (CCDC) as supplementary publication numbers 2251207 (**2a**), and 2251208 (**[2a-H]⁺**).

Table 4. Crystal data and structure refinement for **2a** and **2a-H]$^+$**.

Identification code	**2a**	**[2a-H]$^+$**
Empirical formula	2251207	2251208
Formula weight	$C_{32}H_{31}F_3N_4O_3RuS$	$C_{32}H_{34}Cl_2F_{12}N_4P_2Ru$
Temperature/K	709.74	936.54
Crystal system	173.01(10)	173.00(10)
Space group	monoclinic	monoclinic
a/Å	$P2_1/c$	$P2_1/c$
b/Å	18.9076(3)	20.26618(17)
c/Å	11.49805(18)	10.02851(8)
α/°	14.5081(2)	20.44489(17)
β/°	90	90
γ/°	100.5586(15)	101.7636(9)
Volume/Å^3	90	90
Z	3100.67(9)	4067.94(6)
ρ_{calc}g/cm^3	4	4
μ/mm^{-1}	1.520	1.529
F(000)	5.220	0.679
Crystal size/mm^3	1448.0	1880.0
Radiation	0.22 × 0.154 × 0.049	0.316 × 0.216 × 0.095
2Θ range for data collection/°	Cu Kα (λ = 1.54184)	Mo Kα (λ = 0.71073)
Index ranges	4.754 to 155.63	4.07 to 54.188
Reflections collected	-23 ≤ h ≤ 23, -14 ≤ k ≤ 14, -16 ≤ l ≤ 18	-25 ≤ h ≤ 25, -12 ≤ k ≤ 12, -26 ≤ l ≤ 25
Independent reflections	12137	49828
Data/restraints/parameters	12137 [R_{int} = ?, R_{sigma} = 0.0132]	8903 [R_{int} = 0.0286, R_{sigma} = 0.0202]
Goodness-of-fit on F^2	12137/6/458	8903/12/533
Final R indexes [I>=2σ (I)]	1.203	1.036
Final R indexes [all data]	R_1 = 0.0766, wR_2 = 0.2636	R_1 = 0.0334, wR_2 = 0.0836
Largest diff. peak/hole / e Å^{-3}	R_1 = 0.0818, wR_2 = 0.2785	R_1 = 0.0397, wR_2 = 0.0874

II.5 References

1 C. Liu, F. Li, L.-P. Ma and H.-M. Cheng, *Adv. Mater.*, 2010, **22**, E28–E62.

2 S. van Renssen, *Nat. Clim. Chang.*, 2020, **10**, 799–801.

3 N. Armaroli and V. Balzani, *Energy Environ. Sci.*, 2011, **4**, 3193.

4 L. Schlapbach and A. Züttel, *Nature*, 2001, **414**, 353–358.

5 P. Preuster, C. Papp and P. Wasserscheid, *Acc. Chem. Res.*, 2017, **50**, 74–85.

6 D. Mellmann, P. Sponholz, H. Junge and M. Beller, *Chem. Soc. Rev.*, 2016, **45**, 3954–3988.

7 N. Onishi, R. Kanega, H. Kawanami and Y. Himeda, *Molecules*, 2022, **27**, 455.

8 F. Joó, *ChemSusChem*, 2008, **1**, 805–808.

9 C. Fellay, P. Dyson and G. Laurenczy, *Angew. Chem. Int. Ed.*, 2008, **47**, 3966–3968.

10 B. Loges, A. Boddien, H. Junge and M. Beller, *Angew. Chem. Int. Ed.*, 2008, **47**, 3962–3965.

11 N. Onishi, G. Laurenczy, M. Beller and Y. Himeda, *Coord. Chem. Rev.*, 2018, **373**, 317–332.

12 Y. Pan, C. Pan, Y. Zhang, H. Li, S. Min, X. Guo, B. Zheng, H. Chen, A. Anders, Z. Lai, J. Zheng and K. Huang, *Chem. Asian J.*, 2016, **11**, 1357–1360.

13 N. Lentz and M. Albrecht, *ACS Catal.*, 2022, 12627–12631.

14 A. Agapova, E. Alberico, A. Kammer, H. Junge and M. Beller, *ChemCatChem*, 2019, **11**, 1910–1914.

15 G. A. Filonenko, R. van Putten, E. N. Schulpen, E. J. M. Hensen and E. A. Pidko, *ChemCatChem*, 2014, **6**, 1526–1530.

16 K. Sordakis, C. Tang, L. K. Vogt, H. Junge, P. J. Dyson, M. Beller and G. Laurenczy, *Chem. Rev.*, 2018, **118**, 372–433.

17 R. E. Rodríguez-Lugo, M. Trincado, M. Vogt, F. Tewes, G. Santiso-Quinones and H. Grützmacher, *Nature Chem*, 2013, **5**, 342–347.

18 A. Léval, H. Junge and M. Beller, *Eur. J. Inorg. Chem.*, 2020, **2020**, 1293–1299.

19 S. Patra and S. K. Singh, *Inorg. Chem.*, 2020, **59**, 4234–4243.

20 A. Léval, A. Agapova, C. Steinlechner, E. Alberico, H. Junge and M. Beller, *Green Chem.*, 2020, **22**, 913–920.

21 H. Liu, W.-H. Wang, H. Xiong, A. Nijamudheen, M. Z. Ertem, M. Wang and L. Duan, *Inorg. Chem.*, 2021, **60**, 3410–3417.

22 H. Kawanami, M. Iguchi and Y. Himeda, *Inorg. Chem.*, 2020, **59**, 4191–4199.

23 J. J. A. Celaje, Z. Lu, E. A. Kedzie, N. J. Terrile, J. N. Lo and T. J. Williams, *Nat Commun*, 2016, **7**, 11308.

24 M. Iglesias and F. J. Fernández-Alvarez, *Catalysts*, 2021, **11**, 1288.

25 P. Hermosilla, A. Urriolabeitia, M. Iglesias, V. Polo and M. A. Casado, *Inorg. Chem. Front.*, 2022, **9**, 4538–4547.

26 Z. Wang, S.-M. Lu, J. Li, J. Wang and C. Li, *Chem. Eur. J.*, 2015, **21**, 12592–12595.

27 S. Kar, M. Rauch, G. Leitus, Y. Ben-David and D. Milstein, *Nat Catal*, 2021, **4**, 193–201.

28 E. A. Bielinski, P. O. Lagaditis, Y. Zhang, B. Q. Mercado, C. Würtele, W. H. Bernskoetter, N. Hazari and S. Schneider, *J. Am. Chem. Soc.*, 2014, **136**, 10234–10237.

29 S. Oldenhof, M. Lutz, B. de Bruin, J. Ivar van der Vlugt and J. N. H. Reek, *Chem. Sci.*, 2015, **6**, 1027–1034.

30 T. W. Myers and L. A. Berben, *Chem. Sci.*, 2014, **5**, 2771–2777.

31 N. Lentz, A. Aloisi, P. Thuéry, E. Nicolas and T. Cantat, *Organometallics*, 2021, **40**, 565–569.

32 J. Slattery, R. J. Thatcher, Q. Shi and R. E. Douthwaite, *Pure and Applied Chemistry*, 2010, **82**, 1663–1671.

33 K. Salzmann, C. Segarra and M. Albrecht, *Angew. Chem. Int. Ed.*, 2020, **59**, 8932–8936.

34 N. Lentz, Y. Streit, P. Knörr and M. Albrecht, *Chem. Eur. J.*, 2022, e202202672.

35 J. B. Curley, C. Hert, W. H. Bernskoetter, N. Hazari and B. Q. Mercado, *Inorg. Chem.*, 2022, **61**, 643–656.

36 A. Luque-Gómez, S. García-Abellán, J. Munarriz, V. Polo, V. Passarelli and M. Iglesias, *Inorg. Chem.*, 2021, **60**, 15497–15508.

37 C. M. Alder, J. D. Hayler, R. K. Henderson, A. M. Redman, L. Shukla, L. E. Shuster and H. F. Sneddon, *Green Chem.*, 2016, **18**, 3879–3890.

38 Oxford Diffraction, *CrysAlisPro, Version 1.171.40.37a. Oxford Diffraction Ltd., Yarnton, Oxfordshire, UK*, 2018.

39 P. Macchi, H.-B. Bürgi, A. S. Chimpri, J. Hauser and Z. Gál, *J Appl Crystallogr*, 2011, **44**, 763–771.

40 G. M. Sheldrick, *Acta. Crystallogr. A. Found. Adv.*, 2015, **71**, 3–8.

41 G. M. Sheldrick, *Acta. Crystallogr. C. Struct. Chem.*, 2015, **71**, 3–8.

42 O. V. Dolomanov, L. J. Bourhis, R. J. Gildea, J. A. K. Howard and H. Puschmann, *J. Appl. Crystallogr.*, 2009, **42**, 339–341.

CHAPTER III

Base-free formic acid dehydrogenation by ruthenium arene complexes

Formic acid is a promising hydrogen carrier molecule. Based on a Ruthenium(II)-arene complex featuring a tridentate PYE-amide-quinoline NNN ligand (PYE = pyridylidene amine), which is highly active in additive-free formic acid dehydrogenation, we present here a series of derivatives with modifications on the major components of the system. The ancillary cymene ligand of the parental complex was replaced with benzene and hexamethylbenzene. A strong dependence on coordination strength was found, with weaker bound benzene leading to quick deactivation under catalytic conditions and a drop in maximal turnovers by 75%. The NNN-ligand framework was modified by substituting the quinoline donor-site with a second PYE unit (PYE-amide-PYE), as well as by exchanging the aromatic backbone of the ligand for alkyl chains. The amide position in these complexes was much more basic and respective complexes were only isolated with the central nitrogen protonated. Catalytic activity of these complexes dropped by at least 80% compared to the parental system. Furthermore, the role of the centrally coordinated amide in the PYE-amide-quinoline structure was investigated by accessing protonated and methylated versions of the ruthenium complex. The centrally coordinated nitrogen was shown to be crucial for high catalytic activity, with methylation decreasing performance by three orders of magnitude. Simple electronic modifications on the aromatic ligand backbone, introducing Me, OMe and CF_3 substituents, boosted catalytic performance up to three times compared to the unsubstitued ligand. The most active complex, which was comprised of a CF_3 substituted PYE-amide-quinoline and a cymene ancillary ligand, reached turnover frequencies up to 27 000 h^{-1}, making it the most active ruthenium complex to date in the absence of additives.

P. Knörr, N. Lentz, M. Albrecht, Manuscript in preparation

III.1 Introduction

Storage of renewable energy is one of the key challenges to move towards a cyclic green energy economy and huge efforts are being devoted towards the development of alternative fuels.[1–3] Dihydrogen has been proposed as an almost ideal energy carrier which is accessible by water splitting and only yields benign products upon oxidation in a fuel cell.[4] To avoid the significant downsides of gaseous dihydrogen, such as explosivity and low volumetric energy density, the usage of liquid organic hydrogen carriers (LOHCs) as a transient storage vector is highly promising.[5] Small organic molecules can undergo reversible hydrogenation and dehydrogenation cycles allowing safe usage of stored dihydrogen. Formic acid (FA; HCOOH) is an outstanding candidate for this reaction as it can be easily handled and provides sufficiently high energy densities for broadscale application.[6–8] FA can be decomposed via two competing pathways, namely dehydrogenation (to H_2 and CO_2) and, usually undesirable, dehydration (to H_2O and CO) which necessitates development of suitable selective catalysts. While catalytic formic acid dehydrogenation (FADH) is known since the 1960s the field has only sparked more interest with the seminal work of Beller and Laurency in 2008 where they proposed FA as an LOHC.[9–11] Since then various competent systems have been developed with both Earth-abundant and precious metal complexes. Most well-performing systems however still demand additives in the form of bases or Lewis acids to reach maximal performance.[12,13] Notable exceptions are catalysts **I**, developed by Milstein, and **II** from Li and coworkers, which reach turnover frequencies (TOFs) of 3,000 h^{-1} and 487,000 h^{-1}, respectively, and turnover numbers (TONs) in the range of millions (Fig. 1).[14,15] We have recently discovered a ruthenium complex **1** containing a tridentate pyridylidene amine (PYE) ligand,[Chapter II] in which an intrinsic basic site enables TOFs as high as 10,000 h^{-1} even in the absence of additives. Here, we present the effects of systematic modifications of the ligand framework of complex **1** to identify critical factors that govern catalytic activity. Variations in the ancillary arene ligands and the main ligand scaffold were easily introduced because of the high synthetic modularity of the complex, affording improved catalytic FA dehydrogenation activity with TOFs up to 27,000 h^{-1}.

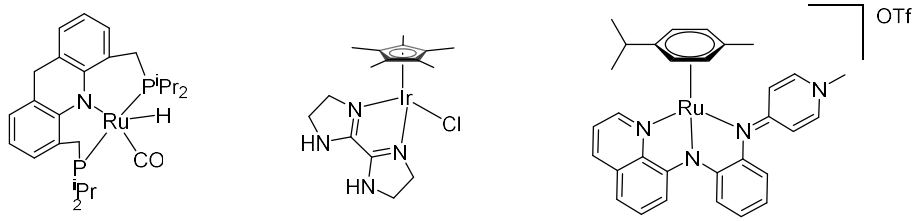

	I	**II**	**1**
	Milstein 2021	Li 2015	Chapter II
TOF [h^{-1}]	3,100	487,000	10,000
TON	1,700,000	2,400,000	1,400

Figure 1: State of the art homogeneous catalysts for FA dehydrogenation catalysis

III.2 Results and discussion

To investigate the importance of the intrinsic basic amide (N_{amid}) site for FADH, derivatives of complex **1** where synthesized, where the lone pair of the central nitrogen was not accessible. The protonated complex **2** was prepared as described in chapter II of this thesis (Fig. 2). The methylated analog **3** was easily accessed by addition of MeOTf to a solution of complex **1** in CH_2Cl_2 (Fig. 2). Passing the solution over a pad of basic Al_2O_3 followed by precipitation via addition of Et_2O yielded the pure product as a yellow solid. Successful methylation was indicated by high-resolution mass spectrometry which showed the expected *m/z* at 288.0905 (288.0908 calculated for [**3**−2OTf]$^{2+}$) and 725.1334 (725.1342 calculated for [**3**−OTf]$^{+}$). ^{1}H NMR spectroscopy showed a new resonance at δ_H = 4.02 in agreement with central nitrogen methylation. Crystals of **3** were grown by vapor diffusion of Et_2O into a CH_2Cl_2 solution of **3** and single crystal X-ray diffraction analysis unambiguously confirmed the proposed structure. We note a significant lengthening of the Ru–N_{amid} bonds by 0.12 Å (**3**) and 0.06 Å (**2**) due to switching from amide to amine coordination modes (Table 1). It was noted that methylation of the central nitrogen made the complex stable towards light irradiation which contrasts the sensitivity of **1** and **2** where ancillary arene loss occurs.[Chapter II]

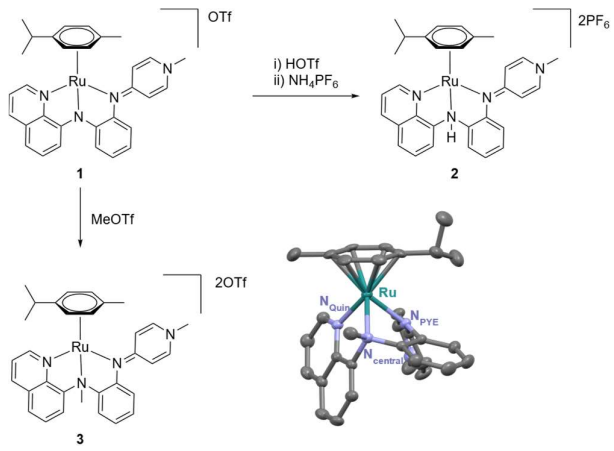

Figure 2: Synthesis of Complexes **2** and **3**, molecular structure of complex **3**; all ellipsoids at 50% probability level (hydrogen atoms and anions omitted for clarity).

Table 1: Selected bond lengths [Å] and angles [deg] of complexes **1-6**.

	1	2	3	4	5	6
Ru–N_{amid}	2.068(5)	2. 132 (3)	2.191(3)	2.068(1)	2.073(3)	2.125(2)
Ru–N_{PYE}	2.123(6)	2.112(2)	2.120(3)	2.103(1)	2.118(2)	2.126(2) 2.113(2)
Ru–N_{Quin}	2.089(6)	2.092(2)	2.081(3)	2.083(1)	2.100(3)	–
Ru– N_{amid} –C_{Quin}	114.4(5)	110.8(1)	107.8(2)	113.66(9)	115.0(2)	–
C_{Quin}– N_{amid} –C_{Ph}	115.7(6)	112.6(2)	108.2(3)	117.5(1)	116.5(3)	–
C_{Ph}– N_{amid} –Ru	108.3(5)	107.0(1)	105.0(2)	110.39(9)	108.6(2)	–

When applied in FADH, under established conditions, complex **2** reaches TOF_{inital} of 1000 h^{-1} which is only 50% of the TOF_{inital} observed with the parent complex **1** (*cf.* 2000 h^{-1}). With the methylated variant **3**, activity dropped drastically to a TOF_{inital} of 13 h^{-1}, similar to the performance level of the ruthenium precursor $[RuCl_2(p\text{-cym})]_2$ (Fig. 3). While protonation only lowers the activity of the system methylation is more impactful by three orders of magnitude, basically shutting it down completely. These findings indicate an active participation of the central nitrogen in the FADH cycle and run contrary to other groups' observations with complexes featuring similar nitrogen coordination modes. In these cases methylation of the nitrogens were highly beneficial, likely due to a difference in the dominant FADH reaction pathway.[13,16] The much lower performance of **3** compared to **2** implies that the central nitrogen position impacts FADH catalysis beyond its ability to act as an internal base in complex **1**. This might come from the higher steric demand of the methylated site, hindering formation of the active species or interfering more in the reaction mechanism, potentially also from the absence of hydrogen bonding interactions.

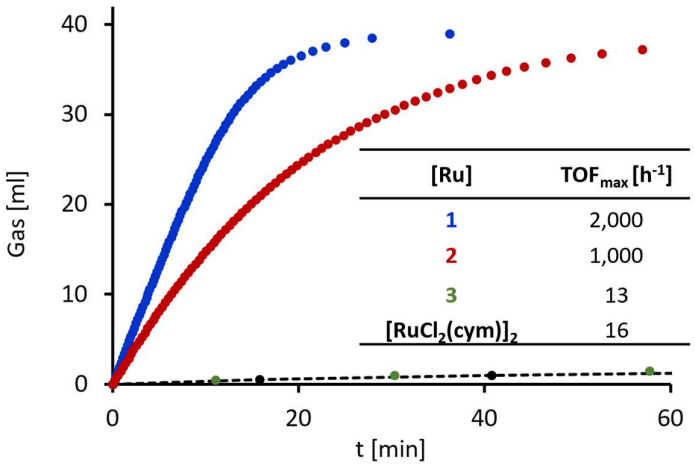

Figure 3: Time-gas evolution profiles for formic acid dehydrogenation with complexes **1**–**3** and [$RuCl_2$(*p*-cym)]$_2$. Reaction conditions: 80°C, Formic acid (40µl,), [Ru] (0.2 mol%), DMSO (1.2 mL), N_2 atm.

To probe the role of the arene moiety, analogs of complex **1** with different arenes were synthesized (Fig. 4). They were prepared via the same route as complex **1** by reacting the ligand precursor **L1** with the corresponding [$RuCl_2$(*arene*)]$_2$ in the presence of Na_2CO_3 (Fig. 4). Successful ruthenation was indicated by disappearance of the two NH protons of the ligand precursor at δ_H = 10.12 and 8.63 from ^{1}H NMR spectra. The spectras of **4** and **5** are comparable to those of **1** apart from the absence of p-cym resonances and the appearance of signals corresponding to CH_{Benz} for **4** at δ_H = 5.66 and $CH_{3\ Hexamethlbenzene}$ for **5** at δ_H = 1.88. High-resolution mass spectrometry showed the expected *m/z* at 505.0953 (505.0961 calculated for [**4**−OTf]$^+$) and 589.1894 (589.1900 calculated for [**5**−OTf]$^+$). Crystals grown by vapor diffusion of Et_2O into CH_2Cl_2 were analyzed by single crystal XRD analysis which confirmed the proposed structures. The Ru–N bond lengths of both **4** and **5** do not majorly differ from **1** (*cf* Table 1). It was noted that the arene changes had major impacts on the stability of the complexes, which turn darker upon degradation in solution. When exposed to sunlight, solutions of complex **4** featuring a benzene ligand visibly decomposed after several seconds, much faster than cymene containing complex **1** which visually darkens within ca. 30 s. Trace amounts of decomposition products, in the form of free benzene (δ_H = 7.37 in ^{1}H NMR spectras), were always apparent in solution even when handled under minimal light. With complex **5** comprised of a hexamethylbenzene ligand, visible decomposition took around two minutes. This is indicative for a stronger bonding of more electron rich arenes to ruthenium.[17]

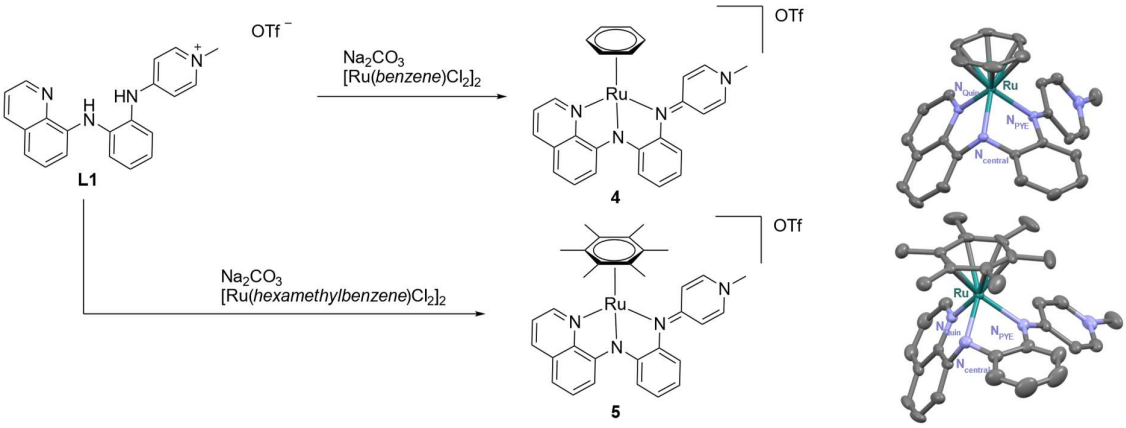

Figure 4: Synthesis of complexes **4** and **5**, and their molecular X-ray structures (ellipsoids at 50% probability level, hydrogen atoms, anions and co-crystallized solvent molecules omitted for clarity).

Applying complexes **4** and **5** in FADH catalysis showed notable differences to complex **1** (Fig. 5). **4** rapidly deactivated after a burst of initial activity where it showed equivalent activity to **1**, with a significant TOF decrease after a few seconds. The hexamethylbenzene complex **5** does not show this rapid deactivation in FADH. However this complex was overall less active than **1** (TOF_{inital}(**1**) = 2000 h^{-1}; TOF_{inital}(**5**) = 1300 h^{-1}). Rapid deactivation of complex **4** suggests arene decoordination as a major catalyst deactivation pathway, in agreement with previous experimental observations with complex **1,** where free cymene was detected by ^{1}H NMR spectroscopy when following FADH catalysis.[Chapter II] Benzene is usually weaker coordinated to ruthenium and dissociates easier than arenes with more donating substituents.[17] This is supported by results obtained from the presumably stronger coordinated hexamethylbenzene which did not rapidly deactivate. In terms of TOF_{max} the hexamethylbenzene ligand was however still outperformed by the cymene. The negative effect of the hexamethylbenzene could arise from several parameters. The imposed sterics might have a detrimental effect on the reaction rate by limiting access of the reactant during a key step of the reaction mechanism. In addition to these steric effects potentially disfavoured η4 slippage during a transition state might also play a role.

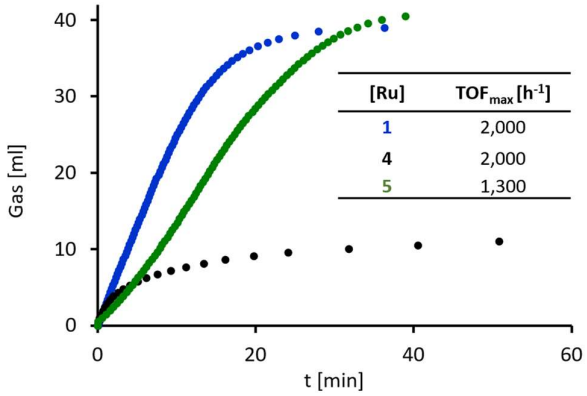

Figure 5: Time-gas evolution profiles for formic acid dehydrogenation with **1**,**4** and **5**. Reaction conditions: 80 °C, Formic acid (40µl, 1.06 mmol), [Ru] (0.2 mol%), DMSO (1.2 mL), N_2 atm.

The influence of the NNN-tridentate chelating ligand framework was evaluated with two analogous complexes **6** and **7,** which feature instead of the aminoquinoline donor site an additional PYE mojety (Fig. 6). The **AIkyl-bisPYE** ligand precursor was synthesized by reaction of diethylenetriamine with 4-chloropyridinium triflate followed by anion metathesis with aqueous KPF_6. Coordination to ruthenium was accomplished by reaction of **AIkyl-bisPYE** with Ru[(p-cym)Cl_2]$_2$ in the presence of Na_2CO_3 as a base. Complex formation was indicated by high resolution mass spectrascopy with an *m/z* of 666.1743 (666.1734 calculated for [**6**−PF_6]$^+$). ^{1}H NMR spectroscopy showed the diagnostic disappearance of the ligand precursors NH_{PYE} resonances at δ_H = 8.45 and appearance of a broad signal at δ_H = 7.28 indicative for the protonated central nitrogen of the ruthenium complex. The proposed connectivity is in line with the other members of the series and was unambiguously confirmed by X-ray diffraction analysis of a single crystal grown by slow diffusion of Et_2O into a CH_2Cl_2 solution of **6**. Complex **6** could not be isolated with the central nitrogen deprotonated. Even when Na_2CO_3 was replaced in the synthesis with strong bases, such as NaOtBu or BuLi the complex got protonated during purification attempts and no clean product was isolated. Deprotonation of **6** and isolation of the resulting complex was equally unsuccessful. The alkyl linkers are strongly donating which may render the central nitrogen increasingly basic. The **Ph-bisPYE** ligand precursor was synthesized according to a previously published procedure.[18] Successful ruthenation was indicated by high resolution mass spectrometry with an *m/z* of 762.1731 (762.1734 calculated for [**7**− PF_6]$^+$). The protonated central nitrogen was observed in ^{1}H NMR spectroscopy with a resonance at δ_H = 6.32. The pure complex is highly air sensitive and decomposes within hours of continuous exposure. Similar to **6,** complex **7** was also only isolated in the protonated form. This indicates that replacement of strongly donating alkyl linkers with electron poorer arenes is not sufficient to lower the basicity of the central nitrogen enough to allow isolation of the

deprotonated complex, but that the presence of the aminoquinoline sidearm is essential to the lower basicity of N_{amid} in complex **1**.

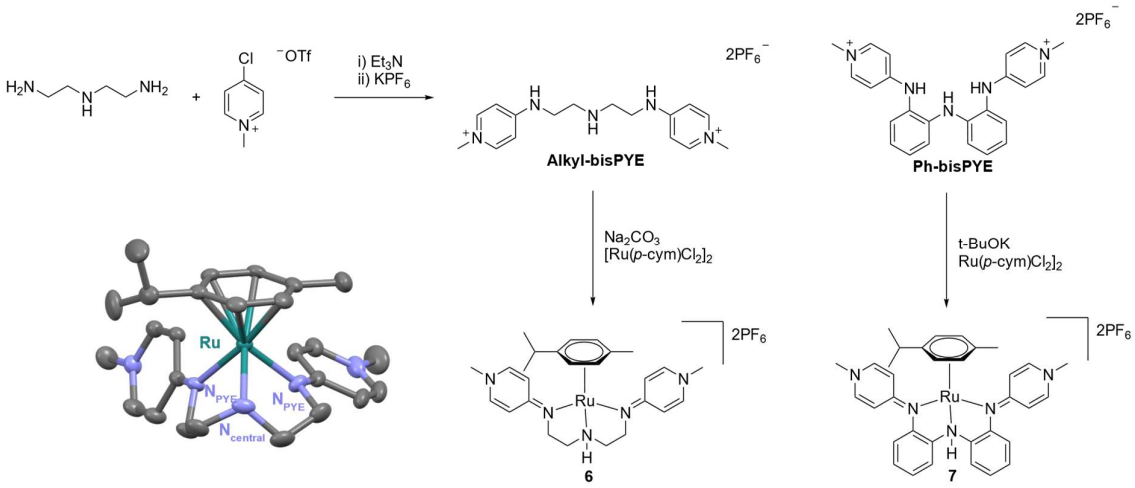

Figure 6: Synthesis of complexes **6** and **7** and their molecular X-ray structures (all ellipsoids at 50% probability level; hydrogen atoms, anions and co-crystallized solvent molecules omitted for clarity).

In FADH both **6** and **7** exhibited decreased catalytic activity with much lower TOFs (**6** = 40 h^{-1}; **7** = 400 h^{-1}) compared to complex **1** (2000 h^{-1}; Fig.6). The diminished performance is most likely strongly correlated to the absence of a basic site on the complexes and thereby absent or diminished ligand cooperativity. In protonated complex **2** activity was decreased to a lesser extent which we tentatively attribute to increased acidity of the NH mojety. The higher acidity is evident through the easy deprotonation **2** with weak bases[Chapter II] (e.g. Na_2CO_3) which are insufficient to deprotonate **6** or **7**. The core design of the initially investigated complex **1,** consisting of cymene ancillary ligand and the dissymmetric PYE aminoquinoline, is thus the most proficient combination with modifications targeting main features of the complex being detrimental.

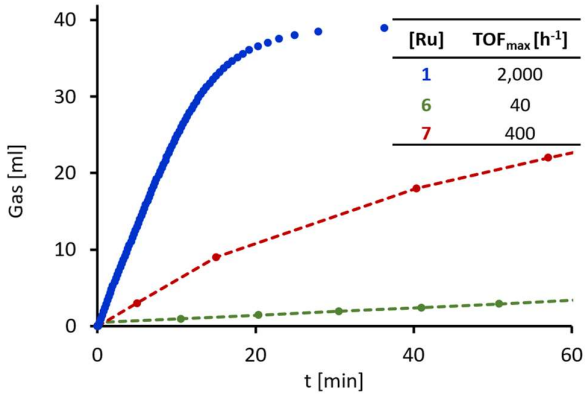

Figure 7: Time-gas evolution profiles for formic acid dehydrogenation with **1**,**6** and **7**. Reaction conditions: 80 °C, formic acid (40 µl, 1.06 mmol), [Ru] (0.2 mol%), DMSO (1.2 mL), N_2 atm. Catalytic runs of **7** were measured with an inverted burette setup.

Electronic modifications of the NNN ligand where thus undertaken (Fig. 8), aimed at changing the basicity of the central nitrogen, which was presumed as a key parameter for high TOFs. Installing electron withdrawing or donating groups in para position to the central nitrogen on the phenyl ring were suggested to allow finetuning of the pK_A of the conjugated acid complex. Ligand precursors **8a** and **b** were prepared through an Ullman coupling between the respective iodonitroarenes and 8-aminoquinoline. **8c** was synthesized similar to the unsubstitued ligand precursor **L1** by electrophilic aromatic substitution on the electron poor -CF_3 substituted nitrofluoroarene with 8-aminoquinoline. The nitro groups of all intermediates were reduced via Pd/C to the corresponding amines, which were heated with 4-chloroaminopyridine under neat conditions to yield the NNN-Ligand precursors **8a-c** as triflate salts. The complexes were obtained analogous to **1** by reacting the ligand precursors with [Ru(*p*-cym)Cl_2]$_2$ in the presence of Na_2CO_3. Complex formation was indicated in ^{1}H NMR spectroscopy by the disappearance of the two NH proton resonances corresponding to the ligand precursors at δ_H = 10.7 and 8.32 for **9c**, δ_H = 9.57 and 8.95 – 8.84 for **9b** and δ_H = 9.88 and 8.75 for **9a**. The overall similarity of the spectra with complex **1** strongly indicates that the general structures and coordination modes are convergent. High-resolution mass spectrometry showed the expected *m/z* signals at at 629.1485 (629.1461 calculated for [**9c**−OTf]$^+$), 591.1714 (591.1692 calculated for [**9b**−OTf]$^+$) and 575.1763 (575.1743 calculated for [**9a**−OTf]$^+$). X-Ray diffraction analysis of single crystals of **9a-c,** grown by Et_2O/ CH_2Cl_2 vapour diffusion, unambiguously confirmed coordination modes analogous to complex **1**. None of the introduced functional groups had pronounced impact on the solid state e.g. bond distances between the ligand and ruthenium are all in the range of complex **1** (Ru–N_{amid} 2.07 Å, Ru–N_{PYE} 2.12 Å, Ru–N_{Quin} 2.09 Å; Table 2.). We note that complex **8b** tended to reprotonate in the syntesis if during precipitations wet

solvents were used. This indcates a slightly higher basicity of the methyl substituted complex **8b** over the other complexes of this series.

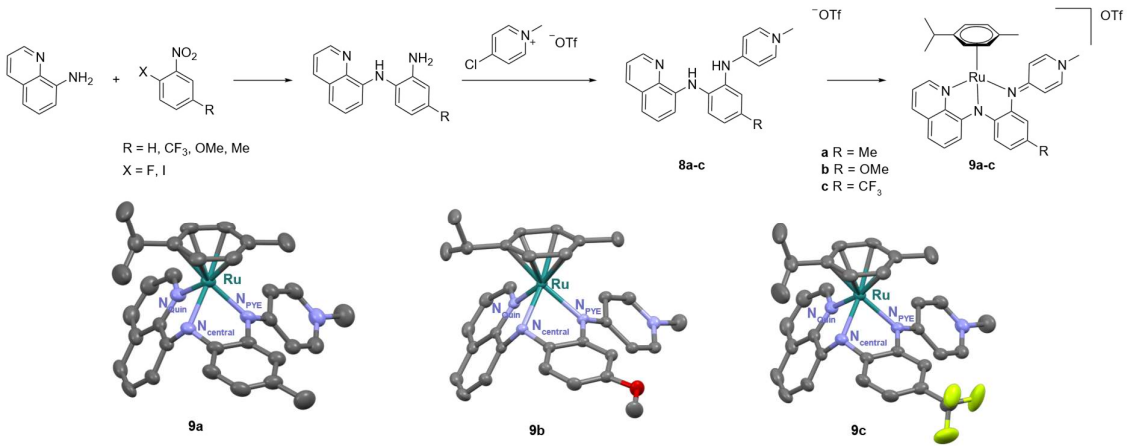

Figure 8: Synthesis of ligand precursors **8a-c** and complexes **9a-c**; molecular X-ray structures of complexes **9a-c**; all ellipsoids at 50% probability level (hydrogen atoms, anions and co-crystallized solvent molecules omitted for clarity).

Table 2: Selected bond lengths [Å] and angles [deg] of complexes **9a-c**.

	9a	**9b**	**9c**
Ru–N_{amid}	2.073(4)	2.074(1)	2.071(2)
Ru–N_{PYE}	2.118(5)	2.117(1)	2.121(2)
Ru–N_{Quin}	2.096(5)	2.087(1)	2.094(2)
Ru– N_{amid} –C_{Quin}	114.5(3)	114.6(1)	115.3(2)
C_{Quin}– N_{amid} –C_{Ph}	118.7(4)	117.5(1)	118.5(2)
C_{Ph}– N_{amid} –Ru	108.3(3)	109.0(1)	109.6(2)

To determine if the modifications had the expected influence on the basicity of the central nitrogen the pK_A of the complexes was determined in DMSO by ^1H NMR spectroscopy (Table 3).[19,20] To solutions of complexes **1** and **9a-c** known amounts of a weak acid ($HNEt_3Cl$, pK_A^{DMSO} = 9.00) were added. Based on the equilibria that established between protonated complex $[Ru(NN\text{-}HN)]^+$, deprotonated complex [Ru(NNN)], weak acid $HNEt_3Cl$ and corresponding base NEt_3 the pK_A^{DMSO} of the protonated complexes $[RuN\text{-}H]^+$ were determined. The pK_A^{DMSO} of the conjugated acid of complex **1** was determined at 8.57. The methyl substitution leads to the most basic complex with a pK_A of 9.22 whereas the OMe substituent barely influenced the measured pK_A (8.62). The CF_3 group slightly lowered the pK_A to 8.41 but not as much as expected, as based on σ_p the CF_3 group should have the most pronounced impact, yet the pK_A

deviation from **1** is smaller (ΔpK_A = 0.16) than that of the methyl substituted complex (ΔpK_A = 0.65). The substituents apparently influence the basicity but not to the extent expected when solely looking at *para*-Hammet parameters.

Table 3. pK_A of the amine nitrogen in complexes **1** and **9**, literature Hammet parameters[21] and TOFmax of complexes **1** and **9**

[Ru]	R	pK_A^{DMSO}	σ_p	σ_m	TOF_{max} [h^{-1}]
1	H	8.57	0	0	2,000
9a	Me	9.22	-0.17	-0.07	2,000
9b	OMe	8.62	-0.27	0.12	2,200
9c	CF_3	8.41	0.54	0.43	4,000

When applied in FADH catalysis (Fig. 9), **9a** with the electron donating methyl group performed almost identical to the unsubstituted complex **1** with TOF_{max} of 2,000 h^{-1}. The -OMe substitution of **9b** lead to a slightly increased TOF_{max} of 2,200 h^{-1} while the -CF3 substitution of **9c** showed twice the activity of **1**, reaching TOF_{max} of 4,000 h^{-1}. Overalll the complexes showed modulated activites compared to the unsubstituted complex but their performance did not follow a clear trend. Based solely on the pK_A, **9a** should show distinctly different activity to **1** as its pK_A deviates the most, yet experimental results show no significant modulation of activity. Hence electronic effects on N_{amid}, as measured by pK_A, do not correlate with activity of the substituted complexes. The positive effect of both CF_3 and OMe substituents may be explained by their electron-withdrawing nature in meta position, thus influencing the electron density on the PYE nitrogen. We suggest that the substituent effects arrise from their combined impact on ligand electronics rather than from a localized effect on the pKa of the central nitrogen.

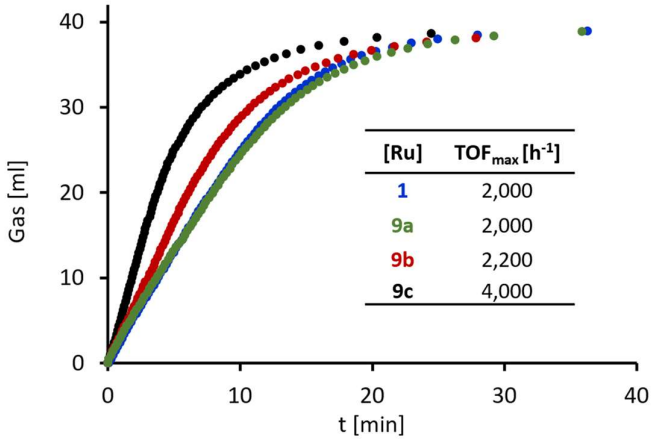

Figure 9: Time-gas evolution profiles for formic acid dehydrogenation with **1** and **9**. Reaction conditions: 80 °C, formic acid (40µl,), [Ru] (0.2 mol%), DMSO (1.2 mL), N_2 atm. Representative single runs are shown but catalytic runs were performed at least twice to ensure reproducibility.

With complex **9c** significantly outperforming other modifications FADH reaction conditions were further optimized to assess maximal performance. Different reaction temperatures were screened (70-100 °C) and raising temperatures increased overall TOFs, up to 15,000 h^{-1} at 100 °C. Catalytic loading was then lowered to 0.02 and 0.002 mol% which resulted in TOF_{max} of 27,000 and 20,000 h^{-1}, respectively. Thus lowering catalyst loading beyond 0.02 mol% decreases catalytic activity. Different FA concentrations were assessed in the range of 0.88 to 4.4 M (Figure 10). TOF_{max} remained constant in the range of 0.88-2.2 M (27,000 h^{-1}) and started to drop off at higher concentrations of 4.4 and 8.8 M. TON_{max} changed from 1,600 (0.88 M) to 2,100 (2.2 M), 2,400 (4.4 M) and 830 (8.8 M). Optimal performace in regard to TONs is reached at around 4.4 M solutions of FA, whereas higher concenctrations were detrimental for the catalyst. To the best of our knowledge **9c** is the most active ruthenium complex in additive free formic acid dehydrogenation described so far (*cf*. state of the art TOF: 3,100 by Milstein[14]), although with TONs well below minimal requirements for practical application.

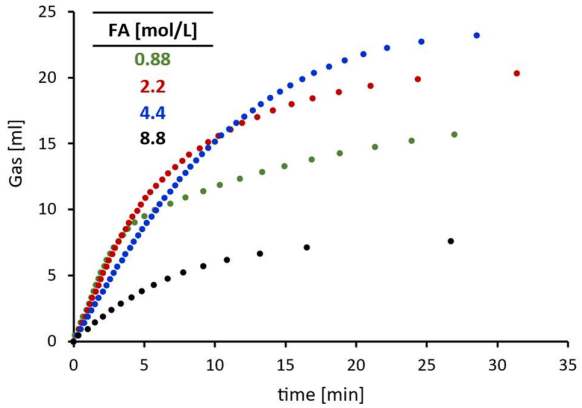

Figure 10: Influence of different FA concentrations on catalytic profile. Single runs are shown but all reactions were carried out at least twice to ensure reproducibility. Reaction carried out according to general procedure. Conditions: 80 °C, DMSO (1.2 mL), **9c** (1.06 µmol, 0.18 mmol/l), FA (40 µL; 100 µL; 0.2 mL; 0.4 mL).

Based on the temperature dependence experiments (Fig. 11) Arrhenius and Eyring analyses were carried out (Fig. 12), revealing an activation energy E_a = 80.2 ± 1 kJ mol^{-1}, an enthalpy of activation $\Delta H^{\ddagger}$ = 77.2 ± 1 kJ mol^{-1} and an entropy of activation $\Delta S^{\ddagger}$ = –80.7 ± 3 J (K mol)$^{-1}$ for catalyst **9c**. Thus E_a is ca. 10 kJ mol^{-1} higher than with complex **1**, $\Delta H^{\ddagger}$ is ca. 12 kJ mol^{-1} higher and $\Delta S^{\ddagger}$ increased by ca. 80 J (K mol)$^{-1}$ (*cf.* **1**: E_a = 68 ±1 kJ mol^{-1}; $\Delta H^{\ddagger}$ = 65 ±1 kJ mol^{-1}; $\Delta S^{\ddagger}$ = –177 ±3 J (K mol)$^{-1}$).[Chapter II] The calculated Gibbs free energy at 100 °C with **9c** is ΔG = 107.3 kJ mol^{-1} compared to ΔG = 131.0 kJ mol^{-1} of compound **1** which requires 23.7 kJ mol^{-1} more energy input. This is congruent with the overall higher FADH activity observed with compound **9c**.

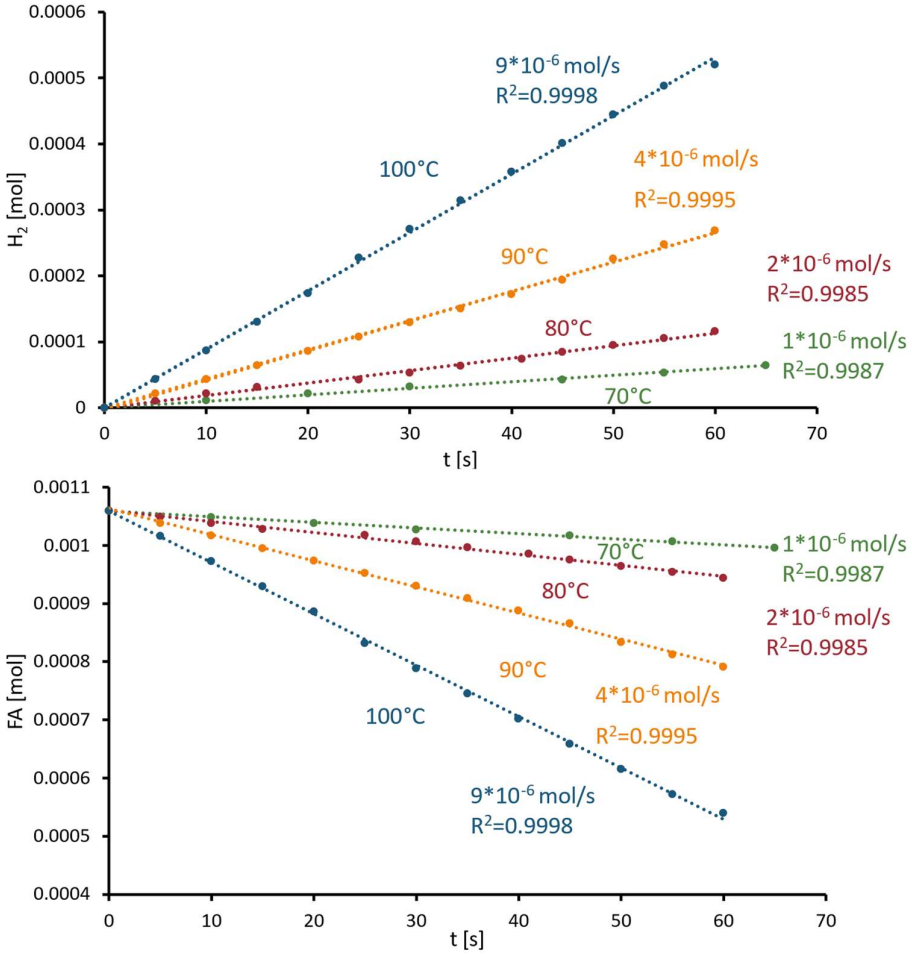

Figure 11: Initial production of H_2 (top) and initial FA consumption (bottom) at different temperatures. H_2 production was calculated based on 50% of the evolved gas volume consisting of the CO_2:H_2 mixture. The FA concentrations were calculated based on initially injected amount minus consumed amount based on evolved gas volume. Reaction condition: **9c** (0.01 mol%), FA (1.06 mmol) and DMSO (1.2 mL) at indicated temperature.

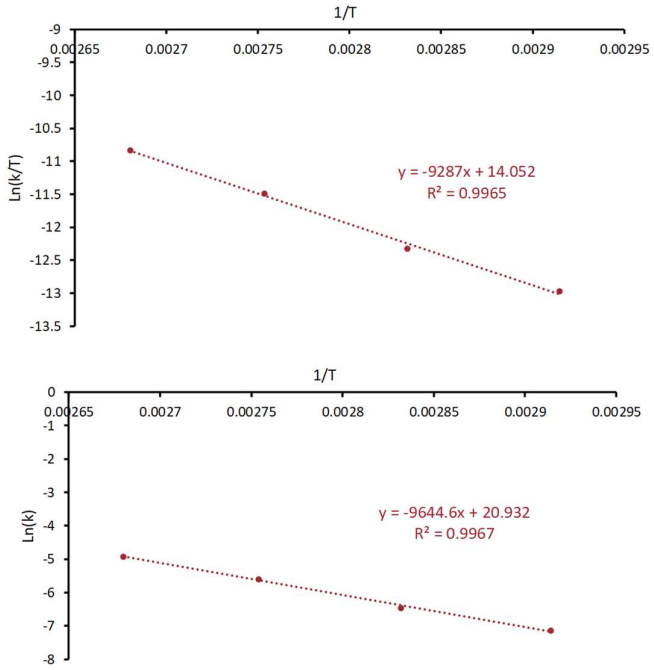

Figure 12: Arrhenius plot (top) and Eyring plot (bottom), form rates deduced from temperature dependent catalysis (see slopes in Fig. 11)

Gas analysis by GC of a representative catalytic run with **9c** did not show any formation of undesired CO, only H_2 and CO_2 were detected.

III.3 Conclusion

By modulating the parent Ru(II)-NNN system and accessing a series of derived complexes the role of individual components was elucidated in FADH catalysis. Our investigation showed that the central nitrogen plays an essential role for high catalytic activity and that methylation of this position, which changes the coordination mode to an amine, is detrimental to catalytic activity. Simple electronic modifications on the NNN framework, by introducing different substituents on the connecting phenyl mojety, resulted in the most active ruthenium complex for additive-free formic acid dehydrogenation to date. The complex features the tridentate PYE-amide-quinoline ligand, functionalized with an electron-withdrawing CF_3 substituent, in combination with an ancillary *p*-cymene and showed TOFs of 27,000 h^{-1}. While the high TOFs of the system are highly promising the productivity is still low due to deactivation, attributed to loss off the ancillary arenes during catalysis. These shortcomings may be remedied by further exploring ancillary

ligands, and potentially linking the arene mojety to the structural backbone of the main ligand, to prevent easy decoordination.

II.4 Experimental section

General considerations

Ruthenium complexes were synthesized under exclusion of light. Ligand precursor **L1**, **Aryl-bis-PYE** and complexes **1** and **2** were synthesized according to previously published procedures.[18, Chapter II] All other reagents were commercially available and used as received unless specified. NMR spectra were recorded at 25 °C on Bruker spectrometers operating at 300 or 400 MHz (^{1}H NMR), 282 or 376MHz (^{19}F NMR), and 75 or 100 MHz (^{13}C{^{1}H} NMR), respectively. Chemical shifts (δ in ppm, coupling constants *J* in Hz) were referenced to residual solvent signals (^{1}H,^{13}C). Assignments are based on homo- and hetero nuclear shift correlation spectroscopy. Column chromatography of 8 was performed on a Biotage Isolera system. High resolution mass spectrometry was carried out by the DCBP mass spectrometry group at the University of Bern with a Thermo Scientific LTQ Orbitrap XL (ESI-TOF). Elemental analyses were performed on a Thermo Scientific Flash 2000 CHNS-O elemental analyzer by the DCBP Microanalytic Laboratory.

Complex 3

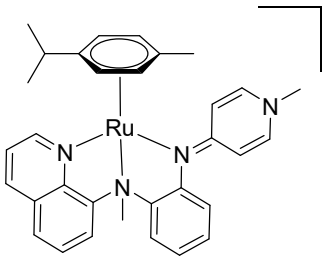

2OTf

Under nitrogen atmosphere and under exclusion of light precursor complex **1** (50 mg, 70 µmol) was dissolved dry CH_2Cl_2 (5 mL), MeOTf (24 µL, 0.21 mmol) was added and the solution was stirred for 15 min. An excess of MeOH (0.3 mL, 74 mmol) was injected and the solution stirred for 3 h. All volatiles were removed under reduced pressure, yielding a green sticky oil, which was dissolved in CH_3CN (10 mL) and filtered over basic Al_2O_3. All volatiles were removed in vacuo. The residue was dissolved in a minimal amount of CH_2Cl_2 (1 mL), filtered over Celite and precipitated from the solution by addition of Et_2O (10 mL). The resulting solid was washed with Et_2O (2 × 10 mL) yielding the pure complex **3** as a yellow powder (50 mg, 81%). Vapor diffusion of Et_2O into a solution of complex **3** in CH_2Cl_2 gave crystals suitable for X-ray diffraction analysis. ^{1}H NMR (400 MHz, CD_3CN) δ 9.83 (dd, $^{3}J_{HH}$ = 5.3, $^{4}J_{HH}$ = 1.3 Hz, 1H, H_{Quin}), 8.51 (dd, $^{3}J_{HH}$ = 8.4, $^{4}J_{HH}$ = 1.3 Hz, 1H, H_{Quin}), 8.04–7.97 (m, 1H, H_{Ph}), 7.89 (dd, $^{3}J_{HH}$ = 8.0, $^{4}J_{HH}$ = 1.3 Hz, 1H, H_{Quin}), 7.75–7.60 (m, 3H, 3 H_{Quin}), 7.31–7.09 (m, 5H, 3 H_{Ph}, 2 $H_{PYE\ \alpha}$), 6.44 (d, $^{3}J_{HH}$ = 7.2 Hz, 2H, $H_{PYE\ \beta}$), 6.09–6.05, 6.03–5.99, 5.96–5.92, 5.92–5.89 (4 × m, 1H, H_{cym}), 4.02 (s, 3H, Ru–NCH_3), 3.53 (s, 3H, pyr–CH_3), 2.62 (septet, $^{3}J_{HH}$ = 6.9 Hz, 1H, $CHMe_2$), 2.04 (s, 3H, cym–CH_3), 1.08, 0.89 (2 × d, $^{3}J_{HH}$ = 6.9 Hz, 3H, (CH_3)$_2$CH). ^{13}C{^{1}H} NMR (101 MHz, CD_3CN) δ 162.32, 159.36 (CH_{Quin1}), 152.63, 149.58, 149.43, 144.54 (C_{Quin9}), 142.29 ($CH_{PYE\ \alpha}$), 141.09 (CH_{Quin3}), 130.22, 130.05 ($CH_{Quin2,6,7}$), 129.89 (CH_{Quin5}), 128.71 (CH_{Ph}), 128.46 ($CH_{Quin2,6,7}$), 124.96 (CH_{Ph}), 124.92 ($CH_{Quin2,6,7}$), 123.84 (C_{OTf}), 122.84 (CH_{Ph}), 120.65 (C_{Ph}), 119.19 (CH_{Ph}), 108.88, 102.87 (C_{cym}–*i*Pr, C_{cym}–Me), 87.35, 86.34, 86.25, 86.00 (4 × CH_{cym}), 58.18 (Ru–NCH_3), 44.59 (pyr–CH_3), 31.10 ($CHMe_2$), 22.11, 21.95 (2 × CH(CH_3)$_2$), 18.11 (cym–CH_3). HR-MS

(m/z): Calculated for $[M–OTf]^+$ = 725.1342 found 725.1334. Anal. Calc. (%) for $C_{34}H_{34}F_6N_4O_6RuS_2$: C 46.73, H 3.92, N 6.41; found C 46.47, H 3.76, N 6.22.

Complex 4

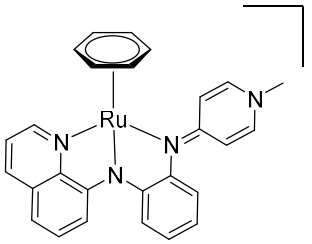

Under nitrogen atmosphere and exclusion of light, $[RuCl_2(benzene)]_2$ (105.0 mg, 0.210 mmol), Ligand precursor **L1** (200 mg, 0.420 mmol) and Na_2CO_3 (444.9 mg, 4.20 mmol) were stirred in degassed CH_3CN (5 mL) for 40 h. The crude mixture was filtered over a paper filter. All volatiles were removed. The crude was dissolved in CH_2Cl_2 and loaded onto a short pad of basic Al_2O_3. The complex was then eluted with a mixture of CH_2Cl_2 and acetone (2:1; 60 mL). All volatiles were evaporated under reduced pressure and the solid redissolved in a minimal amount of CH_2Cl_2. Pentane was then added until a red solid precipitated. The supernatant was removed and the solid washed with and pentane (3 × 30 mL) to yield **4** as a red solid (235 mg, 86%). ^{1}H NMR (400 MHz, CD_3CN) δ 9.51 (dd, $^3J_{HH}$ = 5.0, $^4J_{HH}$ = 1.3 Hz, 1H, H_{Quin}), 8.15 (dd, $^3J_{HH}$ = 8.5, $^4J_{HH}$ = 1.3 Hz, 1H, H_{Quin}), 7.49 (dd, $^3J_{HH}$ = 7.6, $^4J_{HH}$ = 1.5 Hz, 1H, H_{Ar}), 7.37 (dd, $^3J_{HH}$ = 8.4, $^3J_{HH}$ = 5.1 Hz, 1H, H_{Quin}), 7.33 – 7.23 (m, 2H, $H_{PYE\ \alpha}$, H_{Ar}), 7.22 – 7.14 (m, 2H, H_{Ar}), 7.08 (dd, $^3J_{HH}$ = 7.6, $^4J_{HH}$ = 3.1 Hz, 1H, H_{Ar}), 7.01 – 6.92 (m, 3H, H_{Ar}, $H_{PYE\ \alpha}$), 6.85 (td, $^3J_{HH}$ = 7.7, $^4J_{HH}$ 1.5 Hz, 1H, H_{Ar}), 6.79 (dd, $^3J_{HH}$ = 7.7, $^4J_{HH}$ 3.1 Hz, 1H, H_{Ar}), 5.66 (s, 6H, H_{Benz}), 3.49 (s, 3H, pyr–C*H*$_3$). ^{13}C{^{1}H} NMR (101 MHz, CD_3CN) δ 161.04, 160.39, 159.84, 155.34 (4 × CH_{Ar}), 155.12 (CH_{Ar}), 148.15 (C_{Ar}), 141.56, 140.81 (2 × CH_{Ar}), 138.36, 131.10 (2 × C_{Ar}), 129.89 (2 overlapping peaks, 2 × CH_{Ar}), 125.29, 124.43, 123.18, 123.03, 119.47, 119.38, 116.75, 114.81(8 × CH_{Ar}), 109.55 (overlapping peak, 2 × C_{Ar}), 87.64 (C_{Benz}), 43.87 (N–*C*H$_3$). HR-MS (m/z): Calculated for $[M–OTf]^+$ = 505.0961 found 505.0953. Anal. Calc. (%) for [Chemical Formula: $C_{28}H_{23}F_3N_4O_3RuS$]: C 51.45, H 3.55, N 8.57 found C 50.70, H 3.53, N 8.43.

Complex 5

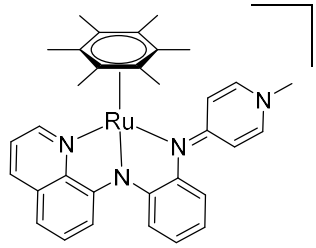

Under nitrogen atmosphere and under exclusion of light, $[Ru(hexamethylbenzene)Cl_2]_2$ (140.3 mg, 0.420 mmol), Ligand precursor **L1** (200 mg, 0.420 mmol) and Na_2CO_3 (309.7 mg, 4.20 mmol) were stirred in degassed CH_3CN (5 mL) for 40 h. The crude mixture was filtered over a paper filter. All volatiles were removed. The crude was dissolved in CH_2Cl_2 and loaded onto a short pad of basic Al_2O_3. The complex was then eluted with a mixture of CH_2Cl_2 and acetone (2:1; 60 mL). All volatiles were evaporated under reduced pressure and the solid redissolved in a minimal amount of CH_2Cl_2. Et_2O was then added until a red solid precipitated. The supernatant was removed and the solid washed with Et_2O (2 × 30 mL) and pentane (2 × 30 mL) to yield **5** as a red solid (265 mg, 86%). ^{1}H NMR (400 MHz, CD_3CN) δ 9.03 (dd, $^3J_{HH}$ = 5.0, $^4J_{HH}$ = 1.4 Hz, 1H, H_{Quin}), 8.07 (dd, $^3J_{HH}$ = 8.4, $^4J_{HH}$ = 1.3 Hz, 1H, H_{Quin}), 7.52 (dd, $^3J_{HH}$ = 7.6, $^4J_{HH}$ = 1.4 Hz, 1H, H_{Ar}), 7.39 (dd, $^3J_{HH}$ = 8.4, $^3J_{HH}$ = 5.1 Hz, 1H, H_{Quin}), 7.28 (dd, $^3J_{HH}$ = 7.6, $^4J_{HH}$ = 2.1 Hz, 1H, H_{Ar}), 7.25 (t, $^3J_{HH}$ = 7.8 Hz, 1H, H_{Ar}), 7.22 – 7.14 (m, 2H, H_{Ar}), 6.99 – 6.88 (m, 3H, H_{Ar}), 6.82 (td, $^3J_{HH}$ = 7.6, $^4J_{HH}$ = 1.4 Hz, 1H, H_{Ar}), 6.77 (dd, $^3J_{HH}$ = 7.8, $^4J_{HH}$ = 3.0 Hz, 1H, H_{Ar}), 6.60 (dd, $^3J_{HH}$ = 7.5, $^4J_{HH}$ 3.0 Hz, 1H, H_{Ar}), 3.46 (s, 3H, pyr–C*H*$_3$), 1.88 (s, 18H, $CH_{3\ Benz}$). ^{13}C{^{1}H} NMR (101 MHz, CD_3CN) δ 160.58, 158.76, 157.81 (3 × C_{Ar}), 153.23 (CH_{Quin}), 149.04 (C_{Ar}), 141.45, 140.71, 137.76 (3 × CH_{Ar}), 131.26 (C_{Ar}), 129.93 (CH_{Ar}), 127.20

(CH_{Quin}), 124.13 (CH_{Ar}), 123.01 (CH_{Quin}), 122.07, 121.37 (2 × CH_{Ar}), 118.31 (peak overlapping with solvent, CH_{Ar}), 115.81, 114.55, 109.34 (3 × CH_{Ar}), 96.37 (C_{Benz}), 43.77 (N–CH_3), 15.50 ($CH_{3\ Benz}$). HR-MS (m/z): Calculated for $[M–OTf]^+$ = 589.1900 found 589.1894. Anal. Calc. (%) for [Chemical Formula: $C_{34}H_{35}F_3N_4O_3RuS$]: C 55.35, H 4.78, N 7.59 found C 55.05, H 4.61, N 7.29.

Alkyl-bis-PYE ligand precursor

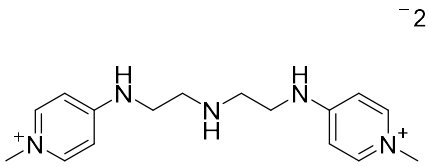

Diethylenetriamine (0.1 mL, 0.93 mmol) was dissolved in dry CH_3CN (10 mL) with Et_3N (10 mL) and placed in an ice bath. A solution of 4-chloro-1-methylpyridinium triflate (0.513 mg, 1.85 mmol) in CH_3CN (10 mL) was added dropwise under stirring to the solution. The mixture was stirred for 16 hours while letting the solution slowly reach room temperature. All volatiles were removed under reduced pressure and the solid washed with $CHCl_3$ (3 × 20 mL). The solid was dissolved in a minimal amount of water and KPF_6 (1.66 g, 9.25 mmol) was added. A white precipitate was formed upon addition and the solid was collected as the pure ligand (392 mg, 0.68 mmol, 73% yield). ^{1}H NMR (DMSO-d_6, 400 MHz): δ 8.45 (s, 2H, PYE-N*H*-CH_2), 8.19 (dd, J = 7.3, 1.5 Hz, 2H, C$H_{PYE\ \alpha}$), 8.02 (dd, J = 7.3, 1.7 Hz, 2H, C$H_{PYE\ \alpha}$), 6.91 (dd, J = 7.3, 2.9 Hz, 2H, C$H_{PYE\ \beta}$), 6.85 (dd, J = 7.2, 2.8 Hz, 2H, C$H_{PYE\ \beta}$), 3.88 (s, 6H, NCH_3), 3.32 (t, J = 6.2 Hz, 4H, NH-CH_2-CH_2), 2.76 (t, J = 6.2 Hz, 4H, NH-CH_2-CH_2). ^{13}C{^{1}H} NMR (DMSO-*d*, 101MHZ): δ 163.4 ($C_{Ar/q}$), 140.7 (CH_α), 140.3 ($CH_{\alpha'}$), 117.0 ($CH_{\beta'}$), 109.2 (CH_β), 105.0 ($C_{Ar/q}$), 103.7 ($C_{Ar/q}$), 86.3 (*C*H), 83.0 (*C*H), 53.3 (CH_A), 53.0(*C*H), 43.7(CH_3), 31.8 (*C*H), 22.8 (*C*H), 18.7 (CH_3). 156.93 (*C*), 144.65 (*C*), 142.51 (*C)*, 110.62 (*C*), 105.52 (*C*), 47.41 (NH-CH_2-CH_2), 44.46 (CH_3), 42.72 (NH-CH_2-CH_2). HR-MS (m/z): calculated for $[M- PF_6]^+$: 432.1747 found 432.1741. Elemental analysis calculated for $C_{16}H_{25}F_{12}N_5P_2$ (%): C, 33.29; H, 4.36; N, 12.13; found C, 33.62; H, 4.45; N, 12.29.

Complex 6:

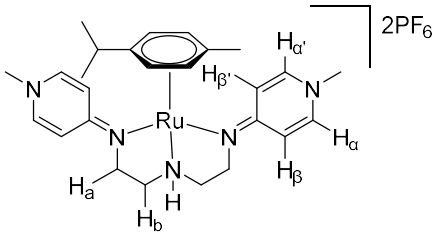

Alkyl-bis-PYE (28.9 mg, 0.05 mmol) was dissolved in dry CH_3CN (5 mL) with Na_2CO_3 (31.8 mg, 0.3 mmol) and $[RuCl_2(p\text{-cymene})]_2$ (15.5 mg, 0.025 mmol) was added to the solution. The mixture was stirred for 2 hours at reflux. The mixture was filtered and the solvent removed under reduced pressure to obtain **6** as a yellow solid (40 mg, 99% yield). Crystals suitable for X-Ray diffraction analysis were obtained from slow diffusion of diethyl ether in a dichloromethane solution. ^{1}H NMR (CD_3CN, 300 MHz): δ 7.35 (dd, J = 7.7, 2.1 Hz, 2H, C$H_{a'}$), 7.25 (dd, *J* = 7.8, 2.1 Hz, 2H, CH_a), 7.28 (br, 1H, N*H*), 6.81 (dd, J = 7.7, 3.2 Hz, 2H, C$H_{b'}$), 6.45 (dd, J = 7.8, 3.2 Hz, 2H, CH_b), 5.98 (d, J = 6.1 Hz, 2H, CH_D), 5.67 (d, J = 6.1 Hz, 2H, CH_C), 3.62 (s, N- 3H, CH_3), 3.06–2.91 (m, 6H, CH_A 4H and CH_B 2H), 2.64 (hept, J = 7.0 Hz, 1H, C*H*(CH_3)$_2$), 1.96 (s, 3H, CH_3), 2.47-2.57 (m, 2H, CH_B), 1.11 (d, J = 6.9 Hz, 6H, CH(CH_3)$_2$). ^{13}C{^{1}H} NMR (CD_3CN, 75 Mhz): δ 163.4 ($C_{Ar/q}$), 140.7 (CH_a), 140.3 ($CH_{a'}$), 117.0 ($CH_{b'}$), 109.2 (CH_b), 105.0 ($C_{Ar/q}$), 103.7 ($C_{Ar/q}$), 86.3 (CH_D), 83.0 (CH_C), 53.3 (CH_A), 53.0(CH_B), 43.7(CH_3), 31.8 (*C*H(CH_3)$_2$), 22.8 (CH(*C*H_3)$_2$), 18.7 (*C*H_3). HR-MS (m/z): calculated for $[M- PF_6]^+$: 666.1734 found 666.1743. Anal. Calc. (%) for [Chemical Formula: $C_{26}H_{37}F_{12}N_5P_2Ru$]: C, 38.52; H, 4.60; N, 8.64; found C, 38.62; H, 4.65; N, 8.69.

Complex 7

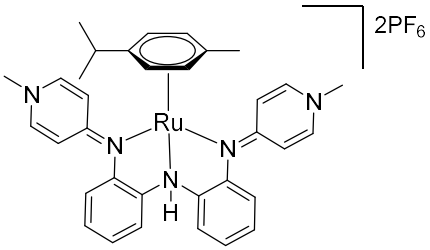

Aryl-bis-PYE (67 mg, 0.1 mmol) was dissolved in dry CH_2Cl_2 (5 mL) and tBuOK (56 mg, 0.5 mmol) was added. The mixture was stirred 10min at RT and [$RuCl_2$(*p*-cymene)]$_2$ (30.5 mg, 0.05 mmol) was added to the solution. The mixture was stirred for 16 hours at room temperature and filtrated. Pentane (20 mL) was added to the filtrate and the resulting solid was collected and dried as the pure complex (70 mg, 0.078 mmol, 78% yield). ^{1}H NMR (300 MHz, CD_3CN): δ 7.88 (d, J = 7.4 Hz, 4H, CH_a), 7.27 (d, J = 7.5 Hz, 4H, CH_{Ar}), 7.17 (d, J = 7.5 Hz, 2H, CH_{Ar}), 7.07 (t, J = 7.5 Hz, 2H, CH_{Ar}), 6.83 (d, J = 7.4 Hz, 4H, CH_β), 6.32 (s, 1H, Ar_2NH), 5.35 (d, J = 6.0 Hz, 2H, *p*-cymene-CH_{Ar}), 5.11 (d, J = 6.0 Hz, 2H, *p*-cymene-CH_{Ar}), 3.89 (s, 6H, NCH_3), 2.66 (h, J = 6.8 Hz, 1H, (d, J = 7.0 Hz, 6H, *p*-cymene-CH(CH_3)$_2$)), 1.94 (s, 3H, *p*-cymene-CH_3), 1.05 (d, J = 7.0 Hz, 6H, *p*-cymene-CH(CH_3)$_2$). ^{13}C{^{1}H} NMR (75 MHz, CD_3CN): δ 157.40 (C_g), 144.75 (C_{Ar}), 139.71 (C_a), 129.89 (C_{Ar}), 127.82 (C_{Ar}), 123.62 (C_{Ar}), 121.15 (C_{Ar}), 110.92 (C_b), 103.24 ($C_{p\text{-}Cymene}$), 99.75 ($C_{p\text{-}Cymene}$), 84.37 ($C_{p\text{-}Cymene}$), 81.97 ($C_{p\text{-}Cymene}$), 46.04 (NCH_3), 31.54 ($CH(CH_3)_2$), 22.34 (CH_3), 18.94 (CH(CH_3)$_2$). HRMS: 762.1731 (M–PF_6)$^+$, calcd 762.1734 (M–PF_6)$^+$. Anal. Calc. (%) for [Chemical Formula: $C_{34}H_{37}F_{12}N_5P_2Ru$]: C, 45.04; H, 4.11; N, 7.72; found C, 45.37; H, 4.33; N, 7.92.

Ligand 8a

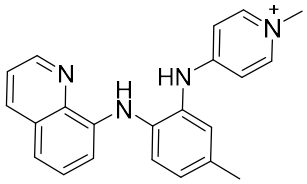

4-iodo-3-nitrotoluene (912.2 mg, 3.47 mmol), 8-aminoquinoline (500 mg, 3.47 mmol), CuI (66.1 mg, 347 µmol), 1,10-phenanthroline (125 mg, 695 µmol) and Na_2CO_3 (958.58 mg, 6.94 mmol) were placed under N_2 atmosphere in a sealed vial. DMSO (3 mL) was added and the mixture stirred at 90 °C for 5 days. The resulting mixture was diluted with water (100 mL) and extracted with CH_2Cl_2 (75 mL). The extract was washed with water (2 × 50 mL) and dried over $MgSO_4$. All volatiles were removed under reduced pressure. The crude product was further purified by gradient column chromatography (SiO_2; pentane/CH_2Cl_2 1:1 to 1:9). The desired compound eluted as an intensely orange fraction which was evaporated to dryness under reduced pressure. The resulting orange solid (720 mg, 74%) was directly used for further synthesis without full characterisation. ^{1}H NMR (300 MHz, DMSO-d_6) δ 10.68 (s, 1H), 8.95 – 8.87 (m, 1H), 8.38 (d, *J* = 8.5 Hz, 1H), 8.06 – 7.93 (m, 2H,), 7.81 (d, *J* = 8.6 Hz, 1H), 7.73 (d, *J* = 6.9 Hz, 1H), 7.66 – 7.45 (m, 3H), 2.30 (s, 3H).

The nitro compound (668 mg, 2.39 mmol) and Pd/C (65.5 mg) were mixed in absolute ethanol (35 mL). Hydrazine monohydrate (0.7 mL, 14 mmol) was added and the mixture heated to reflux for 1 h during which the solution went from intensely orange to a greenish tinted light yellow. The resulting mixture was cooled to room temperature and filtered through Celite. All volatiles were removed under reduced pressure. The resulting oil was dissolved in ethyl acetate (50 mL) and washed with saturated $NaHCO_3$ (50 mL), water (50 mL) and brine (50 mL). The solution was dried over $MgSO_4$ and all volatiles were removed under reduced pressure to yield a light orange oil (567.7 mg, 95%) which was directly used for further synthesis without full characterisation. ^{1}H NMR (300 MHz, CD_3CN) δ 8.79 (dd, $^3J_{HH}$ = 4.2, $^4J_{HH}$ = 1.7 Hz, 1H), 8.20 (dd, $^3J_{HH}$ = 8.3, $^4J_{HH}$ = 1.7 Hz, 1H), 7.54 (s, 1H), 7.48 (dd, $^3J_{HH}$ = 8.3, $^3J_{HH}$ = 4.2 Hz, 1H),

7.33 (t, $^3J_{HH}$ = 7.9 Hz, 1H), 7.22 – 7.13 (m, 1H), 7.08 (d, $^3J_{HH}$ = 7.9 Hz, 1H), 6.73 – 6.67 (m, 1H), 6.62 (dd, $^3J_{HH}$ = 7.6, $^4J_{HH}$ = 1.3 Hz, 1H), 6.59 – 6.51 (m, 1H), 4.10 (s, 2H), 2.27 (s, 3H).

The intermediate (567 mg, 2.27 mmol) was mixed with with 4-chloro-1-methylpyridinium triflate (568.28 mg, 2.05 mmol) and placed under N_2 atmosphere. The reaction was heated to 120 °C for 1 h. The crude product was washed with Et_2O (2 × 30 mL) and CH_2Cl_2 (3 × 50 mL). All volatiles were removed under reduced pressure to yield **8a** as a yellow solid (716.5 mg, 64%). ^{1}H NMR (400 MHz, CD_3CN) δ 9.88 (s, 1H, NH_{PYE}), 9.00 (dd, $^3J_{HH}$ = 8.4, $^4J_{HH}$ = 1.6 Hz, 1H, H_{Quin}), 8.92 (dd, $^3J_{HH}$ = 5.4, $^4J_{HH}$ = 1.6 Hz, 1H, H_{Quin}), 8.75 (s, 1H, NH_{Quin}), 7.98 (dd, $^3J_{HH}$ = 8.4, $^4J_{HH}$ = 5.3 Hz, 1H, H_{Quin}), 7.88 (d, $^3J_{HH}$ = 7.3 Hz, 2H, C$H_{\alpha\ PYE}$), 7.80 – 7.67 (m, 3H, H_{Quin}), 7.40 (d, $^3J_{HH}$ = 8.2 Hz, 1H, CH_{ph}), 7.29 – 7.24 (m, 1H, CH_{ph}), 7.19 (dd, $^3J_{HH}$ = 8.4, $^4J_{HH}$ = 2.0 Hz, 1H, CH_{ph}), 7.07 (d, $^3J_{HH}$ = 7.0 Hz, 2H, C$H_{\beta\ PYE}$), 3.85 (s, 3H, NCH_3), 2.36 (s, 3H, CCH_3). ^{13}C{^{1}H} NMR (101 MHz, CD_3CN) δ 157.20 (CH_q), 148.21 (CH_{Quin}), 144.74 (C$H_{\alpha\ PYE}$), 143.89 (CH_{Quin}), 136.24, 135.02, 134.88, 131.77, 131.62 (5 × CH_q), 131.39 (CH_{Quin}), 130.10 (CH_{ph}), 128.76 (CH_q), 127.99 (CH_{ph}), 122.82 (CH_{Quin}), 121.17 (CH_{ph}), 121.13, 120.20 (2 × CH_{Quin}), 45.92 (NCH_3), 20.72 (CCH_3). HR-MS (m/z): calculated for $[M\text{-}OTf]^+$ = 341.1761; found: 341.1759. Elemental analysis calculated for $C_{23}H_{21}F_3N_4O_3S$ (%): C 56.32, H 4.32, N 11.42; found: C 52.38, H 4.14, N 10.6.

Ligand precursor 8b

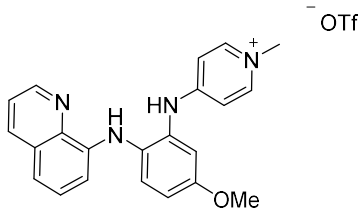

4-iodo-3-nitroanisole (967.7 mg, 3.47 mmol), 8-aminoquinoline (500 mg, 3.47 mmol), CuI (66.1 mg, 346.8 µmol), 1,10-phenanthroline (125 mg, 693.6 µmol) and Na_2CO_3 (958.58 mg, 6.94 mmol) were placed under N_2 atmosphere in a sealed vial. DMSO (3mL) was added and the mixture stirred at 90 °C for 4 days. The resulting mixture was diluted with water (100 mL) and extracted with CH_2Cl_2 (75 mL). The extract was washed with water (2 × 50 mL) and dried over $MgSO_4$. All volatiles were removed under reduced pressure. The crude product was further purified by gradient column chromatography (SiO_2; pentane/CH_2Cl_2 1:1 to 1:9). The desired compound eluted as an intensely orange coloured fraction which was evaporated to dryness under reduced pressure. The resulting orange solid (603 mg, 59%) was directly used for further synthesis without full characterisation. ^{1}H NMR (300 MHz, DMSO-d_6) δ 10.48 (s, 1H), 8.95 (dd, $^3J_{HH}$ = 4.3, $^4J_{HH}$ = 1.7 Hz, 1H), 8.41 (dd, $^3J_{HH}$ = 8.4, $^4J_{HH}$ = 1.7 Hz, 1H), 7.90 (d, $^3J_{HH}$ = 9.2 Hz, 1H), 7.71 – 7.62 (m, 3H), 7.61 – 7.51 (m, 2H$_I$), 7.39 (dd, $^3J_{HH}$ = 9.3, $^4J_{HH}$ = 3.1 Hz, 1H), 3.36 (s, 3H).

Ligand precursor (550 mg, 1.86 mmol) and Pd/C (44.1 mg) were mixed in absolute ethanol (24 mL). Hydrazine monohydrate (0.5 mL, 11.18 mmol) was added and the mixture heated to reflux for 1h during which the solution went from intensely orange to a greenish tinted light yellow. The resulting mixture was cooled to room temperature and filtered through Celite. All volatiles were removed under reduced pressure. The resulting oil was dissolved in ethyl acetate (50mL) and washed with saturated $NaHCO_3$ (50 mL), water (50 mL) and brine (50 mL). The solution was dried over $MgSO_4$ and all volatiles were removed under reduced pressure to yield a brownish oil (467.7 mg, 95%) which was directly used for further synthesis without full characterisation. ^{1}H NMR (300 MHz, CD_3CN) δ 7.53 (dd, $^3J_{HH}$ = 4.2, $^4J_{HH}$ = 1.7 Hz, 1H), 6.93 (dd, $^3J_{HH}$ = 8.3, $^4J_{HH}$ = 1.7 Hz, 1H), 6.29 – 6.15 (m, 2H), 6.05 (t, $^3J_{HH}$ = 7.9 Hz, 1H), 5.89 (dd, $^3J_{HH}$ = 8.2, $^4J_{HH}$ = 1.3 Hz, 1H), 5.81 (d, $^3J_{HH}$ = 8.5 Hz, 1H), 5.25 (dd, $^3J_{HH}$ = 7.6, $^4J_{HH}$ = 1.3 Hz, 1H), 5.18 (d, $^4J_{HH}$ = 2.8 Hz, 1H), 5.04 (dd, $^3J_{HH}$ = 8.5, $^4J_{HH}$ = 2.8 Hz, 1H), 2.95 (s, 2H), 2.50 (s, 3H).

The intermediate (441.8 mg, 1.67 mmol) was mixed with with 4-chloro-1-methylpyridinium triflate (437.19 mg, 1.58 mmol) and placed under N_2 atmosphere. The reaction was heated to 120 °C for 1 h. The crude product was washed with Et_2O (2 × 10 mL), ice-cold CH_2Cl_2 (7 × 10 mL) and THF (3 × 10 mL). All volatiles were removed under reduced pressure to yield **8b** as an orange solid (463 mg, 55%). ^{1}H NMR (400 MHz, CD_3CN) only one NH peak is observed δ 9.57 (s, 1H, NH_{PYE}), 8.95 – 8.84 (m, 2H, H_{Quin}), 7.93 (dd, $^3J_{HH}$ = 8.4, $^3J_{HH}$ = 5.3 Hz, 1H, H_{Quin}), 7.87 (d, $^3J_{HH}$ = 7.0 Hz, 2H, C$H_{\alpha\ PYE}$), 7.70 – 7.56 (m, 2H, H_{Ar}), 7.49 (d, $^3J_{HH}$ = 8.9 Hz, 1H, H_{Ar}), 7.45 – 7.38 (m, 1H, H_{Ar}), 7.15 – 6.92 (m, 4H, C$H_{\beta\ PYE}$, H_{Ar}), 3.84 (s, 3H, CH_3), 3.83 (s, 3H, CH_3). ^{13}C{^{1}H} NMR (101 MHz, CD_3CN) δ 158.02, 156.98 (2 × CH$_q$), 147.46 (CH$_{Quin}$), 144.84 (C$H_{\alpha\ PYE}$), 143.84 (CH$_{Quin}$), 138.01 (C$_q$), 131.88, 131.66, 131.34, 131.09 (2 × CH$_{Ar}$, 2 × CH$_q$), 129.52 (C$_q$), 125.73 (CH$_{Ar}$), 122.72 (CH$_{Quin}$), 119.48, 116.74, 115.14, 112.58 (4 × CH$_{Ar}$), 110.87 (CH$_{\beta\ PYE}$), 56.55 (CH_3), 46.01(CH_3). HR-MS (m/z): calculated for $[M\text{-}OTf]^+$ = 357.1710; found: 357.1705. Elemental analysis calculated for $C_{23}H_{21}F_3N_4O_4S$ (%): C 54.54, H 4.18, N 11.06; found: C 50.38, H 3.98, N 10.28.

Ligand precursor 8c

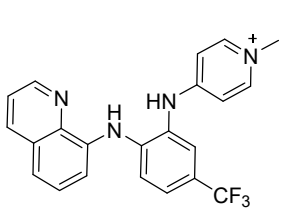

$^-$OTf

1-Fluoro-2-nitro-4-trifluoromethylbenzene (1.9 mL, 13.87 mmol) , 8-aminoquinoline (2000 mg, 13.87 mmol) and Na_2CO_3 (1760 mg, 16.65 mmol) were suspended in DMSO (7.5 mL) and stirred at 120 °C. The resulting mixture was diluted with water (100 mL) and extracted with CH_2Cl_2 (75 mL). The extract was washed with water (2 × 50 mL) and dried over $MgSO_4$. All volatiles were removed under reduced pressure. The crude product was further purified by gradient column chromatography (SiO_2; pentane/CH_2Cl_2 1:1 to 1:9). The desired compound eluted as an intensely orange coloured fraction which was evaporated to dryness under reduced pressure. The resulting orange solid (1897.5 mg, 41%) was directly used for further synthesis without full characterisation. ^{1}H NMR (300 MHz, DMSO-d_6) δ 11.06 (s, 1H), 8.98 (dd, $^3J_{HH}$ = 4.2, $^4J_{HH}$ = 1.7 Hz, 1H), 8.53 – 8.44 (m, 2H), 7.98 – 7.88 (m, 3H), 7.81 (dd, $^3J_{HH}$ = 8.3, $^4J_{HH}$ = 1.3 Hz, 1H), 7.74 – 7.61 (m, 2H). ^{19}F NMR (282 MHz, DMSO) δ -60.60 (s, 3F, CCF_3).

The nitro compound (1700 mg, 5.76 mmol) and Pd/C (166.4 mg) were mixed in absolute ethanol (90mL). Hydrazine monohydrate (1.7 mL, 34.54 mmol) was added and the mixture heated to reflux for 1h during which the solution went from intensely orange to a greenish tinted light yellow. The resulting mixture was cooled to room temperature and filtered through Celite. All volatiles were removed under reduced pressure. The resulting oil was dissolved in ethyl acetate (50mL) and washed with saturated $NaHCO_3$ (50 mL), water (50 mL) and brine (50 mL). The solution was dried over $MgSO_4$ and all volatiles were removed under reduced pressure to yield a yellow oil. The oil was layered with pentane (50 mL) for 30min resulting in a solid which was washed with pentane (4 × 20 mL). This afforded a light beige solid (1186 mg, 77%) which directly used for further synthesis without full characterisation. ^{1}H NMR (300 MHz, DMSO-d_6) δ 8.87 (dd, $^3J_{HH}$ = 4.2, $^4J_{HH}$ = 1.7 Hz, 1H), 8.33 (dd, $^3J_{HH}$ = 8.3, $^4J_{HH}$ =1.7 Hz, 1H), 8.08 (s, 1H), 7.59 (dd, $^3J_{HH}$ = 8.3, 4.2 Hz, 1H), 7.49 – 7.38 (m, 2H), 7.34 (dd, $^3J_{HH}$ = 8.2, $^4J_{HH}$ =1.3 Hz, 1H), 7.13 (d, $^4J_{HH}$ = 2.2 Hz, 1H), 7.07 (dd, $^3J_{HH}$ = 7.6, $^4J_{HH}$ =1.3 Hz, 1H), 6.91 (dd, $^3J_{HH}$ = 8.4, $^4J_{HH}$ =2.2 Hz, 1H), 5.35 (s, 2H).

The intermediate (500 mg, 1.65 mmol) was mixed with with 4-chloro-1-methylpyridinium triflate (444 mg, 1.6 mmol) and placed under N_2 atmosphere. The reaction was heated to 120 °C for 1 h. The crude product was washed with CH_2Cl_2 (3 × 50 mL). All volatiles were removed under reduced pressure to yield **8c** as a yellow solid (630.7 mg, 41%). ^{1}H NMR (400 MHz, CD_3CN) δ 10.70 (s, 1H, NH_{PYE}), 9.10 (d, $^3J_{HH}$ = 8.4

Hz, 1H, H_{Quin}), 9.02 (d, $^3J_{HH}$ = 5.3 Hz, 1H, H_{Quin}), 8.32 (s, 1H, NH_{Quin}), 8.11 – 8.01 (m, 3H, CH_{Quin}, CH_{Ph}), 7.98 (d, $^3J_{HH}$ = 7.1 Hz, 2H, $CH_{\alpha\ PYE}$), 7.96 – 7.89 (m, 1H, $CH_{ph/Quin}$), 7.71 (s, 1H, $H_{Ph/Quin}$), 7.54 (d, $^3J_{HH}$ = 8.7 Hz, 1H, $CH_{Ph/Quin}$), 7.37 (d, $^3J_{HH}$ = 8.7 Hz, 1H, $CH_{ph/Quin}$), 7.21 – 7.15 (m, 2H, $CH_{\beta\ PYE}$), 3.91 (s, 3H, CH_3). $^{13}C\{^1H\}$ NMR (101 MHz, CD_3CN) δ 160.16, 157.70, 148.46, 145.13, 143.57, 134.29, 133.09, 131.77, 131.25, 127.64, 126.76 – 126.59 (m), 126.22, 125.38 – 125.19 (m), 125.52, 123.40, 116.18 ($CH_{ph/Quin}$), 46.16 (NCH_3). HR-MS (m/z): calculated for $[M–OTf]^+$ = 395.1478; found: 395.1472. Elemental analysis calculated for $C_{23}H_{18}F_6N_4O_3S$ (%): C 50.74, H 3.33, N 10.29; found: C 47.31, H 3.24, N 9.62.

Complex 9a

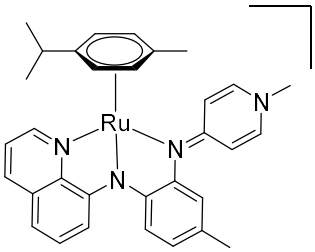

Under nitrogen atmosphere and under exclusion of light, [Ru(*p*-Cl_2cymene)]$_2$ (74.9 mg, 0.122 mmol), ligand precursor **8a** (120 mg, 0.245 mmol) and Na_2CO_3 (259.3 mg, 2.45 mmol) were stirred in degassed CH_3CN (3 mL) for 3 days. The mixture was filtered over filterpaper and evaporated to dryness. The solid was redissolved in dry CH_3CN and the resulting solution filtered over a short pad of basic Al_2O_3. All volatiles were evaporated under reduced pressure yielding **9a** as a red powder (120 mg, 68%). ^1H NMR (400 MHz, CD_3CN) δ 9.44 (dd, $^3J_{HH}$ = 5.0, $^4J_{HH}$ 1.4 Hz, 1H, H_{Quin}), 8.13 (dd, $^3J_{HH}$ = 8.4, $4J_{HH}$ = 1.3 Hz, 1H, H_{Quin}), 7.41 – 7.31 (m, 2H, H_{Ar}), 7.30 – 7.21 (m, 2H, $H_{PYE\ \alpha}$, H_{Ar}), 7.13 (d, $^3J_{HH}$ = 7.8 Hz, 1H, H_{Ar}), 7.03 – 6.89 (m, 4H, $H_{PYE\ \alpha}$, H_{ph}, 2 H_{Ar}), 6.84 – 6.74 (m, 2H, H_{ph}, H_{Ar}), 5.77 – 5.71 (m, 2H, H_{cym}), 5.68 – 5.62 (m, 1H, H_{cym}), 5.12 (d, $^3J_{HH}$ = 5.9 Hz, 1H, H_{cym}), 3.48 (s, 3H, pyr–CH_3), 2.37 (hept, $^3J_{HH}$ = 6.9 Hz, 1H, $CHMe_2$), 2.25 (s, 3H,$C_{ph}CH_3$), 1.92 (s, 3H, cym–CH_3), 0.89 – 0.81 (m, 6H, $(CH_3)_2CH$). $^{13}C\{^1H\}$ NMR (101 MHz, CD_3CN) δ 160.75 (C_{Ar}), 154.64, 154.41 (1 × CH_{Ar}, 1 × CH_{Quin}), 148.17 (C_{Ar}), 141.43, 140.78 (2 × CH_{Ar}), 138.16 (CH_{Quin}), 132.46, 130.97 (2 × C_{Ar}), 129.93, 124.86, 124.71 (3 × CH_{Ar}), 123.80 (C_{OTf}), 123.18, 120.81, 120.61, 119.11, 116.59, 114.40, 109.65 (7 × CH_{Ar}), 102.98, 102.65 (2 × C_{Ar}), 88.27, 87.93, 86.42, 84.62 (4 × C_{cym}–H), 43.81 (N–CH_3), 31.30 ($CHMe_2$), 22.67, 21.81 (2 × $CH(CH_3)_2$), 21.07 ($CH_{3\ ph}$), 18.53 (cym–CH_3). HR-MS (m/z): Calculated for $[M–OTf]^+$ = 575.1743 found 575.1763. Anal. Calc. (%) for $C_{33}H_{33}F_3N_4O_3RuS$: C 54.76, H 4.60, N 7.74; found C 53.85, H 4.57, N 7.39.

Complex 9b

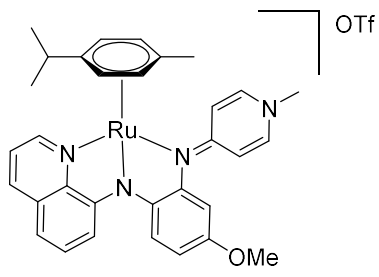

Under nitrogen atmosphere and under exclusion of light, [Ru(*p*-cymene)Cl_2]$_2$ (60.5 mg, 0.098 mmol), ligand precursor **8b** (100 mg, 0.197 mmol) and Na_2CO_3 (209.3 mg, 1.97 mmol) were stirred in degassed CH_3CN (3 mL) for 3 days. The mixture was filtered over filterpaper and evaporated to dryness. The solid was redissolved in CH_2Cl_2 and loaded onto a short pad of basic Al_2O_3. The complex was then eluted with acetone (60 mL). All volatiles were evaporated under reduced pressure and the solid redissolved in a minimal amount of CH_2Cl_2. Et_2O was added until the complex precipitated and the supernatant was removed. The resulting solid was washed with Et_2O (2 × 30 mL) and pentane (2 × 30 mL) yielding **9c** as a red powder (95 mg, 65%). ^1H NMR (400 MHz, CD_3CN) δ 9.43 (dd, $^3J_{HH}$ = 5.1, $^4J_{HH}$ = 1.3 Hz, 1H, H_{Quin}), 8.13 (dd, $^3J_{HH}$ = 8.4, $^4J_{HH}$ = 1.3 Hz, 1H, H_{Quin}), 7.40 – 7.32 (m, 2H, H_{Ar}, H_{ph}), 7.31 –

7.22 (m, 2H, $H_{PYE\ \alpha}$, H_{Ar}), 7.11 (d, $^3J_{HH}$ = 7.8 Hz, 1H, CH_{Ar}), 7.04 – 6.95 (m, 2H, $H_{PYE\ \alpha}$, H_{Ar}), 6.92 (d, $^3J_{HH}$ = 7.8 Hz, 1H, CH_{Ar}), 6.85 – 6.78 (m, 1H, H_{Ar}), 6.76 (d, $^4J_{HH}$ = 2.7 Hz, 1H, H_{ph}), 6.51 (dd, $^3J_{HH}$ = 8.4, $^4J_{HH}$ = 2.7 Hz, 1H, H_{ph}), 5.78 – 5.71 (m, 2H, H_{cym}), 5.69 – 5.63 (m, 1H, H_{cym}), 5.13 (d, $^3J_{HH}$ = 6.0 Hz, 1H, H_{cym}), 3.74 (s, 3H, OCH_3), 3.49 (s, 3H, pyr–CH_3), 2.39 (hept, $^3J_{HH}$ = 6.9 Hz, 1H, $CHMe_2$), 1.97 – 1.91 (overlappend with solvent, 3H, cym–CH_3) 0.90 – 0.83 (m, 6H, $(CH_3)_2CH$). $^{13}C\{^1H\}$ NMR (101 MHz, CD_3CN) δ 160.89 (C_{Ar}), 155.41 (C_{Ar}), 155.17 (C_{Ar}), 154.56 (CH_{Quin}), 153.80 (C_{Ar}), 148.11 (C_{Ar}), 141.53(CH_{Ar}), 141.02 (CH_{Ar}), 138.18 (CH_{Quin}), 130.97(C_{Ar}), 129.94(CH_{Ar}), 124.91 (CH_{Ar}), 123.85(C_{OTf}), 123.17 (CH_{Ar}), 119.17 (CH_{Ar}), 116.74 (CH_{Ar}), 114.35 (CH_{Ar}), 109.84 (C_{Ar}), 108.09 (CH_{ph}), 107.39 (CH_{ph}), 102.86 (C_{Ar}), 88.39, 87.92, 86.42, 84.55 (4 × C_{cym}–H), 56.33 (OCH_3), 43.90 (N–CH_3), 31.33 ($CHMe_2$), 22.71, 21.86 (2 × $CH(CH_3)_2$), 18.59 (cym–CH_3). HR-MS (m/z): Calculated for $[M–OTf]^+$ = 591.1692 found 591.1714. Anal. Calc. (%) for $C_{33}H_{33}F_3N_4O_4RuS$: C 53.58, H 4.50, N 7.57; found 50.92, H 3.83, N 6.93.

Complex 9c

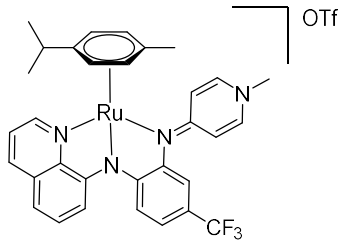

Under nitrogen atmosphere and under exclusion of light, [Ru(*p*-cymene)Cl_2]$_2$ (90.0 mg, 0.165 mmol mmol), ligand precursor **8c** (50.6 mg, 0.83 mmol) and Na_2CO_3 (175 mg, 1.65 mmol) were stirred in degassed CH_3CN (3 mL) for 16 h. The mixture was filtered over filterpaper and evaporated to dryness. The solid was redissolved in CH_2Cl_2 and loaded onto a short pad of basic Al_2O_3. The complex was then eluted with acetone (60 mL). All volatiles were evaporated under reduced pressure and the solid redissolved in a minimal amount of CH_2Cl_2. Et_2O was added until the complex precipitated and the supernatant was removed. The resulting solid was washed with Et_2O (2 × 30 mL) and pentane (2 × 30 mL) yielding the product as a orange-red powder (80 mg, 62%). ^1H NMR (400 MHz, CD_3CN) δ 9.48 (d, $^3J_{HH}$ = 5.0 Hz, 1H, H_{Quin}), 8.18 (d, $^3J_{HH}$ = 8.4 Hz, 1H, H_{Quin}), 7.59 (d, $^3J_{HH}$ = 8.1 Hz, 1H, H_{Ar}), 7.46 – 7.36 (m, 3H, $H_{PYE\ \alpha}$, 2H_{Ar}), 7.36 – 7.22 (m, 3H, H_{Ar}), 7.18 – 7.09 (m, 1H, H_{Ar}), 7.08 – 6.98 (m, 2H, $H_{PYE\ \alpha}$, H_{Ar}), 6.85 – 6.72 (m, 1H, H_{Ar}), 5.80 – 5.75 (m, 2H, H_{cym}), 5.70 (d, $^3J_{HH}$ = 6.0 Hz, 1H, H_{cym}), 5.25 (d, $^3J_{HH}$ = 6.0 Hz, 1H, H_{cym}), 3.53 (s, 3H, pyr–CH_3), 2.36 (h, *J* = 7.0 Hz, 1H, $CHMe_2$), 1.96 – 1.92 (overlapping with solvent, 3H, cym–CH_3), 0.85 (d, $^3J_{HH}$ = 2.8 Hz, 3H, $(CH_3)_2CH$), 0.84 (d, $^3J_{HH}$ = 2.9 Hz, 3H, $(CH_3)_2CH$). $^{13}C\{^1H\}$ NMR (101 MHz, CD_3CN) δ 163.78, 161.59, 158.42, 155.53 (4 × C_{Ar}), 155.26 (CH_{Quin}), 148.40 (C_{Ar}), 142.02, 141.41 (2 × CH_{Ar}), 138.47 (CH_{Quin}), 130.94 (C_{Ar}), 129.97 (CH_{Ar}), 128.51, 126.97 (2 × C_{Ar}), 125.62 (CH_{Ar}), 124.27, 124.02, 123.70 (3 × C_{Ar}), 123.38 (CH_{Ar}), 121.60 – 121.35 (m, CH_{Ph}), 119.62, 116.82 (2 × CH_{Ar}), 116.67 – 116.52 (m, CH_{Ph}), 115.60 (CH_{Ar}), 109.38 (CH_{Ar}), 103.22, 102.94 (2 × C_{Ar}), 88.25, 88.07, 86.43, 84.63 (4 × C_{cym}–H), 44.08 (N–CH_3), 31.28 ($CHMe_2$), 22.55, 21.79 (2 × $CH(CH_3)_2$), 18.55 (cym–CH_3). ^{19}F NMR (282 MHz, CD_3CN) δ -61.95 (CF_3), -79.34 (OTf). HR-MS (m/z): Calculated for $[M–OTf]^+$ = 629.1461 found 629.1485. Anal. Calc. (%) for $C_{33}H_{30}F_6N_4O_3RuS$: C 50.96, H 3.89, N 7.20; found 50.41, H 3.80, N 6.91.

General Catalytic procedure

A stock solution of complex **2a** (7.53 mg in 5 mL CH_3CN, 10.6 mM) was prepared under exclusion of light and kept protected from light. An aliquot of the solution (1 mL, 2,13 µmol) was transferred into a 10 mL two-neck round-bottom flask and, under exclusion of light, all volatiles were evaporated under reduced pressure. The flask was equipped with a magnetic stirrer bar and a condenser. The condenser was connected to a three-way valve, connected to a Schlenk line and to a BlueV count volumetric gas

measurement device. The round bottom flask and condenser were put under N_2 atmosphere. Under N_2 pressure the valve is opened to the volumetric counter and the tubing flushed with nitrogen. Degassed solvent (1.2 mL) was added to the round bottom flask, the valve to the Schlenk line was closed and the mixture submerged into a preheated oil bath for 10 min. Degassed formic acid (40 µl, 98% purity) was injected (time = 0), and gas evolution was monitored with the BlueV count device unless noted otherwise.

Crystal Structure determination

A crystal of **3-6** and **9a–c** was immersed in parabar oil was mounted at ambient conditions and transferred into the stream of nitrogen (173 K). Measurements of **3** and **5** - **9** were made on a *RIGAKU Synergy S* area-detector diffractometer[22] using mirror optics monochromated Cu *K*α radiation (λ = 1.54184 Å). 4 was measured on an *Oxford Diffraction SuperNova* area-detector diffractometer[22] using mirror optics monochromated Mo *K*α radiation (λ = 0.71073 Å) and Al filtered.[23]

Data reduction was performed using the *CrysAlisPro*[22] program. The intensities were corrected for Lorentz and polarization effects, and an absorption correction based on the multi-scan method using SCALE3 ABSPACK in *CrysAlisPro*[22] was applied. The structure was solved by intristic phasing using *SHELXT*[24], which revealed the positions of all non-hydrogen atoms of the title compound. All atoms were refined anisotropically and H-atoms were assigned in geometrically calculated positions and refined using a riding model where each H-atom was assigned a fixed isotropic displacement parameter with a value equal to 1.2Ueq of its parent atom (1.5Ueq for methyl groups). Refinement of the structure was carried out on F^2 using full-matrix least-squares procedures, which minimized the function $\Sigma w(F_o^2 - F_c^2)^2$. The weighting scheme was based on counting statistics and included a factor to downweight the intense reflections. All calculations were performed using the *SHELXL-2014/7*[25] program in OLEX2. [26] For **3** twinning could be detected on the frames where the second component corresponds to a rotation of 179.95 degrees around 0.0001 -0.0006 1.0000 (reciprocal) or 0.2277 -0.0010 0.9737 (direct) direction with refined fractional contribution of 0.4443(15). The structure was refined against the reflection file treated from the twinning containing both components (hkl5 format). Disorder models were included for **3**, **9b** and **9c** for one of the triflate anions, for **5** for one of the rotating methyl units and for 6 for the DCM unit. The occupancies of each disorder component were refined through the use of a free variable. The sum of equivalent components was constrained to 1 i.e. 100%. For **5** a solvent mask was used to include the contribution of electron densities from void areas into the calculated structure factors. Further crystallographic details are compiled in tables 4-7.

Table 4. Crystal data and structure refinement for **3** and **4**.

Identification code	**3**	**4**
Empirical formula	$C_{34}H_{34}F_6N_4O_6RuS_2$	$C_{28}H_{23}F_3N_4O_3RuS$
Formula weight	873.84	653.63
Temperature/K	173.01(10)	173.00(10)
Crystal system	monoclinic	triclinic
Space group	$P2_1/c$	P-1
a/Å	9.33077(6)	9.12386(11)
b/Å	21.64536(19)	11.31527(17)
c/Å	18.00928(17)	12.81351(17)
α/°	90	84.9413(12)
β/°	95.4841(7)	79.9462(11)
γ/°	90	79.5257(12)
Volume/Å^3	3620.65(5)	1278.66(3)
Z	4	2
ρ_{calc}g/cm^3	1.603	1.698
μ/mm^{-1}	5.305	0.757
F(000)	1776.0	660.0
Crystal size/mm^3	0.344 × 0.073 × 0.055	0.538 × 0.407 × 0.312
Radiation	Cu Kα (λ = 1.54184)	Mo Kα (λ = 0.71073)
2Θ range for data collection/°	6.402 to 142.126	3.234 to 60.066
Index ranges	-9 ≤ h ≤ 11, -26 ≤ k ≤ 26, -22 ≤ l ≤ 22	-12 ≤ h ≤ 12, -15 ≤ k ≤ 15, -18 ≤ l ≤ 18
Reflections collected	63203	75399
Independent reflections	6996 [R_{int} = 0.0713, R_{sigma} = 0.0293]	7469 [R_{int} = 0.0325, R_{sigma} = 0.0160]
Data/restraints/parameters	6996/146/538	7469/54/410
Goodness-of-fit on F^2	1.049	1.083
Final R indexes [I>=2σ (I)]	R_1 = 0.0416, wR_2 = 0.1039	R_1 = 0.0231, wR_2 = 0.0605
Final R indexes [all data]	R_1 = 0.0464, wR_2 = 0.1061	R_1 = 0.0236, wR_2 = 0.0608
Largest diff. peak/hole / e Å^{-3}	0.88/-1.05	0.65/-0.73

Table 5. Crystal data and structure refinement for **5** and **6**.

Identification code	**5**	**6**
Empirical formula	$C_{34}H_{34}F_6N_4O_6RuS_2$	$C_{27}H_{39}Cl_2F_{12}N_5P_2Ru$
Formula weight	C34H35F3N4O3RuS	895.54
Temperature/K	737.79	173.01(10)
Crystal system	173.01(10)	monoclinic
Space group	monoclinic	$P2_1/n$
a/Å	P21/n	16.42378(7)
b/Å	10.82130(10)	11.94719(4)
c/Å	13.80280(10)	19.05613(8)
α/°	21.7442(2)	90
β/°	90	105.2635(4)
γ/°	95.3720(10)	90
Volume/Å^3	90	3607.26(3)
Z	3233.54(5)	4
ρ_{calc}g/cm^3	4	1.649
μ/mm^{-1}	1.516	6.546
F(000)	5.028	1808.0
Crystal size/mm^3	1512.0	0.198 × 0.129 × 0.094
Radiation	0.4 × 0.27 × 0.16	Cu Kα (λ = 1.54184)
2Θ range for data collection/°	Cu Kα (λ = 1.54184)	6.334 to 145.602
Index ranges	7.596 to 133.51	-20 ≤ h ≤ 20, -14 ≤ k ≤ 14, -23 ≤ l ≤ 23
Reflections collected	-12 ≤ h ≤ 12, -16 ≤ k ≤ 12, -25 ≤ l ≤ 25	71672
Independent reflections	29101	7181 [R_{int} = 0.0361, R_{sigma} = 0.0158]
Data/restraints/parameters	5732 [R_{int} = 0.0546, R_{sigma} = 0.0288]	7181/19/473
Goodness-of-fit on F^2	5732/25/422	0.993
Final R indexes [I>=2σ (I)]	1.029	R_1 = 0.0327, wR_2 = 0.0854
Final R indexes [all data]	R_1 = 0.0421, wR_2 = 0.1101	R_1 = 0.0331, wR_2 = 0.0858
Largest diff. peak/hole / e Å^{-3}	R_1 = 0.0432, wR_2 = 0.1115	0.78/-1.05

Table 6. Crystal data and structure refinement for **Alkyl-bisPYE** and **9a**.

Identification code	**Alkyl-bisPYE**	**9a**
Empirical formula	$C_{27}H_{39}Cl_2F_{12}N_5P_2Ru$	$C_{33}H_{33}F_3N_4O_3RuS$
Formula weight	895.54	723.76
Temperature/K	173.01(10)	173.00(10)
Crystal system	monoclinic	monoclinic
Space group	$P2_1/n$	$P2_1/c$
a/Å	16.42378(7)	19.3201(2)
b/Å	11.94719(4)	11.73675(12)
c/Å	19.05613(8)	14.35967(16)
α/°	90	90
β/°	105.2635(4)	100.0603(11)
γ/°	90	90
Volume/Å^3	3607.26(3)	3206.07(6)
Z	4	4
ρ_{calc}g/cm^3	1.649	1.499
μ/mm^{-1}	6.546	5.060
F(000)	1808.0	1480.0
Crystal size/mm^3	0.198 × 0.129 × 0.094	0.235 × 0.204 × 0.054
Radiation	Cu Kα (λ = 1.54184)	Cu Kα (λ = 1.54184)
2Θ range for data collection/°	6.334 to 145.602	4.646 to 160.52
Index ranges	-20 ≤ h ≤ 20, -14 ≤ k ≤ 14, -23 ≤ l ≤ 23	-24 ≤ h ≤ 24, -14 ≤ k ≤ 14, -18 ≤ l ≤ 18
Reflections collected	71672	12869
Independent reflections	7181 [R_{int} = 0.0361, R_{sigma} = 0.0158]	12869 [R_{int} = ?, R_{sigma} = 0.0066]
Data/restraints/parameters	7181/19/473	12869/97/467
Goodness-of-fit on F^2	0.993	1.179
Final R indexes [I>=2σ (I)]	R_1 = 0.0327, wR_2 = 0.0854	R_1 = 0.0548, wR_2 = 0.2082
Final R indexes [all data]	R_1 = 0.0331, wR_2 = 0.0858	R_1 = 0.0559, wR_2 = 0.2114
Largest diff. peak/hole / e Å^{-3}	0.78/-1.05	0.88/-0.99

Table 7. Crystal data and structure refinement for **9b** and **9c**.

Identification code	**9b**	**9c**
Empirical formula	$C_{33}H_{33}F_3N_4O_4RuS$	$C_{33}H_{30}F_6N_4O_3RuS$
Formula weight	739.76	777.74
Temperature/K	173.00(10)	172.93(16)
Crystal system	monoclinic	monoclinic
Space group	$P2_1/c$	$P2_1/c$
a/Å	20.20317(10)	19.40492(11)
b/Å	11.90647(6)	11.90961(6)
c/Å	14.05737(7)	14.36197(8)
α/°	90	90
β/°	109.4964(5)	100.9905(6)
γ/°	90	90
Volume/Å^3	3187.59(3)	3258.25(3)
Z	4	4
ρ_{calc}g/cm^3	1.541	1.585
μ/mm^{-1}	5.127	5.162
F(000)	1512.0	1576.0
Crystal size/mm^3	0.21 × 0.096 × 0.017	0.317 × 0.074 × 0.013
Radiation	Cu Kα (λ = 1.54184)	Cu Kα (λ = 1.54184)
2Θ range for data collection/°	8.758 to 138.61	4.638 to 140.124
Index ranges	-24 ≤ h ≤ 24, -14 ≤ k ≤ 14, -16 ≤ l ≤ 17	-23 ≤ h ≤ 23, -14 ≤ k ≤ 14, -17 ≤ l ≤ 17
Reflections collected	60163	63240
Independent reflections	5970 [R_{int} = 0.0333, R_{sigma} = 0.0163]	6196 [R_{int} = 0.0431, R_{sigma} = 0.0170]
Data/restraints/parameters	5970/0/475	6196/66/465
Goodness-of-fit on F^2	1.037	1.053
Final R indexes [I>=2σ (I)]	R_1 = 0.0195, wR_2 = 0.0513	R_1 = 0.0327, wR_2 = 0.0820
Final R indexes [all data]	R_1 = 0.0202, wR_2 = 0.0517	R_1 = 0.0335, wR_2 = 0.0824
Largest diff. peak/hole / e Å^{-3}	0.34/-0.32	0.65/-0.63

II.5 References

1 C. Liu, F. Li, L.-P. Ma and H.-M. Cheng, *Adv. Mater.*, 2010, **22**, E28–E62.

2 S. van Renssen, *Nat. Clim. Chang.*, 2020, **10**, 799–801.

3 N. Armaroli and V. Balzani, *Energy Environ. Sci.*, 2011, **4**, 3193.

4 L. Schlapbach and A. Züttel, *Nature*, 2001, **414**, 353–358.

5 P. Preuster, C. Papp and P. Wasserscheid, *Acc. Chem. Res.*, 2017, **50**, 74–85.

6 D. Mellmann, P. Sponholz, H. Junge and M. Beller, *Chem. Soc. Rev.*, 2016, **45**, 3954–3988.

7 N. Onishi, G. Laurenczy, M. Beller and Y. Himeda, *Coord. Chem. Rev.*, 2018, **373**, 317–332.

8 F. Joó, *ChemSusChem*, 2008, **1**, 805–808.

9 R. S. Coffey, *Chem. Commun. (London)*, 1967, 923b.

10 B. Loges, A. Boddien, H. Junge and M. Beller, *Angew. Chem. Int. Ed.*, 2008, **47**, 3962–3965.

11 C. Fellay, P. Dyson and G. Laurenczy, *Angew. Chem. Int. Ed.*, 2008, **47**, 3966–3968.

12 N. Lentz and M. Albrecht, *ACS Catal.*, 2022, 12627–12631.

13 Y. Zhang, A. D. MacIntosh, J. L. Wong, E. A. Bielinski, P. G. Williard, B. Q. Mercado, N. Hazari and W. H. Bernskoetter, *Chem. Sci.*, 2015, **6**, 4291–4299.

14 S. Kar, M. Rauch, G. Leitus, Y. Ben-David and D. Milstein, *Nat Catal*, 2021, **4**, 193–201.

15 Z. Wang, S.-M. Lu, J. Li, J. Wang and C. Li, *Chem. Eur. J.*, 2015, **21**, 12592–12595.

16 A. Agapova, E. Alberico, A. Kammer, H. Junge and M. Beller, *ChemCatChem*, 2019, **11**, 1910–1914.

17 N. V. Shvydkiy and D. S. Perekalin, *Coord. Chem. Rev.*, 2020, **411**, 213238.

18 N. Lentz, Y. Streit, P. Knörr and M. Albrecht, *Chem. Eur. J.*, 2022, e202202672.

19 R. H. Morris, *Chem. Rev.*, 2016, **116**, 8588–8654.

20 M. V. Gradiski, B. E. Rennie, A. J. Lough and R. H. Morris, *Dalton Trans.*, 2022, **51**, 11241–11254.

21 Corwin. Hansch, A. Leo and R. W. Taft, *Chem. Rev.*, 1991, **91**, 165–195.

22 Oxford Diffraction, *CrysAlisPro, Version 1.171.40.37a. Oxford Diffraction Ltd., Yarnton, Oxfordshire, UK*, 2018.

23 P. Macchi, H.-B. Bürgi, A. S. Chimpri, J. Hauser and Z. Gál, *J Appl Crystallogr*, 2011, **44**, 763–771.

24 G. M. Sheldrick, *Acta. Crystallogr. A. Found. Adv.*, 2015, **71**, 3–8.

25 G. M. Sheldrick, *Acta. Crystallogr. C. Struct. Chem.*, 2015, **71**, 3–8.

26 O. V. Dolomanov, L. J. Bourhis, R. J. Gildea, J. A. K. Howard and H. Puschmann, *J. Appl. Crystallogr.*, 2009, **42**, 339–341.

CHAPTER IV

Immobilization of iridium triazolylidene complexes into polymer scaffolds and their application in water oxidation

A triazolylidene irdium complex was postmodified with simple methods to introduce two alcohol groups in the triazolylidene backbone. Reaction of this difunctionalized iridium triazolylidene unit with terephthalic acid chloride allowed for integrating these iridium complexes into a polymeric assembly. Both the monomeric complexes as well as the polymerized systems showed activity in water oxidation driven by cerium ammonium nitrate as a chemical oxidant with comparable catalytic performance. Post-reaction analysis of the aqueous reaction solution by ICP MS showed a partial loss of iridium from the polymer into the aqueous phase under catalytic conditions, indicating a need for more robust polymer supports for this type of applications.

IV.1 Introduction

The facile storage of renewably produced energy is a key condition to reduce our dependence on fossil resources, and hence, the development of alternative fuels has attracted great interest in recent years.[1–4] In nature, photosynthesis allows plants to store solar energy in chemical bonds through the splitting of water and formation of energy-rich ATP, which powers the fixation of CO_2 into carbohydrates. Even though the photosynthetic pathways are well understood, the complexity and sophistication of the involved systems prevent a direct translation into artificial devices.[5–9] To conceive artificial photosynthesis, therefore two distinct half reactions need to be managed, consisting of an oxidation to provide electrons and protons, and reduction of a feedstock molecule to generate energy dense fuels such as hydrogen, methanol, or formic acid.[10–13] The oxidative process has been focusing on water oxidation (WOx) and is generally considereded as the more difficult half reaction and thus the limiting factor in developing efficient artificial photosynthesis.[14] The increase of WOx performance requires suitable catalysts that lower the barriers of the electron-transfer and O–O bond formation to enhance overall energy conversion efficiencies. Molecularly defined systems[15,16] based on iridium[17–31] and ruthenium[32–39] complexes have shown particular promise in this field[40–46] with remarkably high turnover frequencies (TOFs) and turnover numbers (TONs).[22,47] While these homogeneous systems stand out with well-defined active sites that allow the activity to be finely tailored, their commercial application is surmised to require electrochemical cells and heterogeneous catalytic systems to keep a close proximity of the catalyst to the electrode surface. Heterogeneization of molecular catalysts can address this aspect by anchoring well-defined complexes to a solid matrix.[48–50] This approach allows to preserve the tailored catalytical activity of the metal center, in contrast to heterogeneous systems with ill-defined active sites where only fractions of the used material are engaged in catalysis.[51]

To heterogeneise homogeneous systems rational ligand design is of most importance.[52,53] The ligands must feature suitable functionalities that allow linkage to either a support matrix or to form solids based on the catalyst itself, which creates a self-supported system.[54] We reasoned that a chelated iridium(III) triazolylidene complex provides a suitable starting point to generate a heterogeneized construct, as this complex family has shown good performance in WOx when the carbene is supported by a chelating donor site.[55] Moreover, the triazole backbone of these carbenes is synthetically easy to access through methods that tolerate a wide range of functional groups,[56–60] thus offering opportunities to tailor the ligand both, for robust iridium binding, and for backbone functionalization.[61] Here we present an iridium NHC complex with a bi-functional ligand that allows for heterogeneizing the iridium-carbene synthon via integration into a polymer with simple techniques. Key for this methodology is the high robustness of the iridium-carbene bond,[62] which enables a series of postmodifications of the complex to form (NHC)iridium-containing polyethylene terephthalate (PET) -derived polyesters for WOx catalysis.

IV.2 Results and discussion

Ligand synthesis started from commercially available methyl 4'-amino-[1,1'-biphenyl]-4-carboxylate which was transformed to the corresponding azide **1** by reaction with t-BuONO and $TMSN_3$ (Scheme 1).[63] Copper-catalyzed alkyne azide cycloaddition with commercial methyl 4-ethynylbenzoate yielded the triazole **2** in 53% overall yield. We used a copper imidazole complex [(iPr)CuCl] with 2,2-bipyridine added in situ to catalyze the cycloaddition as typical simple copper sources only gave marginal conversions of 10–20% compared to 60% with the NHC complex.[64] Methylation with trifluoromethanesulfonate gave the triazolium salt **3** as the ligand precursor. Iridium complex **4** was prepared via a well-established transmetallation procedure[65] with Ag_2O. To this end, ligand precursor **3**, NMe_4Cl and Ag_2O were stirred under exclusion of light to yield the Ag-carbene complex. The solution was then filtered onto a mixture of the iridium precursor and sodium acetate, which facilitated the cyclometallation. Simple purification over a silica column yielded complex **4** as a pure yellow solid in 68% yield. Complex formation was indicated in by a diagnostic HR-MS signal with *m*/*z* = 754.2257 (754.2257 calculated for [**4**−Cl]$^+$). In ^{1}H NMR spectroscopy successful coordination was inferred by the disappearance of the $C_{trz}H$ resonance at δ_H = 10.01 and by the disappearance of an aromatic ligand signal in agreement with cyclometallation. X-ray diffraction analysis of single crystals of **4**, grown by vapour diffusion of Et_2O into a CH_2Cl_2 solution of **4**, unambiguously confirmed the proposed structure (Scheme 1).

Due to the high robustness of the Ir–C_{trz} bond in chelated triazolylidene complexes,[62] a set of post-modifications of the distal ester groups of complex **4** was feasible without any detectable demetallation. Thus, the two methylester groups on either side of the triazolylidene ligand backbone were converted to hydroxyethylesters to introduce two free alcohol functionalities on the complex. Attempts to form the product by direct transesterificaiton from the methylester complex **4** were unsuccessful. Instead, the (bis)carboxylic acid complex **5** was therefore synthesized as an intermediate. To this end, both methylester functionalities were hydrolyzed with aqueous NaOH and extracted with CH_2Cl_2, which provided complex **5** in 85% yield. Successful reaction was indicated by a diagnostic m/z signal at 762.1701 (762.1716 calculated for [**5**−H]$^+$). In the ^{1}H NMR spectrum, the methylester resonances at δ_H = 4.00 and 3.95 disappeared in agreement with ester hydrolysis. Single crystal X-ray diffraction further supported the loss of the methyl groups (Scheme 1b). Complex **6** was subsequently prepared in a second post-modification step by a classic esterification reaction involving the di(acid) iridium complex **5** and ethylene glycol as a solvent and reagent. Heating this mixture in the presence of catalytic amounts of H_2SO_4 followed by column chromatographic purification yielded complex **6** was obtained as an analytically pure yellow solid in 60% yield. Successful modification was indicated by two multiplets in the ^{1}H NMR spectrum in the 4.58–4.41 and 4.02–3.91 ranges, consistent with the introduction of two ethylene glycol esters. Moreover, HR-

MS revealed a m/z signal at 814.2468 (814.2437 calculated for [**6**−Cl]$^+$) and single crystal X-ray diffraction analysis showed the hydroxyethyl tether in the ligand backbone (Scheme 1).

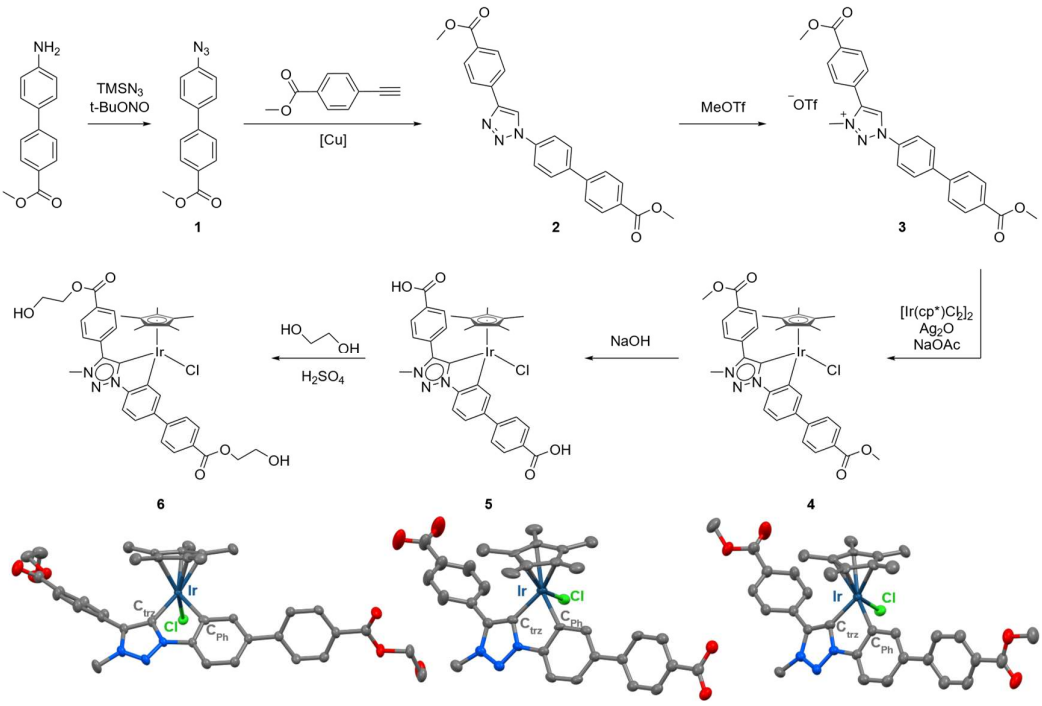

Scheme 1: Synthesis of ligand precursors **1–3** and iridium complexes **4–6**. ORTEP drawings given with 50% probability ellipsoids, hydrogen atoms and cocrystallized solvent molecules (one CH_2Cl_2 in **6**) omitted for clarity.

Single crystal X-ray analysis of the complexes before and after post-modifications indicate that the Cp* iridium carbene core is unaffected by the reactions. All complexes in this series show the classic three-legged piano stool geometry. Both, the Ir–C_{ph} bond (2.060(8) Å) as well as the Ir–C_{trz} bond (2.025(15) Å) are identical within esds in complexes **4–6** (Table 1), demonstrating that the remote ligand modifications have negligible electronic effects on the coordinated metal center. Likewise, the bond angles around iridium do not show any significant differences. Therefore, the remote transformations at the ligand backbone are expected to keep the catalytic activity unaltered with respect to the parent complex.

Table 1: Selected bond lengths [Å] and angles [deg] of complexes **4**–**6**.

	4	5	6
Ir–C_{trz}	2.025(4)	2.037(4)	2.015(6)
Ir–C_{ph}	2.064(4)	2.061(3)	2.057(5)
Ir–Cl	2.419(1)	2.407(1)	2.437(1)
C_{trz}–Ir–C_{ph}	78.5(1)	78.4(1)	77.4(2)
C_{ph}–Ir–Cl	89.4(1)	89.5(1)	89.9(2)
Cl–Ir–C_{trz}	87.1(1)	87.6(1)	89.0(2)

With complex **6** preliminary polymerization studies were carried out to test the stability of the iridium complex in presence of acyl chlorides. A CH_2Cl_2 solution of **6** and terephthaloyl chloride (1:1) was treated with NEt_3 and stirred for an hour at room temperature. The yellow solution was then washed with water and analyzed. ^{1}H NMR spectroscopy showed overall slightly broadened resonances and distinct changes around δ_H = 3.5–4.8, indicating reaction of the ethylenehydroxide groups with acyl chlorides. The aromatic resonances at δ_H = 7.0–8.3 did not shift significantly, suggesting that the iridium complex remained unaltered with persistent ligand coordination. From HR-MS analysis, the formation of oligomeric fragments was inferred from *m*/*z* signals, at 1793.4663 (1793.4680 calculated for the dimer **6**–C(O)–C_6H_4–C(O)–**6** as [M–Cl]$^+$). These results indicate that reaction of **6** with therephthaloyl chloride is feasible under mild conditions and does not lead to noticeable decomposition of the iridium complex.

Since a polymer consisting of just terephthate-bridged complex **6** would feature a very high iridium content, which may induce different WOx mechanisms, the iridium loading of the polymer was lowered by introducing commercially available bis(2-hydroxyethyl)terephthalate as as a co-monomer. This diol has the same functional groups as complex **6** and is therefore assumed to exert the same reactivity towards the terephthaloyl chloride linker. Sufficient dilution of complex **6** with this co-monomer should ensure that each complex forms an isolated mononuclear active catalytic site. Hence, a 1:9 molar mixture of iridium diol **6** and metal-free terephthalate co-monomer in CH_2Cl_2 was reacted with terephthaloyl chloride (10 moleq) in the presence of NEt_3 as a base (Scheme 2). The initial monomer suspension turned immediately to a clear yellow solution upon addition of NEt_3. After 30 s, the solution started to turn turbid, indicating formation of an insoluble fraction. Subsequently, the viscosity increased considerably to the point that magnetic stirring of the reaction mixture became ineffective, indicating the formation of an extensive polymer network. The solid product was filtered off and washed with acetone, water, CH_2Cl_2 and Et_2O to extract all residual monomer and co-monomer, as well as potentially soluble small oligomeric fractions. The product was then dried to yield the polymeric system **7** as a yellow solid. The polymer is insoluble in solvents such as $CDCl_3$, acetone, MeOH,

DMSO, or CH_3CN, that is, solvents which dissolve the iridium monomer complex **6** well. Notably, polymer **7** is slightly soluble in a 1:1 mixture of hexafluoroisopropanol (HFIP) and $CDCl_3$, analogous to polyethylene terephthalate.[66] The ^1H NMR spectrum of **7** in this solvent mixture shows distinct differences to complex **6** (Fig. S 11). In particular, intense signals in the aromatic region around δ_H = 7.9–8.3 correlate well with the aromatic terephthalate linker units. Furthermore, heating the polymer as a DMSO suspension to 100 °C led to considerable swelling and broad aromatic ^1H NMR signals at δ_H = 7.70–8.10 together with a broad resonance at δ_H = 4.6 (Fig. S12), in agreement with extensive polyethylene terephthalate interlinkage. The broadness of the signals may be rationalized by the low solubility and potential coiling of the polymer. Inductively coupled plasma mass spectrometry (ICP-MS) yielded an iridium loading of the polymer of 34 $\mu g_{Ir}/mg_{polymer}$, which equals to 85% of the theoretical loading based on the reaction stoichiometry. Further polymer analysis, for example to identify the polydispersity, was prevented by the very low solubility of polymeric **7**, though the excessive washing with solvents that solubilize the monomeric components indicates that **7** is composed of polymeric material only.

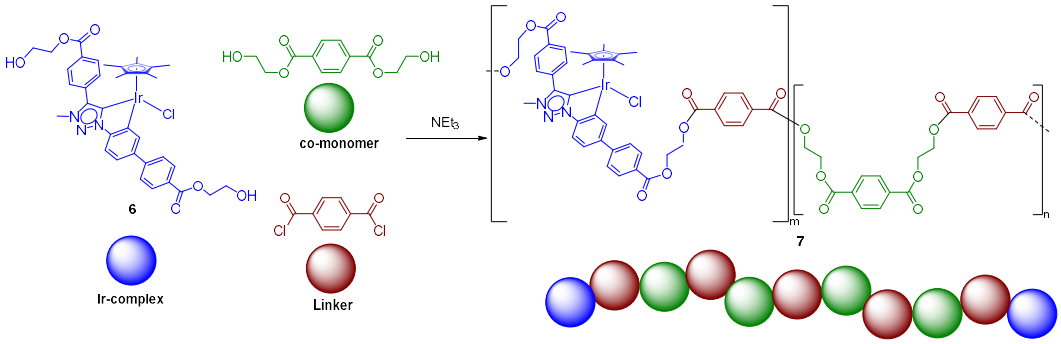

Scheme 2: Polymerization of iridium complex **6** with bis(2-hydroxyethyl)terephthalate as co-monomer, and terephthaloyl chloride as linker. Reaction conditions: **6** (30.0 mg, 35.3 µmol), terephthaloyl chloride (78.9 mg, 389 µmol), bis(2-hydroxyethyl)terephthalate (89.8 mg, 353 µmol) and NEt_3 (0.45 mL, 3.2 mmol) in CH_2Cl_2 (2.5 mL).

The single-site molecular complexes **4** and **6**, and the polymerized variant **7** were tested as WOx catalysts. WOx catalysis with iridium triazolylidene complexes has been established previously and these complexes are usually stable and active for a long time,[55] making this reaction well-suited for studying recyclability of the polymer. Cerium ammonium nitrate (CAN) was used a sacrificial one-electron oxidant, which is unable to catalyze the formation of dioxygen on its own.[67] As complex **4** is essentially insoluble in H_2O, a stock solution in CH_3CN was evaporated before adding H_2O and CAN. Catalytic runs were performed with a 1:8,000 Ir/CAN ratio and conversion was measured via the volume of the evolved gas using a BlueV count volumetric gas counter (Figure 1). After CAN addition (as a solution in 1 M HNO_3), a

considerable induction time of about 1 h was observed before gas evolution started. This long induction time has been attributed predominantly to the insolubility of **4** and, to a lesser extent, to the catalyst precursor activation as often observed with iridium WOx catalysts.[55] This activation is well-documented for Ir(Cp*)-based systems and involves replacement of the ancillary chloride ligand, oxidation of the iridium(III) center, and (partial) oxidation of the Cp* moiety.[68–71] Ancillary chelating ligands are usually retained during this process.[70] With complex **4** up to 860 turnovers were reached before the reaction stopped, which equals to about 45% of the theoretical limit for oxygen production. A maximal turnover frequency TOF_{max} = 180 h^{-1} was noted after the induction period, which is within the range of many other homogeneous Ir(Cp*) catalysts for this reaction, yet well below some of the most active systems currently known (TOF_{max} 6,000–18,000 h^{-1}).[72,73]

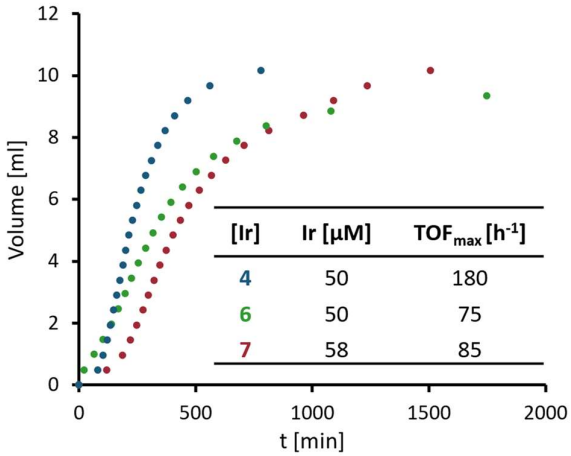

Figure 1: Time-dependent gas evolution profiles for WOx with Ir complexes **4** and **6**, and with Ir-containing polymer **7**. Reaction conditions: 8,000:1 CAN/Ir ratio (0.4 M CAN in 1 M HNO_3), 50µM [**Ir**], 10 mL solvent volume.

Complex **6** was assessed under similar conditions but with additional 19 eq of bis(2-hydroxyethyl)terephthalate to mimic the presence of polymeric linkers present in **7**. The catalytic performance of **6** was diminished compared to complex **4** and TOF_{max} dropped from 180 to 75 h^{-1}. The TONs were, however, not severely affected (TON_{max} = 790) with only 10% disparity when compared to **4**. These results suggest that the presence of the terephthalate linker fragments does not influence the catalyst in a way that would lead to major decomposition. At the end of the catalytic run, the reaction solution was filtered over a glass fiber filter and the filter washed with 1 M HNO_3. When analyzed by ICP-MS, the filtrate was comprised of 79±9 µg iridium. This amount equals to ca 80% of the initially added iridium and indicates that this quantity was present either as homogeneous complex or as soluble

decomposition products. The residual 20% iridium may either be unactivated and hence insoluble complex **6** or insoluble iridium oxide decomposition products. When using the residue from the reaction flask and filter in a second catalytic run, some activity persisted. Gas evolution was considerably slower, which is expected as the iridium loading was significantly decreased. However taking the actual 20% loading into account, the TOF_{max} remained at approximately 85 h^{-1} and TON_{max} increased to 1400. While these values need to be used with caution as the quantity of iridium was very small and errors accordingly are very large, they suggest that either the reused iridium was still bound to the chelating ligand or that the iridium oxide is an active heterogeneous catalyst. Filtration of the solution after the second run followed by ICP-MS analysis indicated that all iridium was solubilized, which does not support the formation of a heterogeneous iridium oxide layer as active catalyst. In agreement with such a model based on complex solubility as limiting factor, a catalytic run starting with only 80% catalyst loading (40 µM instead of 50 µM) afforded identical turnover frequencies and slightly lower TONs (ca. 720). Notably, a recyclying experiment as described above did not show any more gas production and no residual catalytic activity, indicating that at these concentrations, all catalyst was soluble in the first run.

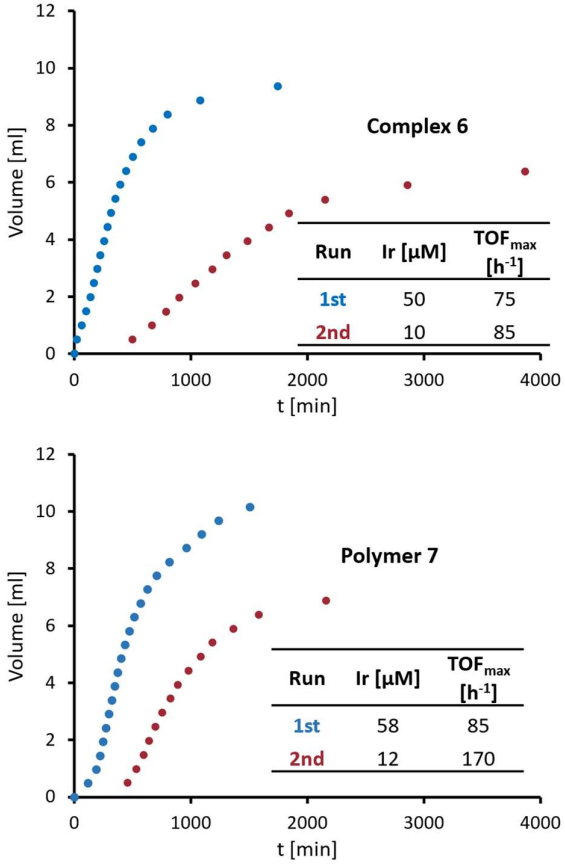

Figure 2: Recycling experiments for WOx catalysis with complex **6** and polymer **7.** For both catalyst precursors time dependent gas evolution profiles are shown corresponding to inital runs (1st) and after

recycling the catalyst (2nd). Reaction conditions: 8,000:1 CAN/Ir ratio (0.4 M CAN (10 mL) in 1 M HNO_3), 50 µM **[Ir]**. After inital runs solids were filtered off, rinsed with 1 M HNO_3 and reused for the indicated 2nd runs.

Under similar conditions polymer **7** showed comparable performance to **6** with $TOF_{max} \approx 85\ h^{-1}$, though the induction time was twice as long. Once gas evolution stopped, the polymer was reused according to the same procedure as applied for complex **6**, that is, separation of the solids from the solution via a glass fiber filter. ICP-MS analysis of the solution showed a total of 86±10 µg iridum in solution (ca. 80% of initial loading). The concentration of iridium in solution is comparable to complex **6** and suggests that only about 20% of iridium is still immobilized in the insoluble polymer after the first cycle. Performing a second run with this 20% retained iridium fraction from the polymer showed increased catalytic activity ($TOF_{max} \approx 170\ h^{-1}$). ICP-MS of the filtrate after this second run revealed close to 25% of initial iridium loading, indicating that all residual iridium was solubilized at this stage. This behavior of polymer **7** is essentially identical to that of the monomeric molecular complex **6**, suggesting that (i) embedding of the catalytically active site into the polyethylene terephthalate structure has no negative impact on catalyst performance, and (ii) that the catalytically active species may be similar or identical both in initial runs and after recycling in the second runs. This similarity and the solubilization of the polymer-immobilized iridium within two runs further indicates that the polymeric backbone is unstable under catalytic conditions. Alternatively, catalyst activation may involve loss of the *N,C*-bidentate chelating phenyl-triazolylidene ligand from the iridium center and leaching of iridium into the solution. Reactions at lower iridium concentrations (*vide supra*) support, however, the former pathway and are not consistent with ligand loss.

The polymer-supported iridium catalyst therefore appears to depolymerize and release oligomeric or even monomeric iridium complexes similar to **6** into the reaction mixture. This reactivity may be due to the relatively harsh conditions when WOx is driven by CAN as the sacrificial oxidant. WOx with different driving forces such as $NaIO_4$ as sacrificial oxidant, or electrocatalytic WOx may change the activity,[55] and thus highlight the potential of this simple heterogeneization methodology.

IV.3 Conclusions

We have demonstrated that the synthetic versatility of triazole-derived “click”-carbenes offers straightforward methodologies to embed triazolylidene metal complexes into polymeric structures as a viable strategy for the immobilization of homogeneous catalysts. The extraordinary stability of triazolylidene iridium complexes allowed for a range of post-functionalizations of the complexes, including base-mediated hydrolysis and acid-catalyzed esterification reactions to access iridium-carbene systems integrated into polyester materials. These iridium polymers catalyze the CAN-driven water oxidation, though recycling experiments show identical behavior as monomeric analogues, which suggests a breakdown of the polymeric structure under catalytic conditions. Based on these results, it may be beneficial to embed the active sites into more robust polymer structures, or to perform the water oxidation in an electrocatalytic set-up for remediating such polymer breakdown and for improving the recyclability of the polymeric iridium system.

IV.4 Experimental

All reagents were commercially available and used as received unless specified. NMR spectra were recorded at 25 °C on Bruker spectrometers operating at 300 or 400 MHz (^{1}H NMR) and 75 or 100 MHz (^{13}C{^{1}H} NMR), respectively. Chemical shifts (δ in ppm, coupling constants *J* in Hz) were referenced to residual solvent signals (^{1}H,^{13}C). Assignments are based on homo- and hetero nuclear shift correlation spectroscopy. High resolution mass spectrometry was carried out by the DCBP mass spectrometry group at the University of Bern with with a Thermo Scientific LTQ Orbitrap XL (ESI-TOF). Elemental analyses were performed on a Thermo Scientific Flash 2000 CHNS-O elemental analyzer by the DCBP Microanalytic Laboratory. ICP measurements were carried out by the group of Prof. Dr. Peter Broekmann at the university of Bern on an Perkin Elmer NexION 2000.

Synthesis of azide 1.

Methyl-4'-amino-(1,1'-biphenyl)-4-carboxylate (800.00 mg, 3.52 mmol) was suspended in CH_3CN (30 mL) and cooled to 0 °C. t-Butyl nitrite (545.0 mg, 5.28 mmol) and subsequently azidotrimethylsilane (487.0 mg, 4.22 mmol) were added dropwise and the mixture was stirred for 24 h at r.t. All volatiles were removed under reduced pressure. The resulting solid was dissolved in ethyl acetate (100 mL) and washed with water (2 × 100 mL). The organic phase was dried over Na_2SO_4 and all volatiles were removed under reduced pressure yielding **1** as a light brown solid (813 mg, 91%). ^{1}H NMR (400 MHz, $CDCl_3$) δ 8.20–8.06 (m, 2H, CH_{Ph}), 7.66–7.58 (m, 4H, CH_{Ph}), 7.16–7.08 (m, 2H, CH_{Ph}), 3.94 (s, 3H, CH_3). ^{13}C{^{1}H} NMR (101 MHz, $CDCl_3$) δ 167.05 (*C*$OOCH_3$), 144.65, 140.29, 136.86, 130.36, 129.15, 128.78, 126.87, 119.71 (8 × $C_{Ph}H$, 4 × C_{Ph}), 52.29 (CH_3). HR-MS (m/z): Calculated for $[M+H]^+$ =254.0924; found: 254.0922.

Synthesis of triazole 2.

Compound **1** (100 mg, 0.40 mmol), methyl-4-ethynylbenzoate (63 mg, 0.40 mmol) 2,2-bipyridine (4 mg, 0.02 mmol) and [(iPr)CuCl] (10 mg, 0.02 mmol) were dried under vacuum and suspended in dry CH_3CN (10 mL). The mixture was stirred at room temperature for 20 h. All solids were filtered of and washed with CH_3CN (10 mL) and CH_2Cl_2 (10 mL). The solids were dried under vacuum yielding triazole **2** as a light brown solid (100 mg, 61%). ^{1}H NMR (400 MHz, $CDCl_3$) δ 8.33 (s, 1H, H_{trz}), 8.21–7.53 (m, 12H, H_{Ph}), 3.96 (s, 3H, OCH_3), 3.96 (s, 3H, OCH_3). HR-MS (m/z): Calculated for $[M+H]^+$ = 414.1448; found: 414.1439.

Synthesis of triazolium salt 3.

Triazole **2** (100 mg, 0.24 mmol) was placed in a microwave vial and suspended in CH_2Cl_2 (6 mL). MeOTf (30 µL, 0.27 mmol) was added. The mixture was heated to 80°C and stirred for 1.5 h. MeOH (1 mL) was added and the mixture was stirred for 1 h at room temperature. The mixture was concentrated under reduced pressure. Et_2O was then added until the product

precipitated, yielding compound **3** (130 mg, 93%) as a white solid. ^{1}H NMR (400 MHz, DMSO-d_6) δ 10.01 (s, 1H, $C_{trz}H$), 8.38–7.94 (m, 12H, $C_{Ph}H$), 4.48 (s, 3H, NCH_3), 3.94 (s, 3H, OCH_3), 3.90 (s, 3H, OCH_3). $^{13}C\{^{1}H\}$ NMR (101 MHz, DMSO) δ 165.93, 165.45 (2× COOMe), 142.45, 142.25, 141.99, 134.46, 132.25, 130.06, 129.98, 129.89, 129.52, 129.03, 127.89, 127.44, 126.84, 122.28, 121.87 (12 × C_{Ph}, 2 × C_{trz}, 1 × C), 52.68, 52.32 (2 × OCH_3), 38.5 (NCH_3). HR-MS (m/z): Calculated for $C_{25}H_{22}O_4N_3$[M-OTf]$^+$ = 428.1581; found: 428.1589. Anal. Calcd for $C_{25}H_{22}F_3N_3O_7S$ (577.53): C 54.07; H 3.84; N 7.28; S, 5.55 Found: C 54.36; H 3.91; N 7.17; S 5.53

Synthesis of complex 4.

Compound **2** (150.0 mg, 0.26 mmol), tetramethylammonium chloride (43.0 mg, 0.39 mmol) and Ag_2O (181.0 mg, 0.78 mmol) were placed in a schlenk flask and dried under vacuum. CH_2Cl_2 (10 mL) was added and the mixture was stirred for 48 h at r.t under exclusion of light. The mixture was filtered over Celite onto a mixture of $[Ir(Cp^*)Cl_2]_2$ (103.0 mg, 0.13 mmol) and sodium acetate (64.0 mg, 0.78 mmol) and stirred for 2 h. The mixture was filtered over Celite and all volatiles were removed under reduced pressure. The crude product was submitted to column chromatography (SiO_2; 2 × CH_2Cl_2/MeOH 1000:4). All volatiles were removed under reduced pressure. The resulting solid was washed with pentane (3 × 10 mL), yielding complex **3** (140 mg, 68%) as a yellow solid. ^{1}H NMR (400 MHz, $CDCl_3$) δ 8.26–8.20 (m, 2H, CH_{Ph}), 8.14–8.08 (m, 3H, CH_{Ph}), 7.98–7.91 (m, 2H, CH_{Ph}), 7.79–7.70 (m, 3H, CH_{Ph}), 7.31 (dd, *J* = 8.2, 1.9 Hz, 1H, CH_{Ph}), 4.14 (s, 3H, CH_3), 4.00 (s, 3H, CH_3), 3.95 (s, 3H, CH_3), 1.53 (s, 15H, Cp–CH_3). $^{13}C\{^{1}H\}$ NMR (101 MHz, $CDCl_3$) δ 167.36, 166.582 (2 × COOH), 151.51 (C_{trz}Ir), 146.75, 145.54, 145.17, 143.07, 140.22 (5 × C_q), 136.61, 132.68, 131.36, 130.86, 130.29, 130.08, 128.55, 127.41, 121.89, 112.54 (7 × C_{Ph}, 2 × C_q), 90.22 (C_q), 52.63, 52.19 (2 × OCH_3), 37.50 (NCH_3), 9.49 (Cp–CH_3). Anal. Calcd for $C_{35}H_{35}ClIrN_3O_4$: C 53.26; H 4.47; N 5.32; Found: C 53.27; H 4.42; N 5.25. HR-MS (m/z): Calculated for [M-Cl]$^+$ = 754.2257; found: 754.2257.

Synthesis of complex 5.

Complex **3** (130 mg, 0.16 mmol) was dissolved in acetone (100 mL). An NaOH solution (2 M in H_2O, 28 mL) was added and the mixture was stirred for 2h at 35°C. The mixture was concentrated under reduced pressure and washed with CH_2Cl_2 (1 × 50 mL). The aqueous phase was acidified with HCl (1 M) and extracted with EtOAc (100 mL). The organic phase was dried over Na_2SO_4 and evaporated to dryness. The crude product was washed twice with Et_2O yielding complex **4** (105 mg, 84%) as a yellow solid. ^{1}H NMR (400 MHz, acetone-d_6) δ 8.29–8.23 (m, 2H, CH_{Ar}), 8.20–8.12 (m, 5H, CH_{Ar}), 7.91–7.85 (m, 2H, CH_{Ar}), 7.74 (m, 1H, CH_{Ar}), 7.40 (dd, *J* = 8.1, 2.0 Hz, 1H, CH_{Ar}), 4.34 (s, 3H, NCH_3), 1.54 (s, 15H, Cp–CH_3). $^{13}C\{^{1}H\}$ NMR (101 MHz, acetone–d_6) δ 167.58, 167.22, 152.25, 147.21, 146.45, 143.94, 140.12, 137.67, 133.87, 132.32, 131.88, 131.08, 130.77, 129.88, 127.93, 122.07, 114.11, 90.39, 38.21 (NCH_3), 9.46 (Cp–CH_3). HR-MS (m/z): Calculated for [M+H]$^+$ = 762.1716; found: 762.1701.

Synthesis of complex 6.

5 (100.0 mg, 131.3 µmol) was placed in a Schlenk flask under nitrogen atmosphere. Ethylene glycol (11 mL, large excess) and H_2SO_4 (0.1 mL) were added and the mixture heated to 100 °C for 3 h. Completion of the reaction was indicated by full dissolution of previously suspended complex. The crude mixture was diluted with water (100 mL) and extracted with EtOAc (2 × 50 mL). The organic phase was washed once with aquaeous sat. Na_2CO_3 solution (20 mL), dried over $MgSO_4$ and evaporated to dryness under reduced pressure. The crude was submitted to gradient column chromatography (SiO_2; CH_2Cl_2/MeOH from 100:0 to 100:1.5). All volatiles were removed under reduced pressure and the resulting solid was dissolved in a minimal amount of CH_2Cl_2 and precipitated by addition of Et_2O. Precipitation was repeated from acetone solution. The solid was washed with Et_2O (3 × 20 mL) to yield complex **6** as a yellow powder (68 mg, 60%). ^{1}H NMR (400 MHz, CD_2Cl_2) δ 8.29–8.22 (m, 2H, CH_{ph}), 8.17–8.08 (m, 3H, CH_{ph}), 7.98–7.93 (m, 2H, CH_{ph}), 7.84–7.73 (m, 3H, CH_{ph}), 7.36 (dd, *J* = 8.2, 2.0 Hz, 1H, CH_{ph}), 4.58–4.41 (m, 4H, $COOCH_2$), 4.16 (s, 3H, trz-CH_3), 4.02–3.91 (m, 4H, C*H*$_2$OH), 2.07–1.97 (m, 2H, OH), 1.52 (s, 15H, Cp–CH_3). ^{13}C NMR (101 MHz, CD_2Cl_2) δ 167.09, 166.55(2 × COOEtOH), 151.97 (C_{trz}Ir), 146.95, 146.44, 143.32, 140.14, 138.05 (5 × C_q), 136.92, 133.18, 131.48, 131.14, 130.49, 130.37, 127.66, 121.93, 114.04 (7 × C_{Ph}, 2 × C_q), 91.10 (C_q), 67.44, 67.08, 61.73, 61.58 (4 × CH_2), 37.96 (NCH_3), 9.48 (Cp–*C*H_3). HR-MS (m/z): Calculated for $[M\text{-}Cl]^+$ = 814.2437; found: 814.2468. Anal. Calcd for $C_{37}H_{41}ClIrN_3O_6$: C 52.32; H 4.63; N 4.95; Found: C 52.33; H 4.42; N 4.62.

Synthesis of polymer 7

The reaction was carried out under dry conditions with anhydrous NEt_3 and CH_2Cl_2 dried on a solvent purification system. Complex **6** (30.0 mg, 35.3 µmol), terephthaloyl chloride (78.9 mg, 389 µmol), bis(2-hydroxyethyl)terephthalate (89.8 mg, 353 µmol) and NEt_3 (0.45 mL, 3.2 mmol) were mixed in CH_2Cl_2 (2.5 mL), producing an intense yellow solution. The solution was incubated at room temperature for 3 days (due to formation of solids, stirring stopped after several minutes). The formed solids were filtered off and washed with acetone, H_2O, CH_3CN CH_2Cl_2 and Et_2O. The product was dried under vacuum to yield a yellow waxy solid (121 mg, 71%).

To determine the Ir content, polymer **7** was decomposed by heating a sample suspended in 60% HNO_3 at 80 °C for 2 days. After this treatment, the suspended solids lost their originally yellow color, and the mixture appeared as a colorless suspension containing white solids. The mixture was filtered over a glass filter, diluted with water and subjected to ICP-MS.

Typical catalytic procedure water oxidation.

Complex **4** (395 µg, 0.5 µmol) was added to a 25 mL two neck round-bottom flask as a CH_3CN solution and evaporated to dryness. One neck was closed with a septum, the other connected to a BlueVCount volumetric gas counter. The gas counter automatically normalizes the measured volume for pressure, humidity and temperature. A CAN solution (0.4 M in 1 M aqueous HNO_3, 10 mL) was added and the solution was stirred at room temperature until gas formation ceased according to the BlueVCount measurements.

ICP-MS measurements after catalytic runs

The reaction mixture was filtered and the glassware and filter washed with HNO_3. The combined aqueous layers were weighted and submitted to ICP analysis which determined the iridium content in µg per g sample. Based on this data the total of leached iridium was calculated and compared to the initial catalytic loading to determine the amount of non-dissolved iridium.

Crystal-Structure Determination.

Crystals of **4,5** and **6** were immersed in parabar oil, mounted at ambient conditions and transferred into the stream of nitrogen (173 K). The measurements of **4** and **5** were made on a *RIGAKU Synergy S* area-detector diffractometer[74] using mirror optics monochromated Cu *K*α radiation (λ = 1.54184 Å). The measurement of **6** was made on a *Oxford Diffraction SuperNova* area-detector diffractometer[75] using mirror optics monochromated Mo *K*α radiation (λ = 0.71073 Å) and Al filtered.[76] Data reduction was performed using the *CrysAlisPro*[75] program. The intensities were corrected for Lorentz and polarization effects, and an absorption correction based on the multi-scan method using SCALE3 ABSPACK in *CrysAlisPro*[75] was applied. The structures were solved by intrinsic phasing using *SHELXT*[77], which revealed the positions of all non-hydrogen atoms. All atoms were refined anisotropically and H-atoms were assigned in geometrically calculated positions and refined using a riding model where each H-atom was assigned a fixed isotropic displacement parameter with a value equal to 1.2Ueq of its parent atom (1.5Ueq for methyl groups). For **4**, one methylester group is conformationally disordered about two sites. About 9% of the unit cell volume is filled by heavily disordered co-crystallized solvent molecules. For **5** the Cp* ligand is conformationally disordered about two sites. Its atomic displacement parameters were restrained using the SHELX SIMU and RIGU instructions. About 27% of the unit cell volume is filled by heavily disordered co-crystallized solvent molecules. Electron density of disordered solvent molecules was accounted for by the SQUEEZE procedure of PLATON.[78] Refinement of the structures were carried out on F^2 using full-matrix least-squares procedures, which minimized the function $\Sigma w(F_o^2 - F_c^2)^2$. The weighting scheme was based on counting statistics and included a factor to downweight the intense reflections. All calculations were performed using the *SHELXL-2014/7*[79] program in OLEX2.[80] Further crystallographic details are compiled in Tables S2–3.

Table 2. Crystal data and structure refinement for **4 and 5.**

Identification code	**4**	**5**
CCDC Nr.	2258617	2258618
Empirical formula	$C_{35}H_{35}ClIrN_3O_4$	$C_{33}H_{31}ClIrN_3O_4$
Formula weight	789.31	761.26
Temperature/K	173.01(10)	99.99(10)
Crystal system	monoclinic	triclinic
Space group	$P2_1/c$	P-1
a/Å	11.84972(6)	8.21061(12)
b/Å	23.19094(14)	14.6707(2)
c/Å	25.53781(14)	15.9100(3)
α/°	90	92.0040(12)
β/°	94.0937(5)	93.7670(13)
γ/°	90	90.9040(12)
Volume/Å^3	7000.04(7)	1910.82(5)
Z	8	2
ρ_{calc}g/cm^3	1.498	1.323
μ/mm^{-1}	8.405	7.679
F(000)	3136.0	752.0
Crystal size/mm^3	0.13 × 0.025 × 0.022	0.166 × 0.078 × 0.045
Radiation	CuKα (λ = 1.54184)	CuKα (λ = 1.54184)
2Θ range for data collection/°	5.154 to 154.68	5.57 to 154.15
Index ranges	-13 ≤ h ≤ 14, -29 ≤ k ≤ 28, -32 ≤ l ≤ 32	-8 ≤ h ≤ 10, -18 ≤ k ≤ 18, -19 ≤ l ≤ 20
Reflections collected	109076	35916
Independent reflections	14500 [R_{int} = 0.0598, R_{sigma} = 0.0302]	7812 [R_{int} = 0.0753, R_{sigma} = 0.0440]
Data/restraints/parameters	14500/96/838	7812/530/485
Goodness-of-fit on F^2	1.058	1.100
Final R indexes [I>=2σ (I)]	R_1 = 0.0343, wR_2 = 0.0823	R_1 = 0.0423, wR_2 = 0.1156
Final R indexes [all data]	R_1 = 0.0389, wR_2 = 0.0843	R_1 = 0.0447, wR_2 = 0.1175
Largest diff. peak/hole / e Å^{-3}	2.29/-0.97	2.47/-2.43

Table 3. Crystal data and structure refinement for **2a** and **2a-H]$^+$**

.

Identification code	**6**
Empirical formula	2258619
Formula weight	$C_{38}H_{41}Cl_3IrN_3O_6$
Temperature/K	934.29
Crystal system	173.00(10)
Space group	triclinic
a/Å	*P*-1
b/Å	9.22160(10)
c/Å	11.05400(10)
α/°	19.2795(2)
β/°	103.1020(10)
γ/°	100.0200(10)
Volume/Å^3	94.8980(10)
Z	1868.88(3)
ρ_{calc}g/cm^3	2
μ/mm^{-1}	1.660
F(000)	3.837
Crystal size/mm^3	932.0
Radiation	0.182 × 0.148 × 0.024
2Θ range for data collection/°	Mo Kα (λ = 0.71073)
Index ranges	3.816 to 63.826
Reflections collected	-13 ≤ h ≤ 13, -16 ≤ k ≤ 16, -28 ≤ l ≤ 28
Independent reflections	24822
Data/restraints/parameters	24822 [R_{int} = ?, R_{sigma} = 0.0716]
Goodness-of-fit on F^2	24822/0/469
Final R indexes [I>=2σ (I)]	1.079
Final R indexes [all data]	R_1 = 0.0459, wR_2 = 0.1279
Largest diff. peak/hole / e Å^{-3}	R_1 = 0.0657, wR_2 = 0.1308

IV.5 References

1 C. Liu, F. Li, L.-P. Ma and H.-M. Cheng, *Adv. Mater.*, 2010, **22**, E28–E62.

2 S. van Renssen, *Nat. Clim. Chang.*, 2020, **10**, 799–801.

3 N. Armaroli and V. Balzani, *Energy Environ. Sci.*, 2011, **4**, 3193.

4 N. Armaroli and V. Balzani, *Angew. Chem. Int. Ed.*, 2007, **46**, 52–66.

5 S. Y. Reece, J. A. Hamel, K. Sung, T. D. Jarvi, A. J. Esswein, J. J. H. Pijpers and D. G. Nocera, *Science*, 2011, **334**, 645–648.

6 S. Berardi, S. Drouet, L. Francàs, C. Gimbert-Suriñach, M. Guttentag, C. Richmond, T. Stoll and A. Llobet, *Chem. Soc. Rev.*, 2014, **43**, 7501–7519.

7 J. J. Concepcion, R. L. House, J. M. Papanikolas and T. J. Meyer, *Proc. Natl. Acad. Sci. U.S.A.*, 2012, **109**, 15560–15564.

8 D. Gust, T. A. Moore and A. L. Moore, *Acc. Chem. Res.*, 2009, **42**, 1890–1898.

9 M. D. Kärkäs, E. V. Johnston, O. Verho and B. Åkermark, *Acc. Chem. Res.*, 2014, **47**, 100–111.

10 C. Herrero, A. Quaranta, W. Leibl, A. W. Rutherford and A. Aukauloo, *Energy Environ. Sci.*, 2011, **4**, 2353.

11 N. S. Lewis and D. G. Nocera, *Proc. Natl. Acad. Sci. U.S.A.*, 2006, **103**, 15729–15735.

12 N. D. McDaniel and S. Bernhard, *Dalton Trans.*, 2010, **39**, 10021.

13 C. G. Morales-Guio, L.-A. Stern and X. Hu, *Chem. Soc. Rev.*, 2014, **43**, 6555.

14 J. K. Hurst, *Science*, 2010, **328**, 315–316.

15 A. Llobet, Ed., *Molecular water oxidation catalysis: a key topic for new sustainable energy conversion schemes*, John Wiley & Sons, Inc, Chichester, West Sussex, 2014.

16 N. Vereshchuk, M. Gil-Sepulcre, A. Ghaderian, J. Holub, C. Gimbert-Suriñach and A. Llobet, *Chem. Soc. Rev.*, 2023, **52**, 196–211.

17 N. D. McDaniel, F. J. Coughlin, L. L. Tinker and S. Bernhard, *J. Am. Chem. Soc.*, 2008, **130**, 210–217.

18 J. F. Hull, D. Balcells, J. D. Blakemore, C. D. Incarvito, O. Eisenstein, G. W. Brudvig and R. H. Crabtree, *J. Am. Chem. Soc.*, 2009, **131**, 8730–8731.

19 J. D. Blakemore, N. D. Schley, D. Balcells, J. F. Hull, G. W. Olack, C. D. Incarvito, O. Eisenstein, G. W. Brudvig and R. H. Crabtree, *J. Am. Chem. Soc.*, 2010, **132**, 16017–16029.

20 R. Lalrempuia, N. D. McDaniel, H. Müller-Bunz, S. Bernhard and M. Albrecht, *Angew. Chem. Int. Ed.*, 2010, **49**, 9765–9768.

21 N. D. Schley, J. D. Blakemore, N. K. Subbaiyan, C. D. Incarvito, F. D'Souza, R. H. Crabtree and G. W. Brudvig, *J. Am. Chem. Soc.*, 2011, **133**, 10473–10481.

22 Z. Codolà, J. M. S. Cardoso, B. Royo, M. Costas and J. Lloret-Fillol, *Chem. Eur. J.*, 2013, **19**, 7203–7213.

23 O. Diaz-Morales, T. J. P. Hersbach, D. G. H. Hetterscheid, J. N. H. Reek and M. T. M. Koper, *J. Am. Chem. Soc.*, 2014, **136**, 10432–10439.

24 A. Petronilho, J. A. Woods, S. Bernhard and M. Albrecht, *Eur. J. Inorg. Chem.*, 2014, **2014**, 708–714.

25 M. Li, K. Takada, J. I. Goldsmith and S. Bernhard, *Inorg. Chem.*, 2016, **55**, 518–526.

26 M. Navarro, M. Li, H. Müller-Bunz, S. Bernhard and M. Albrecht, *Chem. Eur. J.*, 2016, **22**, 6740–6745.

27 G. Menendez Rodriguez, A. Bucci, R. Hutchinson, G. Bellachioma, C. Zuccaccia, S. Giovagnoli, H. Idriss and A. Macchioni, *ACS Energy Lett.*, 2017, **2**, 105–110.

28 G. Menendez Rodriguez, G. Gatto, C. Zuccaccia and A. Macchioni, *ChemSusChem*, 2017, **10**, 4503–4509.

29 R. Puerta-Oteo, M. V. Jiménez and J. J. Pérez-Torrente, *Catal. Sci. Technol.*, 2019, **9**, 1437–1450.

30 Z. Mazloomi, J. Margalef, M. Gil-Sepulcre, N. Romero, M. Albrecht, A. Llobet, X. Sala, O. Pàmies and M. Diéguez, *Inorg. Chem.*, 2020, **59**, 12337–12347.

31 G. Gatto, A. De Palo, A. C. Carrasco, A. M. Pizarro, S. Zacchini, G. Pampaloni, F. Marchetti and A. Macchioni, *Catal. Sci. Technol.*, 2021, **11**, 2885–2895.

32 S. W. Gersten, G. J. Samuels and T. J. Meyer, *J. Am. Chem. Soc.*, 1982, **104**, 4029–4030.

33 C. Sens, I. Romero, M. Rodríguez, A. Llobet, T. Parella and J. Benet-Buchholz, *J. Am. Chem. Soc.*, 2004, **126**, 7798–7799.

34 R. Zong and R. P. Thummel, *J. Am. Chem. Soc.*, 2005, **127**, 12802–12803.

35 S.-X. Guo, C.-Y. Lee, J. Zhang, A. M. Bond, Y. V. Geletii and C. L. Hill, *Inorg. Chem.*, 2014, **53**, 7561–7570.

36 R. Matheu, L. Francàs, P. Chernev, M. Z. Ertem, V. Batista, M. Haumann, X. Sala and A. Llobet, *ACS Catal.*, 2015, **5**, 3422–3429.

37 B. Limburg, E. Bouwman and S. Bonnet, *ACS Catal.*, 2016, **6**, 5273–5284.

38 L. Tong and R. P. Thummel, *Chem. Sci.*, 2016, **7**, 6591–6603.

39 T. Liu, S. Zhan, N. Shen, L. Wang, Z. Szabó, H. Yang, M. S. G. Ahlquist and L. Sun, *J. Am. Chem. Soc.*, 2023, jacs.3c03415.

40 W. C. Ellis, N. D. McDaniel, S. Bernhard and T. J. Collins, *J. Am. Chem. Soc.*, 2010, **132**, 10990–10991.

41 J. L. Fillol, Z. Codolà, I. Garcia-Bosch, L. Gómez, J. J. Pla and M. Costas, *Nature Chem*, 2011, **3**, 807–813.

42 M. Wiechen, H.-M. Berends and P. Kurz, *Dalton Trans.*, 2012, **41**, 21–31.

43 H. Lv, J. Song, Y. V. Geletii, J. W. Vickers, J. M. Sumliner, D. G. Musaev, P. Kögerler, P. F. Zhuk, J. Bacsa, G. Zhu and C. L. Hill, *J. Am. Chem. Soc.*, 2014, **136**, 9268–9271.

44 F. Song, R. Moré, M. Schilling, G. Smolentsev, N. Azzaroli, T. Fox, S. Luber and G. R. Patzke, *J. Am. Chem. Soc.*, 2017, **139**, 14198–14208.

45 M. Natali, I. Bazzan, S. Goberna-Ferrón, R. Al-Oweini, M. Ibrahim, B. S. Bassil, H. Dau, F. Scandola, J. R. Galán-Mascarós, U. Kortz, A. Sartorel, I. Zaharieva and M. Bonchio, *Green Chem.*, 2017, **19**, 2416–2426.

46 M. Gil-Sepulcre and A. Llobet, *Nat Catal*, 2022, **5**, 79–82.

47 L. Duan, F. Bozoglian, S. Mandal, B. Stewart, T. Privalov, A. Llobet and L. Sun, *Nature Chem*, 2012, **4**, 418–423.

48 C. Wang, J.-L. Wang and W. Lin, *J. Am. Chem. Soc.*, 2012, **134**, 19895–19908.

49 R. Matheu, I. A. Moreno-Hernandez, X. Sala, H. B. Gray, B. S. Brunschwig, A. Llobet and N. S. Lewis, *J. Am. Chem. Soc.*, 2017, **139**, 11345–11348.

50 J. Odrobina, J. Scholz, A. Pannwitz, L. Francàs, S. Dechert, A. Llobet, C. Jooss and F. Meyer, *ACS Catal.*, 2017, **7**, 2116–2125.

51 A. Macchioni, *Eur. J. Inorg. Chem.*, 2019, **2019**, 7–17.

52 F. Carson, E. Martínez-Castro, R. Marcos, G. G. Miera, K. Jansson, X. Zou and B. Martín-Matute, *Chem. Commun.*, 2015, **51**, 10864–10867.

53 R. Zhong, A. C. Lindhorst, F. J. Groche and F. E. Kühn, *Chem. Rev.*, 2017, **117**, 1970–2058.

54 D. Wang, S. L. Marquard, L. Troian-Gautier, M. V. Sheridan, B. D. Sherman, Y. Wang, M. S. Eberhart, B. H. Farnum, C. J. Dares and T. J. Meyer, *J. Am. Chem. Soc.*, 2018, **140**, 719–726.

55 M. Olivares, C. J. M. van der Ham, V. Mdluli, M. Schmidtendorf, H. Müller-Bunz, T. W. G. M. Verhoeven, M. Li, J. W. (Hans) Niemantsverdriet, D. G. H. Hetterscheid, S. Bernhard and M. Albrecht, *Eur. J. Inorg. Chem.*, 2020, **2020**, 801–812.

56 H. C. Kolb, M. G. Finn and K. B. Sharpless, *Angew. Chem. Int. Ed.*, 2001, **40**, 2004–2021.

57 V. V. Rostovtsev, L. G. Green, V. V. Fokin and K. B. Sharpless, *Angew. Chem. Int. Ed.*, 2002, **41**, 2596–2599.

58 C. W. Tornøe, C. Christensen and M. Meldal, *J. Org. Chem.*, 2002, **67**, 3057–3064.

59 J. A. Prescher, D. H. Dube and C. R. Bertozzi, *Nature*, 2004, **430**, 873–877.

60 B. T. Worrell, J. A. Malik and V. V. Fokin, *Science*, 2013, **340**, 457–460.

61 Á. Vivancos, C. Segarra and M. Albrecht, *Chem. Rev.*, 2018, **118**, 9493–9586.

62 A. Petronilho, J. A. Woods, H. Mueller-Bunz, S. Bernhard and M. Albrecht, *Chem. Eur. J.*, 2014, **20**, 15775–15784.

63 F. Kloss, U. Köhn, B. O. Jahn, M. D. Hager, H. Görls and U. S. Schubert, *Chem. Asian J.*, 2011, **6**, 2816–2824.

64 M.-L. Teyssot, L. Nauton, J.-L. Canet, F. Cisnetti, A. Chevry and A. Gautier, *Eur. J. Org. Chem.*, 2010, **2010**, 3507–03515.

65 K. F. Donnelly, R. Lalrempuia, H. Müller-Bunz and M. Albrecht, *Organometallics*, 2012, **31**, 8414–8419.

66 S. Farah, T. Tsach, A. Bentolila and A. J. Domb, *Talanta*, 2014, **123**, 54–62.

67 A. R. Parent, R. H. Crabtree and G. W. Brudvig, *Chem. Soc. Rev.*, 2013, **42**, 2247–2252.

68 A. Savini, P. Belanzoni, G. Bellachioma, C. Zuccaccia, D. Zuccaccia and A. Macchioni, *Green Chem.*, 2011, **13**, 3360.

69 C. Zuccaccia, G. Bellachioma, O. Bortolini, A. Bucci, A. Savini and A. Macchioni, *Chem. Eur. J.*, 2014, **20**, 3446–3456.

70 J. M. Thomsen, D. L. Huang, R. H. Crabtree and G. W. Brudvig, *Dalton Trans.*, 2015, **44**, 12452–12472.

71 G. Hu, J. L. Troiano, U. T. Tayvah, L. S. Sharninghausen, S. B. Sinha, D. Y. Shopov, B. Q. Mercado, R. H. Crabtree and G. W. Brudvig, *Inorg. Chem.*, 2021, **60**, 14349–14356.

72 A. Bucci, A. Savini, L. Rocchigiani, C. Zuccaccia, S. Rizzato, A. Albinati, A. Llobet and A. Macchioni, *Organometallics*, 2012, **31**, 8071–8074.

73 I. Corbucci, A. Petronilho, H. Müller-Bunz, L. Rocchigiani, M. Albrecht and A. Macchioni, *ACS Catal.*, 2015, **5**, 2714–2718.

74 Oxford Diffraction, *CrysAlisPro, Version 1.171.40.37a. Oxford Diffraction Ltd., Yarnton, Oxfordshire, UK*, 2018.

75 Oxford Diffraction, *CrysAlisPro, Version 1.171.38.41. Oxford Diffraction Ltd., Yarnton, Oxfordshire, UK*, 2018.

76 P. Macchi, H.-B. Bürgi, A. S. Chimpri, J. Hauser and Z. Gál, *J Appl Crystallogr*, 2011, **44**, 763–771.

77 G. M. Sheldrick, *Acta. Crystallogr. A. Found. Adv.*, 2015, **71**, 3–8.

78 A. L. Spek, *Acta Crystallogr C Struct Chem*, 2015, **71**, 9–18.

79 G. M. Sheldrick, *Acta. Crystallogr. C. Struct. Chem.*, 2015, **71**, 3–8.

80 O. V. Dolomanov, L. J. Bourhis, R. J. Gildea, J. A. K. Howard and H. Puschmann, *J. Appl. Crystallogr.*, 2009, **42**, 339–341.

CHAPTER V

Phenoxy substituted ruthenium PYE complexes

A chelating phenolate-PYE ligand was coordinated to ruthenium, forming a phenolate bridged dimeric species. The dinuclear complex was broken up, into its monomeric counterparts, by addition of suitable ancillary ligands e.g.CH_3CN, pyridine. The complex was further explored for its redox chemistry both by chemical oxidation and spectroelectrochemical means, revealing two reversible redox events. EPR analysis of one-electron oxidized complex indicates that the ligand is non-innocent as the spectrum resembles an organic, ligand-centered radical.

V.1 Introduction

Ligand design is one of the key aspects to generate highly active and durable homogeneous catalysts. While traditional ligands (e.g. amines, halides) are viewed as having static donor properties[1] towards the metal center, new ligand classes have been developed that adapt their donor properties without undergoing structural remodelling. Especially in redox catalysis, where it is necessary to stabilize both high and low valent oxidation states on the metal, such ligands are highly promising. Prime example of such donor-ambiguous ligands are N-heterocyclic carbenes[2–4] (NHCs) which were a breakthrough for many catalytic applications exemplified by Grubbs 2nd generation catalyst.[5] Classic NHCs can be represented by a neutral L-type carbene resonance structure as well as a zwitterionic X-type resonance form.[6,7] The concept of donor ambiguous ligands has also been expanded from C-based to N-based ligands.[8–12] Pyridylidene amines (PYEs) and pyridylidene amides (PYAs) are a recently developped class of such nitrogen based ligands.[13–16] Resulting transition metal complexes can be represented by two mesomeric resonance structures where the ligand coordinates either in a zwitterionic or neutral imine type fashion (Scheme 1.).[13,17] These limiting resonance structures allow PYE ligands to change their donor properties from π-basic strong σ-donors to π-acidic weaker σ-donors based on the needs of the metal center and choice of solvent.[16,18] Recently several pyridylidene based systems have shown outstanding performance in both oxidation and reduction catalysis.[19–24]

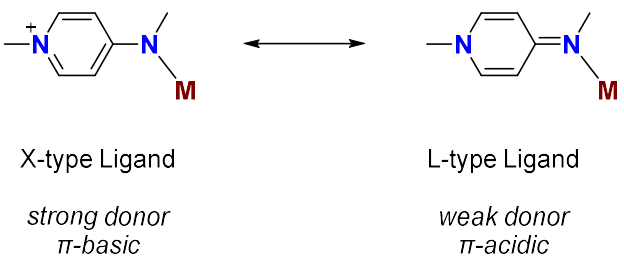

Scheme 1: Limiting resonace structures of *para*-PYE ligands coordinated to a metal center (M)

We hypothesized that combining the electronic flexibility of nitrogen based PYE ligands with a chelating hard oxygen donor could be highly beneficial for potential application in oxidation catalysis. Oxygen coordination is often favoured when higher oxidation states on the metal have to be accessed and in conjunction with an electronically flexible nitrogen site we proposed that redox active complexes should be easily accessible.

Here we investigate a phenoxy substituted PYE-ruthenium(II) complex. We demonstrate the surprising formation of phenolate bridged dimers in non-coordinating solvents which can be easily split into monomeric complexes by addition of various ancillary ligands. Furthermore, the

redox behaviour of the complex was explored and different oxidation states of the complexes were studied.

V.2 Results and discussion

Synthesis and characterisation of PYE-phenolate ruthenium complex. The ligand precursor **1** was easily obtained through neat reaction of 4-chloropyridinium triflate[25] and 2-aminophenol at 170 °C (Scheme 2). It was purified via a precipitation from an acetone solution of the crude product, by addition of CH_2Cl_2. Washing the solid with CH_2Cl_2, gave the ligand precursor **1** in excellent 87% yield as a light beige powder. Reaction of the ligand precursor **1** with $[Ru(p\text{-}cym)Cl_2]_2$ in the presence of Na_2CO_3 as a base afforded the ruthenium complex **2** which was isolated by filtering off the base and precipitating the product from the solution by addition of Et_2O. Removing the supernatant and washing the solid with Et_2O yielded the pure complex as a red solid. The complex is slightly air sensitive and decomposes over a period of several weeks if not stored under inert conditions. Decomposition is visually indicated by a distinct colour change from a red powder to a dark brown one. In non-inert solutions of **2** decomposition is accelerated and visually occurs within a few hours, turning the inital red solution to dark brown one while black deposits formed on the vessel. Notably the complex is however stable in the presence of water. Successfull ruthenation was indicated by ^{1}H NMR spectroscopy in CD_2Cl_2 which shows the absence of the OH and NH protons of the ligand precursor as well as desymmetrisation of the ancillary p-cymene moiety with the aromatic C*H* resonaces split into four distinct doublets (δ_H = 5.13, 4.94, 4.77, 4.36).

^{1}H NMR measurements in CD_3CN indicated slow transformation of the initially dominant species to a new species with all resonances shifted *e.g.* δ_H NCH_3 moved from 3.82 to 3.65 ppm. Signal patterns of the initial complex were reminiscent to those observed in CD_2Cl_2 and show the distinct desymmetrisation of the $CH_{p\text{-}cym}$ resonances (δ_H = 5.17, 4.95, 4.73, 4.31). Over 12 h the initial signals fully disappeared and the new species exhibited overall shifted resonances with only two downfield shifted signals corresponding to $CH_{p\text{-}cym}$ protons (δ_H = 5.66, 5.50). This indicates that rotation of the ancillary cymene ligand was now less hindered than in the parent complex and therefore the two α-$CH_{p\text{-}cym}$ protons, as well as the two β-$CH_{p\text{-}cym}$ protons, appear as equivalent. Thus, the formation of a monomeric ruthenium complex, where the third leg of the piano stool configuration consists of a coordinating chloride or triflate, which is a common coordination pattern for ruthenium arene complexes featuring bidentate N,N and N,O ligands, was unlikely.[20,26,27] The different behaviour in coordinating and non-coordinating solvents indicated reversible coordination of CD_3CN as an ancillary ligand to the ruthenium center.

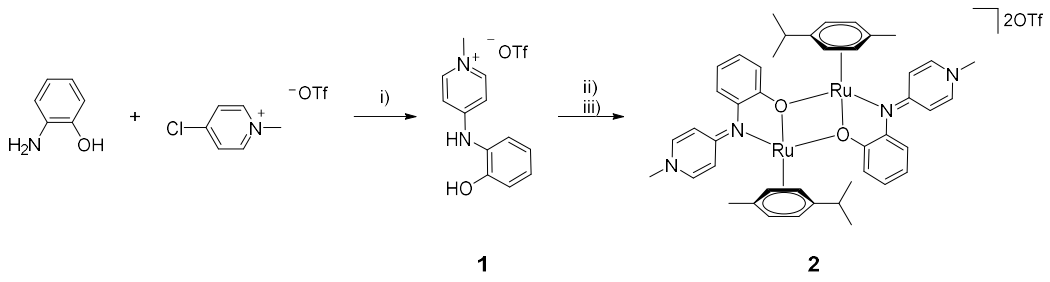

1 **2**

Scheme 2: Synthesis of phenoxy-PYE ligand precursor **1** and ruthenium complex **2**. Reaction conditions: i) neat, 180°C; ii) Na_2CO_3, $[Ru(p\text{-}cym)Cl_2]_2$, CH_3CN; iii) precipitation with Et_2O

Crystals of **1** and **2** were obtained by vapour diffusion techniques (CH_2Cl_2 into an acetone solution of **1**; Et_2O into a CH_3CN solution of **2**). Single crystal X-ray diffraction analysis of **1** confirmed the expected configuration of the ligand. Analysis of complex **2** revealed a dimeric structure where the ruthenium centres are bridged by the phenolate oxygen atoms of the two chelated ligands (Figure 1). Bridging phenolates in dinuclear ruthenium arene complexes were previously reported for example by Brunner et al[28] where salicylaldiminato ligands were employed and by Wong et al[29] which observed a similar coordination mode with a salen-type ligand. Bonding distances from the ruthenium centres to the bridging oxygen atoms are in the same range towards both oxygen atoms (*cf.* Table 1: Ru–O 2.129(3) and 2.126(3) Å). These bond distances are comparable to those observed for the similar complexes reported by Brunner (Ru1–O1 2.093(11); Ru1–O2 2.125(7); Ru2–O1 2.146(7); Ru2–O2 2.110(11)) and Wong (Ru1–O1 2.089(2); Ru1–O2 2.272(2); Ru2–O1 2.081(2); Ru2–O2 2.267(2)). In complex **2** the PYE C_α–C_β bonds (1.356(7) Å) are significantly shorter than C_β–C_γ bonds (1.430(7) Å), indicating high contribution of the neutral imine resonance structure in the ligand. The observed dimeric configuration allowed rationalization of the ^{1}H NMR experiments. In the solid the ruthenium species is present as the dimeric species **2** and this species is also present in non-coordinating solvents such as CH_2Cl_2. In coordinating solvents however the solvent coordinates to the ruthenium centres and break up the dimer to form $\mathbf{3_{Ligand}}$ (Fig. 2). High resolution mass spectrometry measured shortly after dissolution of **2** in CH_3CN showed diagnostic m/z signals for both the monomeric Ru complex at 435.0985 (calculated for $[M_{monomer} - OTf]^+$: 435.1005) and the dimeric complex 1018.1526 (calculated for $[M_{dimer} - OTf]^+$: 1018.1553).

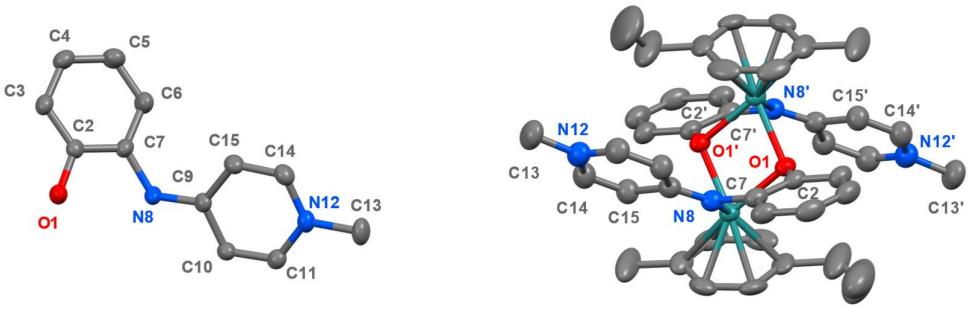

I II

Figure 1: Molecular X-ray structures (50% probability ellipsoids) of ligand precursor **1** (**I**) and complex **2** (**II**), hydrogen atoms, co-crystallized solvent molecules and non-coordinating OTf^- counter anions omitted for clarity. Space group of II: $P2_1/c$

Table 1: Selected bond lengths (Å) and angles (deg) for ligand precursor **1** and complex **2**.

	1	**2**
Ru1–O1	-	2.129(3)
Ru1–O1’	-	2.126(3)
Ru1–N8	-	2.117(4)
$C_{PYE\alpha}$–$C_{PYE\beta}$	1.359(2) [a]	1.356(7) [a]
$C_{PYE\beta}$–$C_{PYE\gamma}$	1.412(3) [a]	1.430(7) [a]
$C_{PYE\gamma}$–N8	1.340(2)	1.329(6)

[a] average of both bonds in the heterocycle

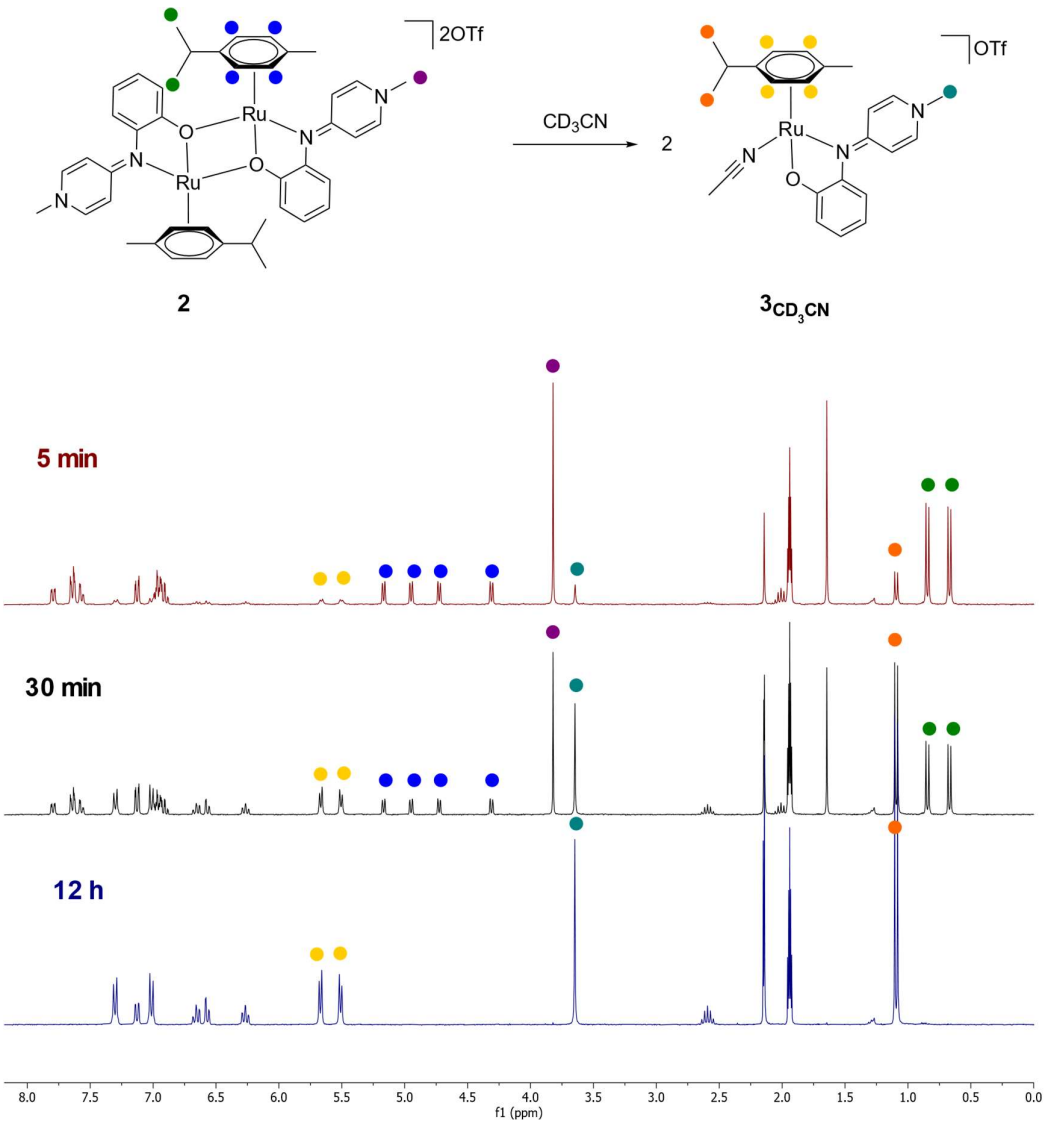

Figure 2: Dissociation of dimeric ruthenium complex **2** and formation of monomeric complex $\mathbf{3_{CD3CN}}$ in CD_3CN solution with corresponding ^1H NMR spectra.

It has to be noted that in non coordinating CD_2Cl_2 solutions of complex **2** a secondary set of resonances appear over time (2 h) with shifted resonances of the ON-ligand as well as of the ancillary cymene (cf. $CH_{p\text{-}cym}$ **[2]** δ_H = 5.14, 4.94, 4.77, 4.36 vs δ_H = 6.18, 5.77, 5.66, 5.47) After that time, the signal ratio stays constant (4:1) indicating that an equilibrium between the two species was established. The asymmetric $CH_{p\text{-}cym}$ resonances of the minor species indicate that not a monomeric complex is observed, as based on the spectras obtained for $\mathbf{3_{CD3CN}}$ only two singlets are expected, although underligated metal complexes with similar ligands are known[22]. Addition of CH_3CN to the CD_2Cl_2 solution leads to slow disappearance of the present signals and eventually clean formation of the monomeric complex, demonstrating that the signals corresponding to the minor species are not due to decomposition products.

Temperature-dependent ^{1}H NMR experiments of CH_2Cl_2 solutions show that lowering the temperature to -40 °C has no effect on the equilibrium between the major and minor species. Increasing the temperature however lowered the intensity of the minor species to a xx:yy ratio. This further indicates that no monomeric species is formed in CH_2Cl_2 as at lower temperature dimer-formation should be favoured and at higher temperature the monomer concentration should increase, contrary to experimental evidence. The temperature dependence can be rationalized by formation of a rotamer (**2**$_{rota}$). When solid complex **2** is formed in the synthesis from **3**$_{CH3CN}$ which is present in solution, only one major species is formed which is the energetically favoured one observed in the crystal structure. In solution at r.t. the cymene can however rotate leading to the minor species observed in ^{1}H NMR. Lowering the temperature thus makes rotation even more hindered and freezes out the ratio in the state it was previously present, whereas increased temperature allows easier rotation so that on average only the energetically favoured rotamer **2** is observed. Thus the new set of signals is attributed to the formation of a conformer **2**$_{rota}$ where the cymene ligands are rotated by 180° (Figure 3).

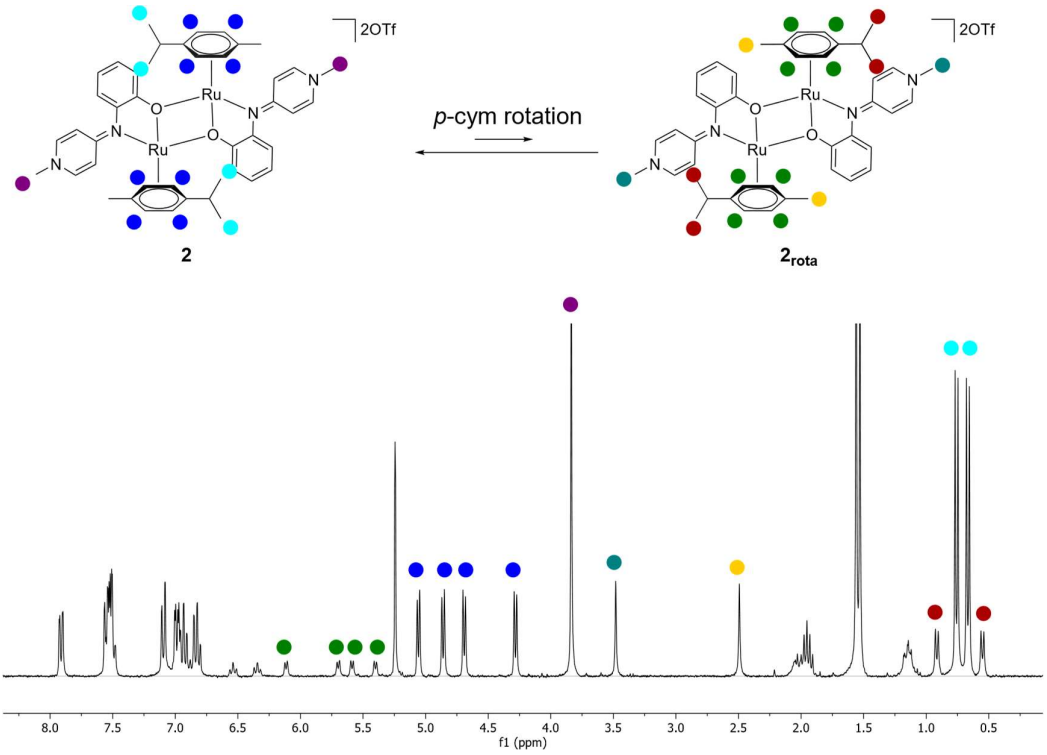

Figure 3: Conformers observable in non coordinating CD_2Cl_2 solutions of **2** by ^{1}H NMR spectroscopy. The spectrum was recorded after letting the system equilibrate for 12 h at r.t.

The ligand-induced dimeric breakup of **2** is of high interest for potential catalytic applications as it can provide facile access to a free coordination site, pontentially eliminating complicated

catalyst activation steps. Thus various anicillary ligands were tested for their ability to break up the dimer by addition of 100 eq of potential ligand to CD_2Cl_2 solutions of **2**. The primary amine (1-hexylamine) led to quick formation of monomeric species $\mathbf{3_{amine}}$, indicated by the disappearance of $CH_{p\text{-}cym}$ resonaces of **2** (δ_H = 5.17, 4.95, 4.73, 4.31). Concommitantly the $CH_{p\text{-}cym}$ resonances of $\mathbf{3_{amine}}$ appeared at δ_H = 5.52 (3H) and 5.39 (1H). The resulting complexes are quickly formed at r.t. and after 5 min 90% of the dimer is broken up, with only monomeric complexes observed after 20 min (Fig. 4). Pyridine addition led to very similar spectral changes overall, $CH_{p\text{-}cym}$ resonances of $\mathbf{3_{pyridine}}$ appeared at δ_H = 5.79 (2H) and 5.52 (2H). Full dimeric break up took around 1 h to completion. PPh_3 (50 eq) led again to similar spectral changes during monomer formation but in $\mathbf{3_{PPH3}}$ the $CH_{p\text{-}cym}$ resonaces appear as 4 distinct doublets (δ_H = 6.18, 5.88, 5.63, 5.30) as in **2**. Furthermore the cym–C*H*$_3$ resonaces of $\mathbf{3_{PPH3}}$ were observed as two doublets (δ_H = 1.28, 0.94) instead of one, which was observed for the other monomers ($\mathbf{3_{Ligand}}$). The increased splitting is likely caused by the steric bulk of the PPh_3 ligand. It fully broke up the dimer after 12 h of reaction, slow reaction is potentially as well corelated to the high steric demand. 100 equivalents of CH_3CN did not fully break up the dimer and took 24 h to reach equilibrium conditions. Aliphatic alcohols (1-decanol) did not induce any dimer break up and appear to be poor ligands for the complex.

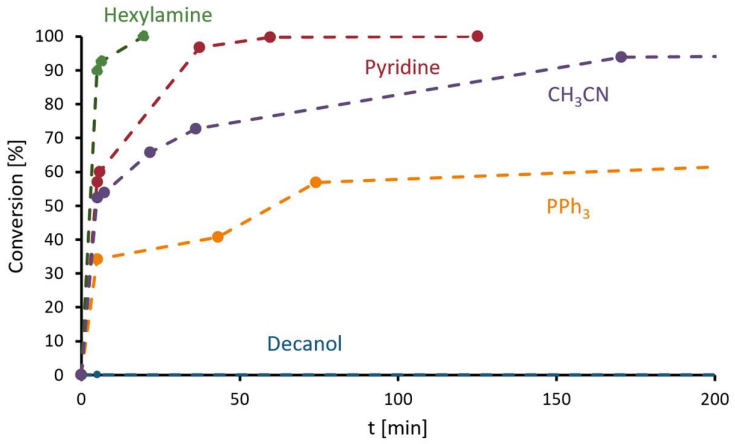

Figure 4. Conversion profile of dimeric complex **2** to monomeric $\mathbf{3_{Ligand}}$ upon addition of exogenous ligands to CD_2Cl_2 solutions of **2.** Conversions determined by ^{1}H NMR. Conditions: CD_2Cl_2 (0.6 ml), **2** (5 mg, 4.28 µmol), potential ligands (100 eq, except for PPh_3 (50eq)).

Electrochemical analysis of complex 2. Cyclovoltammetric (CV) measurements were used to probe the potential of the complex for redox reactions. The measurements were performed in non-coordinating CH_2Cl_2 where the dimer is present and in CH_3CN where the monomeric species dominates (Fig. 5). In both solvents two apparently reversible redox events are

observed ($E_{1/2}$ (CH_3CN): -0.006 and 0.42 V; $E_{1/2}$ (CH_2Cl_2): 0.08 and 0.42V; potentials vs Fc/Fc+). Notably the second redox event happens at the same potential $E_{1/2}$ = 0.42 V in both solvents.

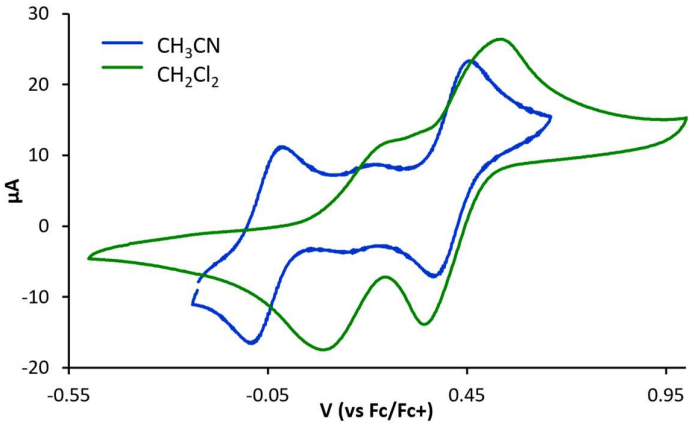

Figure 5: Cyclic voltammograms of complex **2** in CH_2Cl_2 and CH_3CN. Potentials given *vs.* Fc/Fc+; (nBu$_4$N)PF_6 as electrolyte, 100 mVs^{-1} scan rate)

Chemical oxidation of complex 2. When complex **2** is exposed to air it is slowly oxidized as evidenced by broadened ^{1}H NMR signals that indicate formation of a paramagnetic complex. However initial spectra were at least partially recovered by addition of hydrazine as a reductant indicating that **2**/**3** undergo reversible redox chemistry. As **2**/**3** also are stable in cyclic voltammetry, chemical oxidation of the complex was attempted. Addition of 1 eq $Cu(OTf)_2$ as an oxidant to a CH_3CN solution of **2** led to an immediate colour change from red to purple. Thus the reaction was followed by UV-vis spectroscopy (Fig. 6) where a $Cu(OTf)_2$ solution was portionwise added to a CH_3CN solution of **2**. After addition of 1 eq, the main absorbance of the red complex **3** at 380 nm diminishes and a new λ_{max} is observed at 550 nm for the purple product. Addition of another equivalent of oxidant then lead to the formation of another species with λ_{max} = 515 nm. During further additions of oxidant the formation of a new species with λ_{max} = 590 was observed. The 550 nm absorbance is attributed to the formation of a one-electron oxidized complex **[3]$^+$**. It has to be noted that many aminophenolate type ligands are redox non-innocent, which means that the oxidation event might not be metal centered but might have occured on the ligand.[30,31] The 515 nm absorption should correspond to a second one-electron oxidation event where **[3]$^{2+}$** is formed. The third event is more difficult to explain as it was not observed by cyclic voltammetry experiments.

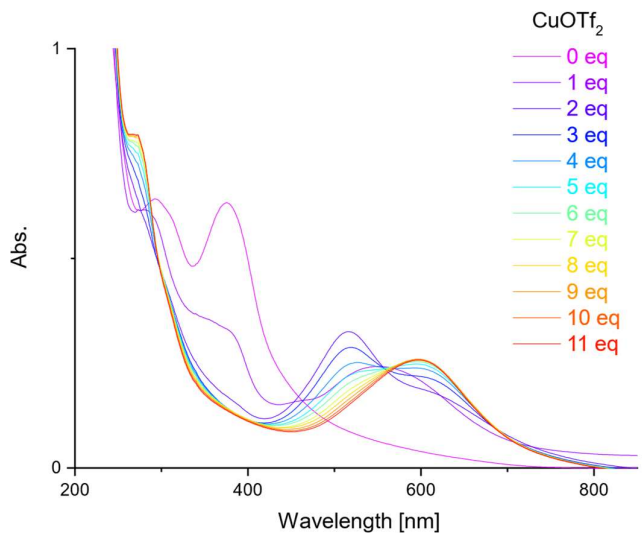

Figure 6: Chemical oxidation of complex **2** followed by UV-vis spectroscopy. To a stock solution of **2** (0.08 mg in 2ml) in CH_3CN aliquots of $Cu(OTf)_2$ were added (20 µl as a solution in CH_3CN (24.7 mg in 10ml))

Spectroelectrochemical analysis: To exclude undesired interference of the oxidant in the UV-vis spectrum spectroelectrochemistry was used to monitor the reactivity. The measurement was performed in an optically transparent thin-layer electrochemical (OTTLE) cell,[32] which allows electrolysis of an analyte while monitoring the formed species through a transparent window . The reaction was set up by loading a degassed CH_3CN solution of **2,** with NBu_4PF_6 as an electrolyte, into an OTTLE cell. The cell was placed in a UV-vis spectrometer and the window of the electrochemical cell aligned with the light source. The first oxidation event observable in CV measurements (E_{pc} = 0.1 V) was isolated by fixed potential oxidation at 0.1 V and concomitantly UV-vis spectra were recorded (Fig. 7). These spectra showed a decrease of the 380 nm absorption of complex **3** over time and gradual build-up of the **[3]**$^+$ species with λ_{max} = 535 nm. After ca. 300 s the spectrum stabilized and did not change significantly anymore indicating that all **3** was oxidized. The spectra resembeled closely those from the chemical oxidation experiments after addition of 1eq $Cu(OTf)_2$ (Fig. 8). The oxidation potential was then raised to 0.6 V to observe the second oxidation event (E_{pc} = 0.5 V). Consistent with chemical oxidation, the formation of the species at 515 nm was observed before the species at 590 nm emerged over time. Yet cyclic voltammetry in CH_3CN did not show any decrease in current around the 2nd oxidation event, even after 20 scans. We thus tentatively attribute the emergence of the 590 nm species to decomposition events triggered by the presence of traces of oxygen in the non-inert UV-vis setups.

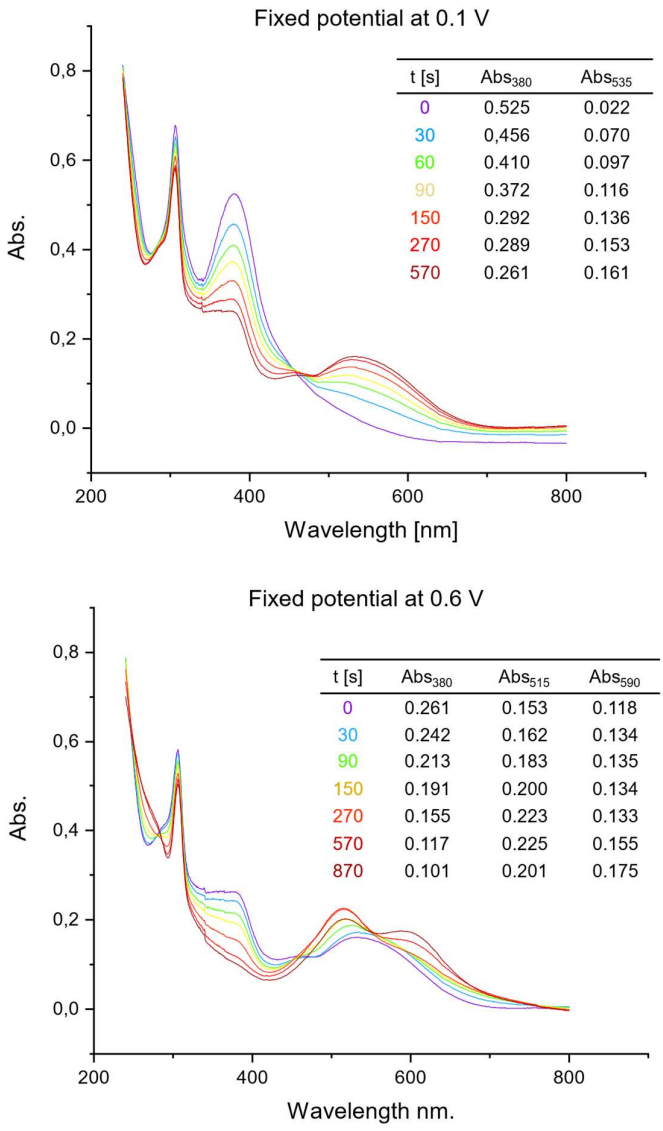

Ottle cell

Figure 7: Spectroelectrochemical oxidation of complex **2**. A degassed CH_3CN solution of **1** (0.003 M) with 0.1M NBu_4PF_6 was loaded into an OTTLE cell. The cell was placed in the UV-vis spectrometer and the window of the electrochemical cell aligned with the light source. The first oxidation event observable in CV measurements was isolated by fixed potential oxidation at 0.1 V and concomitantly UV spectras were recorded. The oxidation potential was then raised to 0.6 V to observe the second oxidation event. Potentials are given in V vs Fc/Fc+

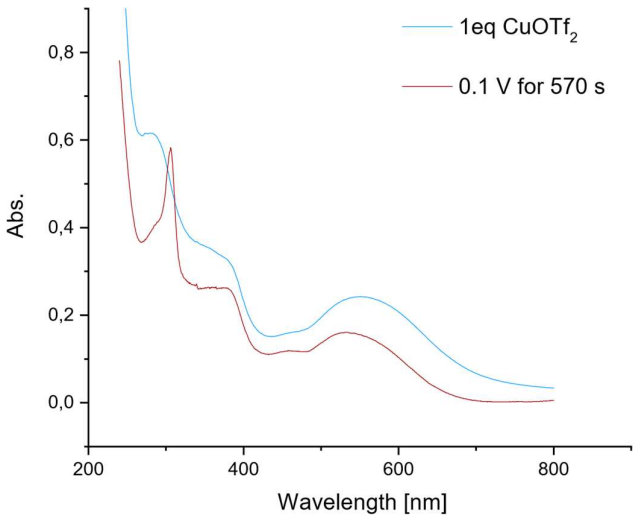

Figure 8: UV-vis spectra of **2** oxidized by different methods. Chemical oxidation with 1eq $CuOTf_2$ (see Fig. 6) and spectroelectrochemical oxidation in an ottle cell with 0.1 V fixed oxidation potential (see Fig. 7).

EPR analysis. Ligands derived from 2-aminophenols can potentially be critically involved in the oxidation chemistry of metal complexes and this redox non-innocence is well documented in literature.[33,34,31,35–37] In such cases oxidation of a metal complex does not necessarily take place on the metal center but can be located on the ligand. EPR measurements of **2** oxidized with 1eq of $Cu(OTf)_2$ where thus performed (Fig. 9). The obtained spectrum is highly symmetrical with a g-facter of 2.002. A g-factor of g = 2 is indicative for the formation of an organic radical which in this case is likely located on the ligand.[38] For a metal centered radical the g-factor would likely significantly deviate from a g-facter of 2.00, we thus suggest that the phenoxy-PYE ligand is redox non-innocent.

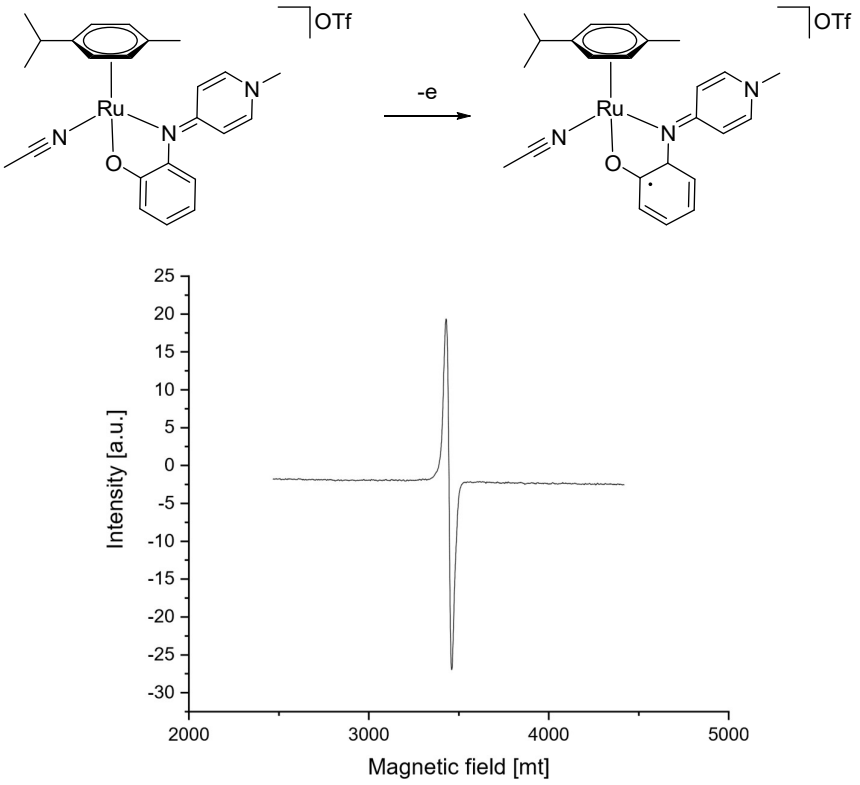

Figure 9: Proposed formation of ligand centered radical upon one electron oxidation. EPR spectrum of complex **2** after oxidation with 1 eq $CuOTf_2$. A g-factor of 2.002 points to a ligand centered radical.

V.3 Conclusion

In summary a ruthenium phenoxy-PYE complex was synthesized. Single crystal X-Ray diffraction analysis revealed that in the solid state the complex is present as a dimeric species where the phenolates bridge two ruthenium centers. In solution addition of ancillary ligands can break up the dimer and this latent free coordination site was explored by addition of various ligands whereby a preference for primary amines was established. The complex showed distinct redox behaviour in air where it was oxidized to **[2]$^+$**. The reduced complex **[2]** was restored by adding chemical reductants. Electrochemical analysis revealed that the complex undergoes two reversible oxidation events at $E_{1/2}$ = -0.006 and 0.42 V, which were further characterized by UV-vis spectroscopy. While electrochemical analysis suggest a quite stable complex rapid decomposition is observed at elevated temperatures in various solvents and with several potential substrates rendering the complex unpromising for catalytic applications so far.

V.4 Experimental section

General

4-Chloropyridinium triflate was synthesized according to a literature procedure.[25] All other reagents were commercially available and used as received unless specified. NMR spectra were recorded at 25 °C on Bruker spectrometers operating at 300 or 400 MHz (^{1}H NMR and 75 or 100 MHz (^{13}C{^{1}H} NMR), respectively. Chemical shifts (δ in ppm, coupling constants J in Hz) were referenced to residual solvent signals (^{1}H,^{13}C). Assignments are based on homo- and hetero nuclear shift correlation spectroscopy. High resolution mass spectrometry was carried out by the DCBP mass spectrometry group at the University of Bern with with a Thermo Scientific LTQ Orbitrap XL (ESI-TOF). Elemental analyses were performed on a Thermo Scientific Flash 2000 CHNS-O elemental analyzer by the DCBP Microanalytic Laboratory. Cyclic voltammograms were recorded using an Autolab PGSTAT101 from Metrohm in MeCN, and CH_2Cl_2 solutions: 10 mL solvent, 1 mM sample, and 100 mM tetrabutylammonium hexafluorophosphate $(nBu_4N)PF_6$ as supporting electrolyte. Solutions were deaerated with argon gas for 10 min prior to each run. The Fc^+/Fc couple was used as an internal reference. A Pt disk with a 3.80 mm^2 surface area was used as a working electrode and polished before each measurement. The reference electrode was an Ag/AgCl electrode (SSCE); the counter electrode was a Pt-wire. The UV-vis measurements were carried out on an UV-1800 from Shimadzu with 1 cm quartz cuvettes. Spectroelectrochemical measurements with the OTTLE cell were carried out in the same UV-1800 with a Specac omni cell connected to an Autolab PGSTAT101 from Metrohm.

Ligand precursor 1

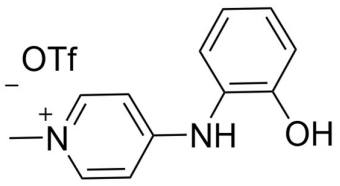

2-Aminophenol (374.3 mg, 3.43 mmol) and 4-chloropyridinium triflate (3.6 mmol, 1000 mg) were loaded into a schlenk flask and mixed. Under N_2 atmosphere the reaction was heated to 170 °C and stirred for 5 h, resulting in a deep green viscous solution. The reaction was cooled down and left open to air over night, resulting in solidification of the reaction. The crude was dissolved in a minimal amount of acetone and CH_2Cl_2 was added until a light yellow solid precipitated. The supernatant was removed and the solid washed twice with CH_2Cl_2 to yield the pure ligand precursor **1** as a light yellow solid 1040 mg (87%). Suitable crystals for single crystal X-ray analysis were grown by vapour diffusion of CH_2Cl_2 into an acetone solution of **1**. ^{1}H NMR (400 MHz, Acetone-d_6) δ 9.59 (s, 1H, NH/OH), 9.15 (s, 1H, NH/OH), 8.31 (d, J = 7.2 Hz, 2H, $CH_{PYE\ \alpha}$), 7.31 (dd, J = 7.8, 1.6 Hz, 1H, CH_{Ph}), 7.28 – 7.22 (m, 1H, CH_{Ph}), 7.25 – 6.90 (broad s, 2H, $CH_{PYE\ \beta}$), 7.12 (dd, J = 8.2, 1.4 Hz, 1H, CH_{Ph}), 6.96 (td, J = 7.6, 1.4 Hz, 1H, CH_{Ph}), 4.16 (s, 3H, CH_3). ^{13}C NMR (101 MHz, Acetone) δ 156.66, 152.06 (2 × C_{Ar}), 143.89 ($CH_{PYE\ \alpha}$), 128.90,

126.46 (2 × C_{Ph}), 123.79 (C_{Ar}), 120.26 (C_{Ph}), 119.72 (C_{Ar}), 117.26 (C_{Ph}), 44.76 (CH_3). HR-MS (m/z): Calculated for $C_{12}H_{13}N_2O$: 201.1022 *m/z* [M – OTf]$^+$; found 201.1019.

Complex 2

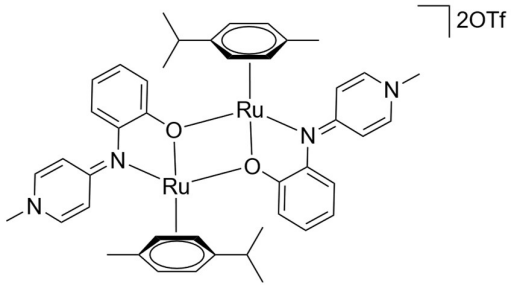

The full synthesis was carried out under N_2 atmosphere and with degassed solvents. Ligand precursor **1** (200 mg, 571 µmol), $[RuCl_2(p\text{-cym})]_2$ (174.8 mg, 286 µmol) and Na_2CO_3 (202 mg 1.9 mmol) were mixed in dry CH_3CN (10 mL) and stirred at r.t. for 3 h. Stirring was stopped and solids left to settle before the supernatant was filtered off under nitrogen atmosphere. The red solution was concentrated under N_2 flow before degassed Et_2O was added until precipitation occurred (50 mL). The Supernatant was removed and the red solid layered with Et_2O and left for 1 h. All solids were scratched from the walls and washed twice with Et_2O. All volatiles were then removed under vacuum to yield complex **2** as a red solid (135 mg, 54%). Crystals suitable for X-ray diffraction analysis were grown by vapor diffusion of Et_2O into a CH_3CN solution of **2**.

^{1}H NMR (300 MHz, CD_3CN) δ 7.35 – 7.27 (m, 2H, PYE_α), 7.13 (dd, $^3J_{HH}$ = 7.8, $^4J_{HH}$ = 1.5 Hz, 1H, H_{Ph}), 7.06 – 6.98 (m, 2H, PYE_β), 6.72 – 6.53 (m, 2H, H_{Ph}), 6.27 (ddd, $^3J_{HH}$ = 8.3, $^4J_{HH}$ =7.0, 1.6 Hz, H_{Ph}), 5.67 (d, $^3J_{HH}$ = 5.9 Hz, 2H, H_{cym}), 5.51 (d, $^3J_{HH}$ = 5.9 Hz, 2H, H_{cym}), 3.65 (s, 3H, NCH_3), 2.60 (hept, $^3J_{HH}$ = 6.9 Hz, 1H, C*H*Me$_2$), 2.14 (s, 3H, cym–CH_3), 1.10 (d, $^3J_{HH}$ = 6.9 Hz, 6H, (CH_3)$_2$CH).

^{13}C NMR (75 MHz, CD_3CN) δ 169.39, 161.50, 144.04 (3 × Cq), 140.92 (PYE_α), 125.33 , 120.34, 117.35 (3 ×C_{Ph}), 115.80 (PYE_β), 113.32, (C_{Ph}), 103.47, 100.07 (2 × Cq), 85.22, 83.15 (2 × CH_{cym}), 43.87 (pyr–CH_3), 31.69 (*C*HMe$_2$), 22.26 (2 × CH(*C*H$_3$)$_2$), 18.76 (cym–*C*H$_3$).

HR-MS (m/z): Calculated for [$M_{monomer}$ – OTf]$^+$: 435.1005 *m/z*; found 435.0985; Calculated for [M_{dimer} – OTf]$^+$: 1018.1553 found 1018.1526. Elem. Anal. Calc. (%) for [$C_{46}H_{50}F_6N_4O_8Ru_2S_2$]: C 47.34, H 4.32, N 4.80; found: C 46.91, H 4.29, N 4.72.

Crystal structure determination of 1. A crystal of **1** and **2** was mounted in air at ambient conditions. All measurements were made on a RIGAKU Synergy S area-detector diffractometer[39] using mirror optics monochromated Cu Kα radiation (λ = 1.54184 Å).[40] The unit cell constants and an orientation matrix for data collection were obtained from a least-squares refinement of the setting angles of reflections. Data reduction was performed using the CrysAlisPro[39] program. The intensities were corrected for Lorentz and polarization effects, and an absorption correction based on the multi-scan method using SCALE3 ABSPACK in

CrysAlisPro[39] was applied. Data collection and refinement parameters are given in Table 2. The structure was solved by direct methods using SHELXT[41], which revealed the positions of all non-hydrogen atoms of the title compound. All non-hydrogen atoms were refined anisotropically. H-atoms were assigned in geometrically calculated positions and refined using a riding model where each H-atom was assigned a fixed isotropic displacement parameter with a value equal to 1.2Ueq of its parent atom (1.5Ueq for methyl groups). Refinement of the structure was carried out on F^2 using full-matrix least-squares procedures, which minimized the function $\Sigma w(Fo^2 - Fc^2)^2$. The weighting scheme was based on counting statistics and included a factor to downweight the intense reflections. All calculations were performed using the SHELXL-2014/7[42] program in OLEX2.[43]

Table 2. Crystal data and structure refinement for **1** and **2**.

Identification code	**1**	**2**
Empirical formula	$C_{13}H_{13}F_3N_2O_4S$	$C_{50}H_{56}F_6N_6O_8Ru_2S_2$
Formula weight	350.31	1249.26
Temperature/K	173.01(10)	173.01(10)
Crystal system	triclinic	monoclinic
Space group	*P*-1	$P2_1/c$
a/Å	9.2555(3)	11.65550(10)
b/Å	9.8831(3)	23.6692(3)
c/Å	9.9799(3)	9.50840(10)
α/°	60.433(3)	90
β/°	81.420(2)	97.6380(10)
γ/°	72.067(3)	90
Volume/Å^3	755.43(5)	2599.87(5)
Z	2	2
ρ_{calc}g/cm^3	1.540	1.596
μ/mm^{-1}	2.437	6.149
F(000)	360.0	1272.0
Crystal size/mm^3	0.2 × 0.2 × 0.1	0.1 × 0.1 × 0.05
Radiation	CuKα (λ = 1.54184)	CuKα (λ = 1.54184)
2Θ range for data collection/°	10.044 to 143.13	7.47 to 154.83
Index ranges	-11 ≤ h ≤ 11, -12 ≤ k ≤ 12, -12 ≤ l ≤ 12	-11 ≤ h ≤ 14, -29 ≤ k ≤ 28, -12 ≤ l ≤ 12
Reflections collected	13861	25069
Independent reflections	2888 [R_{int} = 0.0355, R_{sigma} = 0.0256]	5375 [R_{int} = 0.0382, R_{sigma} = 0.0239]
Data/restraints/parameters	2888/0/217	5375/0/327
Goodness-of-fit on F^2	1.080	1.075
Final R indexes [I>=2σ (I)]	R_1 = 0.0410, wR_2 = 0.1132	R_1 = 0.0524, wR_2 = 0.1444
Final R indexes [all data]	R_1 = 0.0432, wR_2 = 0.1152	R_1 = 0.0544, wR_2 = 0.1461
Largest diff. peak/hole / e Å^{-3}	0.35/-0.45	1.32/-0.94

V.5 References

1 J. F. Hartwig, *Organotransition metal chemistry: from bonding to catalysis*, University Science Books, Sausalito, Calif, 2010.

2 A. J. Arduengo, R. L. Harlow and M. Kline, *J. Am. Chem. Soc.*, 1991, **113**, 361–363.

3 M. N. Hopkinson, C. Richter, M. Schedler and F. Glorius, *Nature*, 2014, **510**, 485–496.

4 D. Bourissou, O. Guerret, F. P. Gabbaï and G. Bertrand, *Chem. Rev.*, 2000, **100**, 39–92.

5 M. Scholl, T. M. Trnka, J. P. Morgan and R. H. Grubbs, *Tetrahedron Letters*, 1999, **40**, 2247–2250.

6 Á. Vivancos, C. Segarra and M. Albrecht, *Chem. Rev.*, 2018, **118**, 9493–9586.

7 F. E. Hahn and M. C. Jahnke, *Angew. Chem. Int. Ed.*, 2008, **47**, 3122–3172.

8 H. Bruns, M. Patil, J. Carreras, A. Vázquez, W. Thiel, R. Goddard and M. Alcarazo, *Angewandte Chemie International Edition*, 2010, **49**, 3680–3683.

9 Á. Kozma, J. Rust and M. Alcarazo, *Chem. Eur. J.*, 2015, **21**, 10829–10834.

10 D. Petrovic, C. G. Hrib, S. Randoll, P. G. Jones and M. Tamm, *Organometallics*, 2008, **27**, 778–783.

11 J. Börner, U. Flörke, T. Glöge, T. Bannenberg, M. Tamm, M. D. Jones, A. Döring, D. Kuckling and S. Herres-Pawlis, *Journal of Molecular Catalysis A: Chemical*, 2010, **316**, 139–145.

12 B. S. Khan, V. Flores-Romero, J. LeBlanc and G. G. Lavoie, *Organometallics*, 2022, **41**, 2668–2677.

13 J. Slattery, R. J. Thatcher, Q. Shi and R. E. Douthwaite, *Pure and Applied Chemistry*, 2010, **82**, 1663–1671.

14 M. E. Doster and S. A. Johnson, *Angew. Chem.*, 2009, **121**, 2219–2221.

15 P. D. W. Boyd, L. J. Wright and M. N. Zafar, *Inorg. Chem.*, 2011, **50**, 10522–10524.

16 V. Leigh, D. J. Carleton, J. Olguin, H. Mueller-Bunz, L. J. Wright and M. Albrecht, *Inorg. Chem.*, 2014, **53**, 8054–8060.

17 Q. Shi, R. J. Thatcher, J. Slattery, P. S. Sauari, A. C. Whitwood, P. C. McGowan and R. E. Douthwaite, *Chem. Eur. J.*, 2009, **15**, 11346–11360.

18 A. J. Bukvic, V. Kesselring, M. Aeschlimann and M. Albrecht, *Inorg. Chem.*, 2023, **62**, 2905–2912.

19 S. Bertini, D. Henryon, A. J. F. Edmunds and M. Albrecht, *Org. Lett.*, 2022, **24**, 1378–1382.

20 K. Salzmann, C. Segarra and M. Albrecht, *Angew. Chem. Int. Ed.*, 2020, **59**, 8932–8936.

21 P. Melle, J. Thiede, D. A. Hey and M. Albrecht, *Chem. Eur. J.*, 2020, **26**, 13226–13234.

22 N. Lentz and M. Albrecht, *ACS Catal.*, 2022, 12627–12631.

23 N. Lentz, Y. Streit, P. Knörr and M. Albrecht, *Chem. Eur. J.*, 2022, e202202672.

24 M. Navarro, M. Li, H. Müller-Bunz, S. Bernhard and M. Albrecht, *Chem. Eur. J.*, 2016, **22**, 6740–6745.

25 E. Stander-Grobler, O. Schuster, G. Heydenrych, S. Cronje, E. Tosh, M. Albrecht, G. Frenking and H. G. Raubenheimer, *Organometallics*, 2010, **29**, 5821–5833.

26 A. Fujii, S. Hashiguchi, N. Uematsu, T. Ikariya and R. Noyori, *J. Am. Chem. Soc.*, 1996, **118**, 2521–2522.

27 C. Gemel, R. John, C. Slugovc, K. Mereiter, R. Schmid and K. Kirchner, *J. Chem. Soc., Dalton Trans.*, 2000, 2607–2612.

28 H. Brunner, R. Oeschey and B. Nuber, *Journal of Organometallic Chemistry*, 1996, **518**, 47–53.

29 C.-Y. Wong, W.-L. Man, C. Wang, H.-L. Kwong, W.-Y. Wong and T.-C. Lau, *Organometallics*, 2008, **27**, 324–326.

30 N. P. van Leest, F. J. de Zwart, M. Zhou and B. de Bruin, *JACS Au*, 2021, **1**, 1101–1115.

31 O. R. Luca and R. H. Crabtree, *Chem. Soc. Rev.*, 2013, **42**, 1440–1459.

32 M. Krejčik, M. Daněk and F. Hartl, *Journal of Electroanalytical Chemistry and Interfacial Electrochemistry*, 1991, **317**, 179–187.

33 A. L. Smith, K. I. Hardcastle and J. D. Soper, *J. Am. Chem. Soc.*, 2010, **132**, 14358–14360.

34 M. R. Haneline and A. F. Heyduk, *J. Am. Chem. Soc.*, 2006, **128**, 8410–8411.

35 H. Masui, A. B. P. Lever and P. R. Auburn, *Inorg. Chem.*, 1991, **30**, 2402–2410.

36 G. Skara, M. Gimferrer, F. De Proft, P. Salvador and B. Pinter, *Inorg. Chem.*, 2016, **55**, 2185–2199.

37 M. R. Ringenberg, S. L. Kokatam, Z. M. Heiden and T. B. Rauchfuss, *J. Am. Chem. Soc.*, 2008, **130**, 788–789.

38 R. H. Crabtree, *The organometallic chemistry of the transition metals*, Wiley, Hoboken, New Jersey, Sixth edition., 2014.

39 Oxford Diffraction, *CrysAlisPro, Version 1.171.40.37a. Oxford Diffraction Ltd., Yarnton, Oxfordshire, UK*, 2018.

40 P. Macchi, H.-B. Bürgi, A. S. Chimpri, J. Hauser and Z. Gál, *J Appl Crystallogr*, 2011, **44**, 763–771.

41 G. M. Sheldrick, *Acta. Crystallogr. A. Found. Adv.*, 2015, **71**, 3–8.

42 G. M. Sheldrick, *Acta. Crystallogr. C. Struct. Chem.*, 2015, **71**, 3–8.

43 O. V. Dolomanov, L. J. Bourhis, R. J. Gildea, J. A. K. Howard and H. Puschmann, *J. Appl. Crystallogr.*, 2009, **42**, 339–341.

CHAPTER VI

Conclusions

This thesis details the synthesis of ruthenium- and iridium-based transition metal complexes and their exploitation in challenging catalytic applications.

An easily accessible NNN ligand system (PYE-Amide-Quinoline) was developed and coordinated to ruthenium cymene. The resulting complex showed very high catalytic activity when applied in base-free formic acid dehydrogenation. Mechanistic investigations indicated that in the catalytically active species, the NNN ligand and cymene are still coordinated to the Ru center. While highly active, the catalysts deactivated quickly. As the parent Ru(II)-NNN system is highly modular a series of derivative complexes were easily accessed. Protonation and methylation of the central nitrogen drastically lowered catalytic activity, demonstrating the crucial role of this position for high performance. Choice of ancillary arene was shown to be essential for longevity of the catalyst, with weaker coordinating benzene analogs of the parent complex quickly deactivating under catalytic conditions. Simple electronic modification on the NNN framework, in particular introducing an electron withdrawing CF_3 group on the connecting phenyl mojety in the ligand backbone, resulted in the most active ruthenium complex for base free formic acid dehydrogenation to date with TOFs of 27,000 h^{-1}. While highly active the system suffers from low longevity. The shortcomings might be addressed by either anchoring the ancillary arene to the main ligand, thus preventing decoordination, or replacing the arene with a more suitable ligand.

Triazole-derived “click”-carbenes were demonstrated to offer straightforward routes to integrate triazolylidene transition metal complexes into self-supporting polymeric structures. The high stability of the triazolylidene iridium complexes allowed postmodification of the ligands, such as esterifications to generate Ir-NHC containing polyesters. The heterogeneized complexes catalyze CAN-driven water oxidation but recycling experiments suggest degradation of the polymer structure under the employed conditions. Electrocatalysis may however remedy the breakdown problem, rendering the system recyclable.

Crystallographic and ^{1}H NMR studies of a Ru-phenolatePYE complex revealed a dimeric species in the solid state, where ruthenium centeres are bridged by the phenolates. By addition

of suitable ancillary ligands to solutions of the dimer it was broken up into its monomeric counterparts and a preference for primary amines was established. Electrochemical analysis revealed two reversible oxidation events observed ($E_{1/2}$ (CH_3CN): -0.006 and 0.42 V; potentials vs Fc/Fc+). which were further characterized by UV-vis spectroscopy. EPR spectroscopy indicates that the first oxidation event is located on the ligand, which renders the ligand non-innocent. This makes this ligand an interesting target for coordination to early transition metals where it might impart nobility and enable catalytic pathways that require two electron transformations.

Erklärung

gemäss Art. 18 PromR Phil.-nat. 2019

Name/Vorname: Knörr Pascal

Matrikelnummer: 14-104-905

Studiengang: Chemie und Molekulare Wissenschaften

Bachelor ☐ Master ☐ Dissertation ☑

Titel der Arbeit: Synthesis of transition metal complexes for catalytic application in green energy storage

LeiterIn der Arbeit: Prof. Dr. Martin Albrecht

Ich erkläre hiermit, dass ich diese Arbeit selbständig verfasst und keine anderen als die angegebenen Quellen benutzt habe. Alle Stellen, die wörtlich oder sinngemäss aus Quellen entnommen wurden, habe ich als solche gekennzeichnet. Mir ist bekannt, dass andernfalls der Senat gemäss Artikel 36 Absatz 1 Buchstabe r des Gesetzes über die Universität vom 5. September 1996 und Artikel 69 des Universitätsstatuts vom 7. Juni 2011 zum Entzug des Doktortitels berechtigt ist. Für die Zwecke der Begutachtung und der Überprüfung der Einhaltung der Selbständigkeitserklärung bzw. der Reglemente betreffend Plagiate erteile ich der Universität Bern das Recht, die dazu erforderlichen Personendaten zu bearbeiten und Nutzungshandlungen vorzunehmen, insbesondere die Doktorarbeit zu vervielfältigen und dauerhaft in einer Datenbank zu speichern sowie diese zur Überprüfung von Arbeiten Dritter zu verwenden oder hierzu zur Verfügung zu stellen.

Bern, 23.05.2023

Ort/Datum

Unterschrift